DIRECT NUMERICAL SIMULATION OF INTERACTION OF DETONATION WAVE WITH HOMOGENEOUS ISOTROPIC TURBULENCE

by

HARI NARAYANAN NAGARAJAN

Presented to the Faculty of the Graduate School of

The University of Texas at Arlington in Partial Fulfillment

of the Requirements

for the Degree of

MASTER OF SCIENCE IN AEROSPACE ENGINEERING

THE UNIVERSITY OF TEXAS AT ARLINGTON

August 2009

To my mom, dad, brother, sister and friends.

ACKNOWLEDGEMENTS

ABSTRACT

DIRECT NUMERICAL SIMULATION OF INTERACTION OF
DETONATION WAVE WITH HOMOGENEOUS
ISOTROPIC TURBULENCE

HARI NARAYANAN NAGARAJAN, M.S.

The University of Texas at Arlington, 2009

Supervising Professors: Frank K. Lu and Luca Massa

The propagation of a shock or detonation wave through a reactive mixture has been the subject of research for over a century. The basic understanding has been shaped by one–dimensional Euler models, namely, those of Chapman–Jouguet and Zeldovich–Neumann–Döring, despite the fact that the detonation front is multi-dimensional. Other complications include observations of detonation instability, and spinning and galloping detonations. Recent advances in CFD have made it possible to examine detonation waves in great detail. These studies have revealed the complex nature of detonations that were observed experimentally. Some outstanding issues include the influence of inhomogeneities in the reactive mixture on the detonation process, such as the formation of hot spots. The understanding of such phenomena has practical implications, including in safe handling of fuels and in promoting detonations for detonation engines.

The current research is to comprehend the interaction of a detonation wave with a homogeneous isotropic turbulent field by solving three dimensional reactive

Navier–Stokes equation using direct numerical simulation. 5th order WENO scheme and 3rd order Runge Kutta technique are employed. The interaction of detonation wave with turbulence resulted in higher amplification of turbulence statistics (such as turbulent Mach number, turbulent length scales, rms of the velocity, etc). The study also revealed that there is an increase in turbulent kinetic energy in the range of wave number relevant to moderate and small scales. Investigation on the effect of heat release indicated that these changes are directly proportional to the heat release. The examination also involved the study relevant to the influence of the length scale which indicated that the changes in turbulence are proportional to the length scale.

TABLE OF CONTENTS

LIST OF FIGURES

LIST OF TABLES

CHAPTER 1

INTRODUCTION

The detonation-turbulence interaction problem is concerned with the unsteady coupling between convected vortical structures and a detonation wave. A better studied interaction is the shock-turbulence coupling problem. Lee et al. [1] recently analyzed the coupling and found that their nonlinear analysis agrees well with Ribner's linear interaction theory [2]. The detonation-turbulence interaction is different from the shock-turbulence interaction because of the role of the induction region in the amplification of convected vortical structures. Linear analysis [3] shows that the post-shock energy spectrum are maximally amplified by the resonant interaction in the induction region. Linear analysis provides useful insights, but fails to correctly represent the system dynamics near natural frequencies.

Powers [4] discussed the modeling aspects of the multiscale case epitomized by a detonation wave along with results generated using single step kinetics for chemical reaction while emphasizing the necessity of capturing finer scales. A similar technique with one-step kinetics is used for the present work. The pre-shock turbulent field is incompressible, isotropic and chemically homogeneous. The post-shock field is strongly inhomogeneous because of the thermo-fluid coupling in the induction region. Ribner et al. [5] states that the effect of exothermicity is to amplify the rms fluctuations downstream of the detonation, with the greatest changes occurring around the Chapman-Jouguet Mach number with a restrictive assumption of the reaction zone thickness being much smaller than the turbulence length scale (but induction zones

can be quite large). The influence of transverse waves on detonation and the pattern of quasi-steady detonation fronts are discussed by Dou et al [6].

The dynamics of small fluid-mechanics scales is vital to resolving the thermo-fluid interaction in the induction region of a detonation. An unstable detonation wave possesses a large set of intrinsic fluctuating frequencies with a range that increases with the activation energy [3]. A direct numerical simulation (DNS) of the fluid-mechanics equations in three dimensions usually delve in determining the fine-scale evolution. The problem in the present research is that it deals with extremities of scales. Turbulence encompasses phenomena taking place over an extremely wide range of scales from a few millimiters to hundred of thousand kilometers, from laboratory to galaxies. Usually, chemical reaction ensues in scales which are much finer than turbulence scales. Hence, we employ DNS in the present research to simulate the interaction.

The dynamics of small fluid-mechanics scales is vital to resolving the thermo-fluid interaction in the induction region of a detonation. An unstable detonation wave possesses a large set of intrinsic fluctuating frequencies with a range that increases with the activation energy [3].

It is well-known that the DNS of the shock–turbulence interaction is a complicated topic and in our case such an interaction with chemical reaction is studied and makes the research topic more sophisticated. The occurrence of a chemical reaction greatly complicates the analysis of processes. This is connected with the need to take into account a large number of intermediate and final reaction products, which have a considerable effect on the properties. But, for convenience, a simple one-step irreversible Arrhenius chemical reaction is selected for the present research to simulate detonations.

CHAPTER 2

PROBLEM DESCRIPTION AND BACKGROUND

2.1 Purpose of the Research

Decades of study on detonations has not resulted in satisfactory understanding because of the complex phenomena that takes place in it. One significant unexplored area is detonation instability. The demand to comprehend the instability phenomena entails research that deals with topics like the coupling between vortical structures and detonation waves, the role of induction zone and role of length scales.

2.2 Prior Research on Simulation of Compressible HIT

Turbulence has been examined experimentally, analytically and numerically for many decades [7, 8, 9, 10, 11, 12, 13, 14, 15, 16]. The relevance of theoretical methods on homogeneous isotropic turbulence flow investigation is discussed in [10, 17, 18, 19, 20, 21]. Experimental evidence on turbulence energy spectra revealed that all spectra collapse to a universal curve [11].

Direct numerical simulation (DNS) is a popular simulation technique for studies relevant to turbulent flows and this method is based on solving the Navier–Stokes equations numerically without resorting to any turbulence model. Its vital purpose is to capture the whole range of spatial and temporal scales of the turbulence. All the spatial scales of the turbulence must be resolved in the computational mesh, from the smallest dissipative scales (Kolmogorov microscales), up to the integral scale L, associated with the motions containing most of the kinetic energy. DNS can be carried

out using non-spectral, psuedo-spectral and spectral methods [22, 23, 24]. DNS based on spectral method is believed to provide the best accuracy for turbulence simulation.

Decay of freely-evolving, two-dimensional, isotropic turbulence was examined by Lowe [25] amongst others. This study showed the failure of Batchelor's theory with the proof that two-dimensional turbulence possesses second invariance since the peak in vorticity and the inertial energy range do not follow the k^{-3} decay.

DNS of the decay of isotropic turbulence using 64^3, 128^3 and 256^3 resolution shows good agreement with experimental results, see Mansour [26, 27]. The simulations also revealed that nonlinear terms play a vital role in energy evolution even at low Reynolds number. Statistics of the spatial evolution of turbulence such as turbulence intensity, vorticity, and velocity derivative skewness show that they are identical to results obtained from temporal evolution via Taylor's hypothesis except the dilatation term, see Lee [28]. Limitations of Taylor's hypothesis are discussed in [1]. Conditions for the occurrence of eddy shocklets in compressible turbulence decay were examined by Lee [29]. Three-dimensional turbulence is found to be less sensitive to the initial compressibility, and requires higher initial M_t for eddy shocklets to form than for two-dimensional turbulence. It was also found that higher M_t and higher Re increase the probability of occurrence of eddy shocklets.

The effect of compressibility on the dynamics and structures of turbulence decay are examined, e.g., in [30]. This study revealed that the joint probability density function has a universal structure. Even for compressible turbulence, the growth of enstrophy is associated to a preferntial alignment of the vorticity with the intermediate eigen vector of the anisotropic part of the strain-rate tensor as for incompressible turbulence. Pressure–dilatation correlation and its significance were analyzed by Sarkar [31]. Compressibility tends to reduce spatial intermittency in fully-developed turbulence, see Shivamoggi [32]. The energy decay in physical space is traced using the

Lagrangian correlation coefficient between local kinetic energy at different scales, see Meneveau et al. [33]. The Kolmogorov energy cascade is expected to be little affected by compressibility, and therefore remains independent of rms Mach number M_t [34]. The analysis of DNS data of compressible turbulence decay using the Helmholtz decomposition of the velocity field, Miura et al. [35] found that the pressure–dilatation term yields a dominant contribution to the exchange of compressive kinetic energy and internal energy.

Thermodynamic analysis of DNS data revealed that lower initial turbulent Mach number results in simple thermodynamic scalings whereas higher turbulent Mach number result in more complex thermodynamic scalings [36]. Analysis of the rate-of-strain tensor in compressible homogeneous turbulence helped to deduce the presence of these structures. Moreover, their shapes and orientations are quite different from those found in incompressible flows [37]. The results also confirmed that the vorticity and the dilatation are uncorrelated and statistically independent. The investigation by Goto [38] on the physical mechanism for the energy cascade showed that the cascade is due to the stretching of small-scale vortices by tubular vortex pairs. Vortex extraction studies were discussed by using wavelet decomposition [39], by using curvelet transform [40] and by using DNS [41]. These studies revealed that there are distinct differences in the vortex structures of compressible and incompressible turbulence. The $k^{-5/3}$ law is in itself not a sufficient indicator of inertial-range behavior [42] but requires that the inertial scales be small compared to the size of the solution domain. The finest scale intermittent fluctuations of fluid turbulence which are associated with a whole range of local dissipation scales have been studied by Schumacher et al. [43]. Increasing Reynolds number causes the generation of ever finer local dissipation scales. The results confirmed that the increasing small-scale intermittency affects a growing number of scales in the dissipation range.

DNS analysis by Samtaney [44] using 128^3 and 256^3 resolution, $M_t = 0.1$–0.5, $Re_\lambda = 50$–100 revealed that compressibility causes shocklets to occur. The shock thickness statistics are found to scale on the Kolmogorov length rather than the mean free path of the gas. Samtaney et al. also observed that the presence or absence of fluctuations of thermodynamic quantities as well as velocity divergence in the initial conditions are found to have negligible effect on the decay of turbulent kinetic energy. DNS results by Kops et al. [45] showed the ability of DNS to produce excellent agreement with the experimental results of isotropic turbulence decay experiments of Comte-Bellot and Corrsin.

Porter [13] performed simulations of decaying compressible turbulence with grid resolution of 512^3 and 1024^3 which revealed that the flow exhibits a self-similar character in large wavenumbers. DNS of incompressible turbulence based on the Fourier spectral method is carried out with 4096^3 grid resolution by Ishihara et al. [46, 47]. The DNS yields an energy spectrum exhibiting a wide inertial subrange, in contrast to previous DNS simulations at lower resolutions, and therefore provides valuable data for the study of the universal features of turbulence at large Reynolds number.

The suitability of ENO and WENO schemes with DNS and LES of compressible turbulence is discussed by Ladeinde [48]. The study revealed the requirement of filters by the ENO scheme to improve the energy transfer process at high wavenumbers and also the reason for limiting the useful wavenumber range. The WENO scheme does not require stabilizing filters but the results were found to be slightly more dissipative. On the other hand, Wu [49] found that the WENO and Runge–Kutta methods are too dissipative for DNS of shock wave and turbulent boundary-layer interactions and so limiters must be used.

Taylor et al. [50] showed the results of DNS of compressible turbulence while capturing shock-containing regions with the use of a bandwidth-optimized WENO

scheme. The simulation was carried with turbulence Mach number of 1.1 in the three-dimensional case and 2.0 in the two-dimensional case. Unacceptably high numerical dissipation even after optimization of the linear component that dominates in smooth regions is handled by using a "relative smoothness limiter" and a "relative total variation limiter" with WENO [51]. These limiters significantly enhance the grid convergence properties of WENO schemes for DNS of compressible turbulence. The numerical stability issue associated with compressible turbulence simulation is addressed by Honein et al [52]. The novel method's robustness is demonstrated up to a very high Reynolds number.

Supersonic turbulent flow is studied by many researchers [53, 54]. Preliminary results of numerical simulation of decaying supersonic turbulence using the piecewise parabolic method (PPM) on a mesh of 512^3 showed that the decay follows the classical Kolmogorov law [54, 55].

Methods other than DNS have also been employed to study turbulence simulation. These methods and their outcomes are discussed here. Owing to the limitation of insufficient computational capacity, DNS was restricted to low Reynolds number. Large eddy simulation has been proposed as the remedy to this limitation and has been in use recently. Large eddy simulation of two- and three-dimensional isotropic turbulence is discussed by many researchers [56, 57, 58, 59, 60]. Vreman et al. [58] discussed the results of decaying isotropic turbulence using a finite volume based, large eddy simulation with Smagorinsky's subgrid model. An analysis of the energy spectra showed agreement with the Kolmogorov law for the inertial range both for a low (0.05) and a moderate (0.6) rms Mach number. Results pertaining to DNS and LES of turbulent mixing layer are discussed in [15]. The suitability of subgrid scale models for turbulence simulation are discussed by Martin [60].

Recently, Thornber [61] carried out the simulation of homogeneous decaying turbulence using the implicit large eddy simulation technique and several schemes. It was observed from studying the kinetic energy spectra and the effective numerical filter that all the schemes employed are too dissipative. The growth of large scales and the dissipation of kinetic energy were well captured at resolutions greater than 32^3, or when using numerical methods of higher than 3rd order accuracy.

Compressible turbulence simulation using implicit large eddy simulation (ILES) is discussed by Rider [62]. A non-dissipative, robust, implicit algorithm is used to simulate the compressible turbulent flow and the results demonstrate that the algorithm is stable even in the convective time scale [63].

Detached-eddy simulation (DES) has also been used to study decaying homogeneous isotropic turbulence [64]. DES is based on the standard k-ϵ RANS model and yields a proper slope of the inertial range except that some energy accumulation can be found for the high wavenumbers.

The energy transfer process of compressible turbulence was analyzed using a two-point model [21]. The examination helped to demonstrate that the compressible energy is locally transferred from the solenoidal part to the compressible part for all the turbulent Mach numbers.

Rapid distortion theory (RDT) was used to analyze compressible homogeneous turbulence and its range of applicability was illustrated in [65, 66]. PDF modeling approach of inhomogeneous turbulence was developed by Slooten et al. [67]. This is an exact representation of RDT at the level of the directional spectrum. The extension of homogeneous turbulence models to inhomogeneous turbulence was accomplished by adding a stochastic variable representing the particle location and through the use of the full particle velocity. The results showed an apparent need for an improved dissipation model.

LANS-α equations were employed by Mohseni et al. [68] to study their ability to capture turbulence . The results showed that the LANS-α equations can capture most of the large-scale features of the turbulent flow while the effect of small scales on the large scales were modeled by Lagrangian averaging.

The lattice Boltzmann method (LBE) was employed to simulate decaying isotropic turbulence using DNS and LES [69]. The LBE results corroborate the published results and is potentially a reliable computational tool for turbulence simulations. Wavelets are a new mathematical tool used to analyze the turbulence, see [70] and it is expected to replace the present Fourier-space statistical methods. Turbulent motions are non-separable in the Fourier representation, while a wavelet representation may be able to provide such separability. The energy spectrum obtained using a wavelet based solution does not deviate from published results. It is also noted that the adaptive wavelet method will become particularly attractive for high Reynolds number flows due to the greater intermittency of the flow. The study of intermittency using wavelets to understand turbulence phenomena is shown in [71].

Studies other than natural decay of turbulence have also been performed and their results are discussed here. Studies with hyperviscosity [72] using forced homogeneous isotropic turbulence were attempted to examine the asymptotic behavior of TKE. As Re grows, the energy spectra extend to higher and higher wave numbers, with an attendant increase in the TKE. In all the cases, the higher wave number spectra were found to be self-similar under Kolmogorov scaling. The results showed that the model spectrum used in their research was inadequate to estimate the asymptotic slope.

The piecewise parabolic method (PPM) was applied to simulate forced isotropic turbulence by Schmidt et al. [73] and helped to study several properties such as bottleneck effect, and the range of length scales approximately satisfying Kolmogorov

scaling. The bottleneck phenomenon is nothing but the flattening of the spectrum function near the wave number of maximum dissipation. The magnitude of the bottleneck effect appears to be similar to what is obtained in simulations with hyperviscosity.

2.2.1 Chemical Reaction and Turbulence

Numerical studies pertaining to chemical reaction and turbulence has been performed for a decade or so [74, 75, 76, 77]. The effect of chemical reaction on decaying isotropic turbulence was studied by Martin et al. [74]. The study involving exothermic reaction revealed that positive temperature fluctuations increase the reaction rate, thereby increasing the heat released by the reaction, which further increases the temperature. It is also found that localized expansions due to reaction caused an increase in kinetic energy. Simultaneously, increased kinetic energy decay, vorticity production and Reynolds stress production were noticed. On the other hand, endothermic reactions resulted in damped temperature fluctuations.

Jaberi et al. [75] used a single-step, irreversible Arrhenius-type reaction to simulate the effects of chemistry on turbulence. The results showed a noticeable influence of chemical reaction on the solenoidal and dilatational turbulent motions. Doom et al. [76] used a spatially non-dissipative implicit numerical method with DNS and LES to perform the simulation of turbulent reacting flow.

2.3 Prior Research on Interaction of Shock Wave and Turbulence

All high-speed flows exhibit the ubiquitous phenomenon of shock-turbulence interactions. There has been extensive numerical and experimental study to comprehend the shock–turbulence interaction phenomena. One of the main application of such studies can be linked with hypersonic vehicles and propulsion systems. A shock

wave exhibits substantial unsteadiness and deformation as a result of the interaction, whereas the characteristic velocity, timescales, length scales of turbulence change considerably. The outcome of the interaction depends on the strength, orientation, location and shape of the shock wave as well as the flow geometry and boundary conditions. Several theoretical studies have also been carried out by Ribner [2, 5]. Linear interaction analysis of these interactions revealed that fluctuations amplify with length scale decrease across the shock wave. Significant acoustic noise was also found to be generated [5]. An excellent review on the physics behind shock wave and turbulence interaction is given by Andreopoulos et al. [78].

Anyiwo and Bushnell revisited the same research to understand the primary mechanisms of turbulence enhancement [79]. Numerical results also corroborated that the results of linear analysis are valid for range of parameters such as shock strength, incidence angle, amplitude of waves [80]. In the report by Jacquin et al. [81], it was shown that rapid distortion theory was inappropriate for the analysis of shock–turbulence interaction.

Weaker length-scale reduction, reduced amplification in the thermodynamic quantities by an order of magnitude and a different behavior of the pressure work term were observed for compressibe turbulent-shock case when compared against incompressible turbulence shock case [82]. It was also found that the incompressible flow case gives good agreement with LIA.

Jamme et al. [83] used DNS to study the interaction between normal shock waves of moderate strength and turbulence generated using Kovasznay's decomposition. Their research found the following observations. Computation of budgets of the fluctuating vorticity variances revealed that the baroclinic torque is responsible for additional production of transverse vorticity. Positive pressure dilatation is responsible for an energy transfer from the mean internal energy to the turbulent kinetic

energy immediately behind the shock. Investigation on fluctuation in the thermo-dynamic quantities depict enhancement by the shock wave and also is followed by a rapid decay immediately behind the shock. It was found that the classic estimation of Batchelor relating the dissipation rate and the integral scale of the flow proves to be invalid.

Interaction of moderately strong shock with a pre-existing turbulence showed an overall amplification of vorticity as has been noted for the case of a weak shock [84]. However, LIA indicates amplification of transverse vorticity and reduction of streamwise vorticity.

Fundamental aspects of shock–turbulence interaction and their modeling were reviewed by Lele [9]. Investigation of the effect of shock-normal Mach number on turbulence was carried out using both direct numerical simulation and linear analysis with stronger shock waves. The investigation revealed that the TKE is amplified across the shock wave and also the amplification saturates beyond $M_1 = 3.0$ [1, 85]. It was also observed that most turbulent length scale decrease across the shock wave while the dissipation length scale increase for $M_1 < 1.65$. Here, M_1 refers to shock Mach number. Fluctuations in thermodynamic variables are nearly isentropic for $M_1 < 1.2$ and deviate significantly from isentropy for the stronger shock waves. The energy spectrum was found to show higher energy levels at large wavenumbers, leading to an overall length scale decrease.

Results of LES of shock homogeneous interaction with four different subgrid scale models (Smagorinsky model, mixed scale model, dynamic Smagorinsky model, dynamic mixed model) and two different Mach numbers confirmed that the LES is efficient for such an interaction [86]. Although limited to low Reynolds numbers, LES also have been applied to the problem of shock–turbulence interaction and the results confirm LIA predictions [86, 87, 88]. The suitability of various schemes such as ENO,

WENO, MUSCL, Jameson for the shock–turbulence interaction was carried out with and without SGS models at different rms Mach numbers and resolutions [89].

Experimental studies also have been carried out to understand the physics of shock–turbulence interaction [90, 91, 92]. Experimental study by Xanthos et al. [90] of moving shockwave with nearly homogeneous isotropic decaying turbulence showed an amplification of pressure fluctuations which depends on the initial turbulence level and shock strength. Attenuation of shockwave strength has been found to take place as a result of the interaction. Keller et al. [91] showed the amplification of density fluctuations in their experiments.

2.4   Prior Research on Detonation

Supersonic flow phenomena comprising a shock front followed by a reaction zone is known as detonation. Various concepts of pulse detonation engines have been evaluated either theoretically or experimentally during the past several decades [93, 94, 95, 96, 97, 98].

Experimental studies relevant to detonation and pulse detonation engines have been carried out during past several decades [96, 99, 100]. Some of the experiments were concerned with the structure of detonation [97, 101, 95]. Experimental results with hydrogen–oxygen detonation also confirmed the existence of the induction zone [93] as postulated by ZND and observed by many others.

Numerical studies relevant to detonation also showed considerable progress [102, 103, 104, 105, 106, 107, 6, 108, 109, 110, 111, 112]. Most of the numerical simulation of detonation wave was carried out by using reactive Euler equations with single-step chemistry [6, 108, 109, 110, 111]. Recently, detonation waves were simulated with two-step chemistry [108, 113] and detailed kinetics [114, 115]. All these studies concentrated on the detonation wave structure. The one-dimensional detonation

wave simulation by LeVeque [110] discusses the existence of weak and the strong detonation and also basic features of detonation wave. Gamezo [105] investigated the two-dimensional unsteady detonation characterized by the cellular structure resulting from trajectories of triple-shock configurations formed by the transverse waves and the leading shock front. The numerical solution helped to examine the dynamics of the cellular detonation front involving the triple points, transverse waves and unreacted pockets. Tsuboi, Daimon and Hayashi [106] carried out three-dimensional numerical simulation of detonations in both a circular tube and a coaxial tube to investigate the characteristics of single spinning and two-headed detonations. The numerical results showed a feature of a single spinning detonation which was discovered in 1926. The results also revealed that there is no formation of an unreacted gas pocket behind the detonation front in the single spinning mode; however, the two-headed mode showed unreacted gas pocket behind the front near the axial insert. Issues pertaining to modeling detonation wave and the need to devise better ways to capture all the scales were discussed by Powers [4]. Multi-dimensional detonation wave solutions of the compressible reactive Navier–Stokes equation was used to resolve the diffusive scales and reactive scales [116].

The influence of transverse waves on detonation and the pattern of quasi-steady detonation fronts are discussed by Dou et al. [6]. The numerical simulation suggests that the two dimensional and three dimensional wave front formations are greatly enhanced by the presence of transverse waves. It is also stated that the influence of transverse wave is more profound in three dimension and the pattern of quasi-steady detonation fronts also depends on the duct size.

The effect of turning of the detonation wave around a corner and its consequence on post-diffraction evolution is also analyzed numerically, see [117]. Helzel [108] and Deledicque [109] produced the detonation wave simulation using exact Riemann

solution so as to limit the influence of the reaction term across discontinuities. Studies relevant to detonation initiation were also carried out numerically [113, 118].

The chemical reaction time scales are often orders of magnitude less than the fluid dynamical time scales. Well-known spurious numerical phenomenon occurs in standard finite volume schemes while dealing with stiff problem if the spatial/temporal resolution is not ample. A method to predict the detonation wave with accurate speed of propagation even in the stiff case is done by using a new fractional step method which proposes a two-value reconstruction [119]. Analytical and numerical study pertaining to detonation triggering helped to predict the main properties of flame acceleration like velocity profile, the flame shape, and the acceleration rate [111]. Their direct numerical simulation employed single step chemistry and the results matched those of the analytical ones.

2.5 Prior Research on Interaction of Detonation Wave and Turbulence

Very limited research has been done in the field of the interaction of detonation wave and turbulence. Due to the complexity involved in its physics, these studies were carried out by simplifying the process using linear interaction theory and analytical methods [3, 120, 121, 122].

The physics behind the interaction of a detonation wave with convected homogeneous isotropic weak turbulence is discussed in detail by Jackson et al. [120, 121]. It shows the effect of detonation Mach number on rms values of turbulence with an assumption of reaction zone being much smaller than the turbulence length scale. But, induction zones can be quite large. The increase in heat release parameter results in an increase in rms values of velocity and pressure, thereby increase in turbulence levels, with the greatest change occuring around the Chapman-Jouguet Mach number. It is observed that the noise levels increase due to detonation and turbulence

interaction. The increase in heat release also produces minimal increase in the longitudinal component of turbulence whereas significant increase in the temperature spectra and pressure spectra. The results showed that the exothermicity did not affect the Kolmogorov decay.

The numerical simulation of the interaction of an entropy spot with a shock wave [123] show that such interactions could be a potent source of turbulence production, especially in reacting flows. The study based on linear theory [122] revealed that exothermicity amplifies the resultant triad of vorticity, entropy and acoustic waves, significantly more so near the critical angle of incidence. The same was verified by the numerical results of Lasseigne et al. [124].

Short and Stewart [125] discussed the analytical result of the examination of the stability of an overdriven planar detonation wave for a one-step Arrhenius reaction model in the limit of weak effective heat release and an order-one activation energy; where these two parameters are scaled with respect to the post-shock detonation temperature. These limits allowed them to obtain an analytical dispersion relation which governs the stability of a detonation to small-amplitude perturbations. Massa and Lu [3] found that the post-shock energy spectra are maximally amplified by the resonant interaction in the induction region. Linear analysis provides useful insights, but fails to correctly represent the system dynamics near natural frequencies.

CHAPTER 3

GOVERNING EQUATIONS AND METHODOLOGY

3.1 Governing Equations

The motion of compressible fluid is described by the conservation of mass, momentum and energy. For a Newtonian fluid, the set of conservation equations is commonly called the Navier–Stokes equations which are expressed in Cartesian coordinates as

$$\frac{\partial \rho}{\partial t} + \frac{\partial}{\partial x_j}(\rho u_j) = 0 \tag{3.1}$$

$$\frac{\partial}{\partial t}(\rho u_i) + \frac{\partial}{\partial x_j}(\rho u_i u_j + p\delta_{ij} - \sigma_{ij}) - \rho f_i = 0, \quad i = 1, 2, 3 \tag{3.2}$$

$$\frac{\partial E}{\partial t} - \frac{\partial Q}{\partial t} - \rho f_i u_i + \frac{\partial}{\partial x_j}(E u_j + u_j p + q_j - u_i \sigma_{ij}) = 0 \tag{3.3}$$

where the independent variables t and x_j indicate time and three-dimensional Cartesian space, respectively, u_i are the velocity components, p is the pressure and ρ is the density. The viscous stress tensor for a Newtonian fluid is given by

$$\sigma_{ij} = \mu\left(\frac{\partial u_i}{\partial x_j} + \frac{\partial u_j}{\partial x_i} - \frac{2}{3}\delta_{ij}\frac{\partial u_k}{\partial x_k}\right), \quad i = 1, 2, 3 \tag{3.4}$$

The Kronecker delta is defined by

$$\delta_{ij} = \begin{cases} 0 & i \neq j \\ 1 & \text{otherwise} \end{cases}$$

The dynamic viscosity μ of an ideal gas is obtained as a function of the temperature T using Sutherland's formula

$$\mu = \mu_0 \frac{T_0 + C}{T + C} \left(\frac{T}{T_0}\right)^{3/2},$$

(3.5)

where T_0 is the reference temperature and C is the Sutherland constant. The specific total energy is given by

$$E = \rho \left(e + \frac{u_i^2}{2} + \text{potential energy} + \text{etc.}\right)$$

(3.6)

where e is the internal energy. The thermal conduction term is given by

$$q_j = -k \frac{dT}{dx_j}$$

(3.7)

The external heat addition or the finite-rate chemical reaction term is Q and $\rho f_i u_i$ represents the rate of work done by body forces. Closure of the Navier–Stokes equations require the thermal conductivity k to be defined. This is obtained via the Prandtl number Pr once the viscosity is known, as follows:

$$Pr \triangleq \frac{c_p \mu}{k}$$

(3.8)

$$k = \frac{c_p}{Pr} \mu$$

(3.9)

where c_p is the specific heat at constant pressure.

3.2 Development of the 3D WENO Euler Code

The three-dimensional Euler code is developed using Eqs. (3.1)–(3.3) by neglecting transport terms. The code also assumes zero body force and no external heat addition. The conservation form of the Euler equations can be written as

$$\frac{\partial \rho}{\partial t} + \frac{\partial}{\partial x_j}(\rho u_j) = 0 \tag{3.10a}$$

$$\frac{\partial}{\partial t}(\rho u_i) + \frac{\partial}{\partial x_j}(\rho u_i u_j + p\delta_{ij}) = 0, \quad i = 1, 2, 3 \tag{3.10b}$$

$$\frac{\partial E}{\partial t} + \frac{\partial}{\partial x_j}(E u_j + u_j p) = 0 \tag{3.10c}$$

Equations (3.10a)–(3.10c) are closed by the equation of state for a perfect gas

$$p = \rho R T \tag{3.11}$$

where R is the gas constant. The conservation form of the equations is used in the present numerical model because it results in a smooth solution for all problems [108]. The non-conservation form does not result in smooth solution [126].

3.2.1 Flux Term Evaluation

An important class of homogeneous hyperbolic equations is known as conservation equations [126]. The general form of such an equation in three-dimensional space is

$$q_t + f(q)_x + g(q)_y + h(q)_z = \psi(q) \tag{3.12}$$

where $q(x, y, z, t)$ is a vector of conserved variables. The flux functions in the x, y and z directions are $f(q)$, $g(q)$ and $h(q)$, respectively, while $\psi(q)$ represents the source term. More generally, a nonlinear hyperbolic system has the form

$$q_t + A(q, x, y, z, t)q_x + B(q, x, y, z, t)q_y + C(q, x, y, z, t)q_z = D(q, x, y, z, t) \quad (3.13)$$

where A, B, C and D are the coefficient matrices obtained using the eigenvalues. The easiest way to solve a multi-dimensional problem is by using the dimensional splitting approach. A multi-dimensional problem is simply split into a sequence of one-dimensional problems and hence use dimension-by-dimension reconstruction. The reconstruction is carried out using the WENO 5th order scheme [127, 128, 129, 130, 131, 132, 133, 134, 135]. Weighted essentially non-oscillatory (WENO) methods have been developed to simultaneously provide robust shock capturing in compressible turbulence fluid flow and avoid excessive damping of fine-scale flow features such as turbulence [51]. For example, Eq. (3.13) can be split into

$$\text{xsweeps}: q_t + A(q, x, y, z, t)q_x = 0 \quad (3.14a)$$

$$\text{ysweeps}: q_t + B(q, x, y, z, t)q_y = 0 \quad (3.14b)$$

$$\text{zsweeps}: q_t + C(q, x, y, z, t)q_z = 0 \quad (3.14c)$$

A genuine multi-dimensional reconstruction considers all cells in the multi-dimensional stencil simultaneously to build up a reconstruction polynomial, whereas dimension-by-dimension reconstruction consist of a number of one-dimensional reconstruction sweeps. Dimension-by-dimension reconstruction at each face uses data in a slice orthogonal to that face. Dimension-by-dimension reconstruction is simpler and computationally less expensive than the genuine multi-dimensional approach [136].

Many numerical methods have been developed to solve the Eq. (3.13). Here, an approximate Riemann solver is employed as the numerical method. The Riemann problem [137], is simply the hyperbolic equation together with the piecewise constant initial data

$$q(x,0) = q_0(x) = \begin{cases} q_l & x < 0 \\ q_r & x > 0 \end{cases} \tag{3.15}$$

If Q_{i-1} and Q_i are the cell averages in two neighbouring grid cells on a finite volume grid, then by solving the Riemann problem with $q_l = Q_{i-1}$ and $q_r = Q_i$, we can obtain information that can be used to compute a numerical flux and update the cell averages over a time step. For hyperbolic systems, the Riemann problem is easily solved in terms of the eigenvalues and eigenvectors of the matrix A. Computationally, the exact Riemann solution is often too expensive to compute for nonlinear problems so an approximate Riemann solver is used in implementing numerical methods.

In the x sweep, the conservation law is integrated over a cell to obtain

$$\frac{\partial Q_i}{\partial t} = -\frac{1}{\Delta x} \left(A^- \Delta q_{i+1/2} + A^+ \Delta q_{i-1/2} + A \Delta q_i \right) \tag{3.16}$$

where

$$A^- \Delta q_{i+1/2} = \sum_{p=1}^{m} (s_{i-1/2}^p)^+ W_{i-1/2}^p \tag{3.17a}$$

$$A^+ \Delta q_{i-1/2} = \sum_{p=1}^{m} (s_{i+1/2}^p)^- W_{i+1/2}^p \tag{3.17b}$$

$$A \Delta q_i = f(q_{i+1/2}^-) - f(q_{i-1/2}^+) \tag{3.17c}$$

The $A^-\Delta q$ term represents the net effect of all left-running waves while $A^+\Delta q$ represents the net effect of all right-running waves; W^p represents the jump across the pth wave,

$$\Delta q = q_r - q_l = \sum_{p=1}^{m} W^p \tag{3.18}$$

where m is the number of waves and each wave has an associated wave speed s^p.

3.2.2 Time Stepping

Equation (3.16) is integrated using an ODE solver. The third-order, three-step Runge–Kutta (RK) method is used here. By using two trial steps per interval, it is possible to cancel out both the first- and second-order error terms and, thereby, construct a third-order Runge–Kutta method. Analogously, using three trial steps per interval yields a fourth-order RK method, etc. [138]. In the present solver, the third-order RK method [139] is used for time stepping and is given by

$$Q^{(1)} = Q^{(n)} + \Delta t L(Q^{(n)}) \tag{3.19a}$$

$$Q^{(2)} = \frac{3}{4}Q^n + \frac{1}{4}Q^{(1)} + \frac{1}{4}\Delta t L(Q^{(1)}) \tag{3.19b}$$

$$Q^{(n+1)} = \frac{1}{3}Q^n + \frac{2}{3}Q^{(2)} + \frac{2}{3}\Delta t L(Q^{(2)}) \tag{3.19c}$$

Third-order accuracy is shown by evaluating $Q^{(n+1)}$ in terms of $Q^{(n)}$, where n corresponds to the value of Q at the old time, $n+1$ corresponds to the value of Q at the new time and $L = \partial Q/\partial t$. This approach is called the Total Variation Dimnishing (TVD) Runge–Kutta scheme [139] because the fractions are positive.

3.3 Development of 3D WENO Navier–Stokes Code

The Navier–Stokes equations with the absence of external heat addition and body forces are obtained from Eqs. (3.1)–(3.3) as

$$\frac{\partial \rho}{\partial t} + \frac{\partial}{\partial x_j}(\rho u_j) = 0 \tag{3.20a}$$

$$\frac{\partial}{\partial t}(\rho u_i) + \frac{\partial}{\partial x_j}(\rho u_i u_j + p\delta_{ij} - \sigma_{ij}) = 0, \quad i = 1, 2, 3 \tag{3.20b}$$

$$\frac{\partial E}{\partial t} + \frac{\partial}{\partial x_j}(E u_j + u_j p + q_j - u_i \sigma_{ij}) = 0 \tag{3.20c}$$

The flux terms are evaluated using the scheme described in the Section 3.2.1 while the viscous terms are evaluated using the central difference scheme. The time integration is carried out using the 3rd order Runge-Kutta method explained in Section 3.2.2.

3.3.1 Non–Dimensional Form

Equations (3.20a)–(3.20c) are non-dimensionalized so that characteristic parameters, viz., the Mach, Reynolds and Prandtl numbers can be varied independently. The nondimensionalization procedure is obtained using the equations given below,

$$
\begin{aligned}
x_i^* &= \frac{x_i}{L} \quad t^* = \frac{t}{L/V_\infty} \quad \mu^* = \frac{\mu}{\mu_\infty} \\
\rho^* &= \frac{\rho}{\rho_\infty} \quad T^* = \frac{T}{T_\infty} \quad e^* = \frac{e}{V_\infty^2} \\
u_i^* &= \frac{u_i}{V_\infty} \quad p^* = \frac{p}{\rho_\infty V_\infty^2}
\end{aligned}
\tag{3.21}
$$

The nondimensionalized variables are denoted by asterisks, the freestream conditions are denoted by ∞ and the Reynolds number is given by

$$Re_L = \frac{\rho_\infty V_\infty L}{\nu_\infty} \tag{3.22}$$

The nondimensional form of the shear stress tensor and the heat flux vector are given by

$$\sigma^*_{ij} = \frac{\mu^*}{Re_L}\left(\frac{\partial u^*_i}{\partial x^*_j} + \frac{\partial u^*_j}{\partial x^*_i} - \frac{2}{3}\frac{\partial u^*_k}{\partial x^*_k}\delta_{ij}\right) \tag{3.23}$$

$$q^*_i = -\frac{\mu^*}{(\gamma - 1)M^2_\infty Re_L Pr}\frac{\partial T^*}{\partial x^*_i} \tag{3.24}$$

where the freestream Mach number M_∞ is given by

$$M_\infty = \frac{V_\infty}{\sqrt{\gamma R T_\infty}} \tag{3.25}$$

The perfect gas equations of state become

$$p^* = (\gamma - 1)\rho^* e^* \tag{3.26}$$

$$T^* = \frac{\gamma M^2_\infty p^*}{\rho^*} \tag{3.27}$$

Because of the self-similarity of the Navier–Stokes equations, the dimensionless form and the original form, Eqs. (3.1)–(3.3), are identical.

3.3.2 Implementation of Single–Step Chemistry with 3D WENO Navier–Stokes Code

Using one step, irreversible, Arrhenius kinetics, the chemical interaction between two perfect gases $A \rightarrow B$ is modeled. The governing equations in conservation form become

$$\frac{\partial \rho}{\partial t} + \frac{\partial}{\partial x_j}(\rho u_j) = 0 \tag{3.28a}$$

$$\frac{\partial}{\partial t}(\rho u_i) + \frac{\partial}{\partial x_j}(\rho u_i u_j + p\delta_{ij} - \sigma_{ij}) = 0, \quad i = 1, 2, 3 \tag{3.28b}$$

$$\frac{\partial E}{\partial t} + \frac{\partial}{\partial x_j}(Eu_j + u_j p + q_j - u_i \sigma_{ij}) = 0 \tag{3.28c}$$

$$\frac{\partial \rho\tilde{\lambda}}{\partial t} + \frac{\partial}{\partial x_j}(\rho\tilde{\lambda} u_j) = (\rho - \rho\tilde{\lambda})r(T) \tag{3.28d}$$

The variable $\tilde{\lambda}$ is the reaction progress, where $\tilde{\lambda} = 0$ describes the unburnt state and $\tilde{\lambda} = 1$ the completely burnt state. The other variables are the same as in nonreactive case. Here, the total energy of the fluid is given by

$$E = \rho\left(\frac{P}{\gamma - 1} + \frac{u_i^2}{2} - Q_0\tilde{\lambda}\right) \tag{3.29}$$

where Q_0 is the heat release and the term $Q_0\rho\tilde{\lambda}$ denotes the chemical energy which is released as heat during the burning process. The reaction rate $r(T)$ is described by single step, Arrhenius law and depends on temperature T through the relation

$$r(T) = K_0 \exp^{-\left(\frac{E_a}{T}\right)} \tag{3.30}$$

where K_0 is the pre-exponential factor and it is also known as rate constant that sets the temporal scale of the reaction, E_a is the activation energy. The assumption of

a single-step, Arrhenius kinetics law for $r(T)$ has been often employed in numerical studies. The important characteristics of the propagation of detonation waves can be sufficiently described by this simple chemistry model. On the other hand, this simplified model cannot provide an accurate description of the thermochemistry of real-life detonations and, therefore, its applicability has certain limitations. Important phenomena, such as detonation initiation or deflagration-to-detonation transitions, require a more detailed reaction mechanism [109].

The nondimensional form for the nonreactive terms are obtained using the Eqs. (3.21)–(3.27), and for the reactive terms are obtained using the following relation

$$Q^* = \frac{QP}{\rho} \tag{3.31a}$$

$$E_a^* = \frac{E_a P}{\rho} \tag{3.31b}$$

$$K_0^* = K_0 \sqrt{\left(\frac{P}{\rho}\right)} \tag{3.31c}$$

CHAPTER 4

VERIFICATIONS AND VALIDATIONS

4.1 Verification of One-Dimensional Euler Code

A compressible code's ability to capture shocks and discontinuities is usually verified via standard test cases such as the Sod shock tube problem and the Lax problem.

4.1.1 Sod and Lax Problems

The one-dimensional version of the WENO Euler code [140] is initially validated using the Sod and Lax problems. In both cases, the computational domain is $(-5, 5)$ and the number of cells N was taken as 500. Zero-order boundary conditions are employed. These two cases contain only shocks and simple smooth regions for which shock resolution is the main concern. Usually, a good second-order non-oscillatory scheme would give satisfactory results. The 5th-order scheme provides some advantage in the results than what was observed with the 2nd-order scheme [135]. The results are discussed below.

4.1.2 The Sod Problem

The initial data used for the Sod problem are

$$(\rho, u, P) = \begin{cases} 1, 0, 1 & x < -4 \\ 0.125, 0, 0.1 & x \geq -4 \end{cases}$$
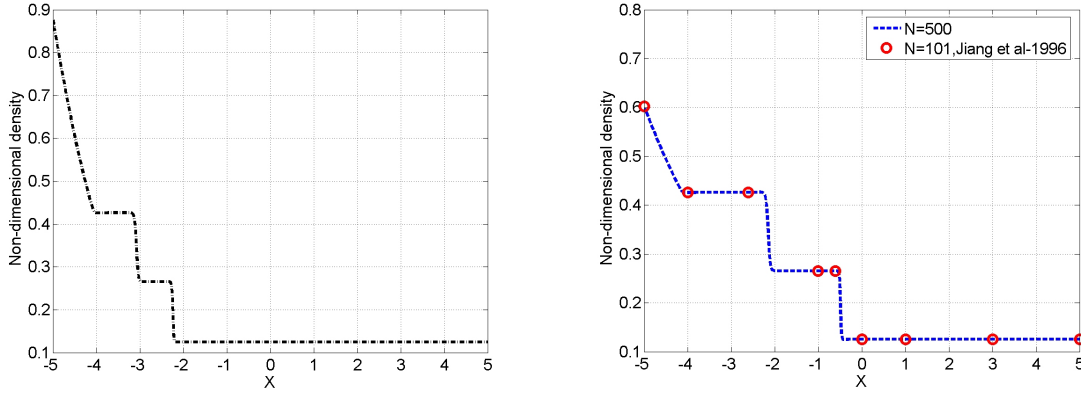
Figure 4.1. Sod shock tube problem, density trend t=1 (left) and t=2 (right).

The density trend shows a good agreement with the analytical results and is shown in right of Fig. 4.1. These trends compare well with results for a 5th-order WENO scheme with 101 equally distributed points [139]. The shock is captured as a sharp front without oscillations.

4.1.3   The Lax Problem

The initial data used for the Lax problem are

$$(\rho, u, P) = \begin{cases} 0.445, 0.698, 3.528 & x < -4 \\ 0.5, 0, 0.571 & x \geq -4 \end{cases}$$

The density trend shows that the shock is captured as a sharp front without oscillations and confirms reasonable agreement with analytical result, see right of Fig. 4.2. These trends compare well with results for a 5th-order WENO scheme with 101 equally distributed points [127].
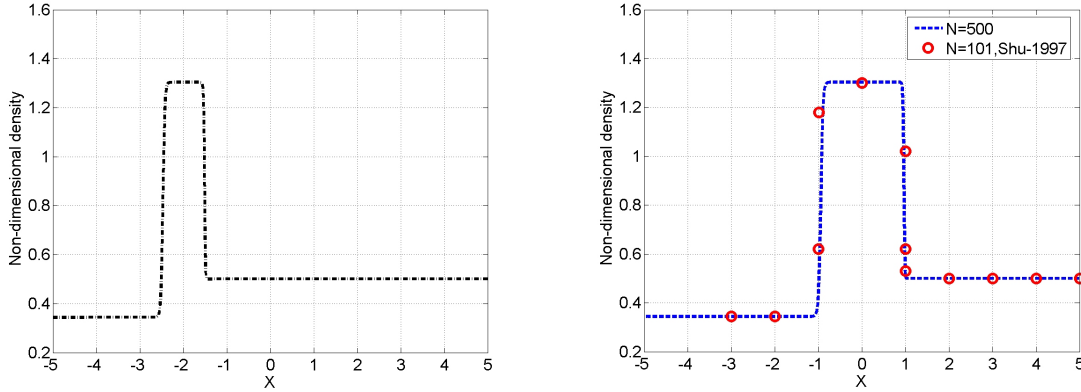
Figure 4.2. The Lax problem, density trend t=1 (left) and t=2 (right).

4.2   Verification of One-Dimensional Euler Code with Chemical Reaction

The validation of the chemical reaction routine was carried out using the one-dimensional version of the Euler code. This involved the simulation of the propagation of a one-dimensional detonation wave.

4.2.1   One-Dimensional Detonation Wave Propagation

Simulation of one-dimensional detonation wave is accomplished using the concepts based on the well-known ZND model [141]. A detailed description of the ZND model can be found in [142, 112]. The basic principles behind the detonation process are as follows. The shock heats the material (fuel and oxidizer), triggering the chemical reaction and causing the detonation (supersonic combustion). The region that follows the shock is called the reaction zone. The reaction takes place in the reaction zone and becomes complete in the final state. The shock and the reaction zone propagate with a velocity known as the detonation velocity D. A typical schematic of detonation is shown in Figure 4.3. In the figure, P is pressure.

In this validation, an inviscid, non-heat conducting gas is assumed. A simple model of chemical interaction between two perfect gases $A \rightarrow B$, is obtained using
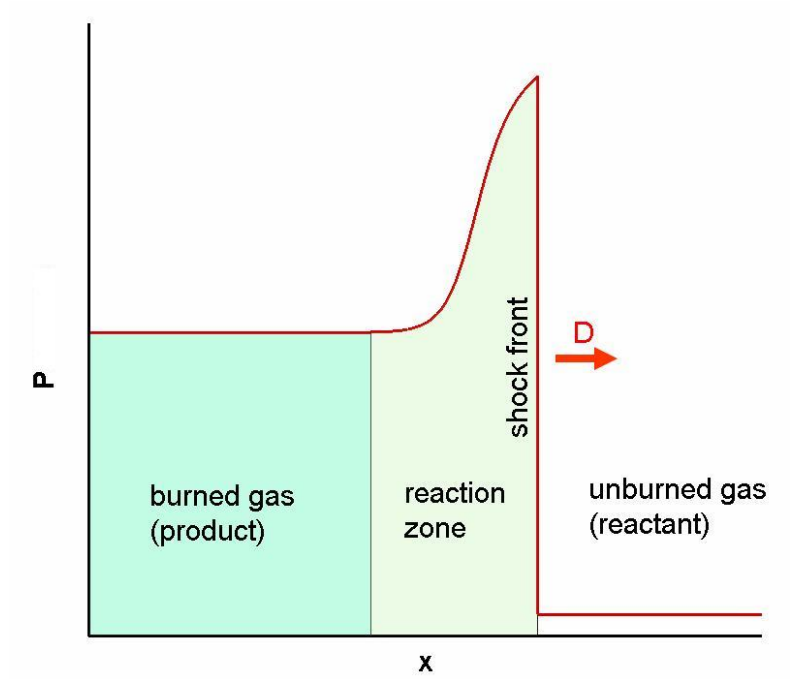
Figure 4.3. Detonation schematic.

one-step, irreversible Arrhenius kinetics. The pre- and post-detonation conditions are obtained using the Rankine–Hugoniot conditions,

$$\rho u = -D\rho_0 \tag{4.1a}$$

$$\rho u^2 + P = D^2 \rho_0 + P_0 \tag{4.1b}$$

$$\rho u \left(\frac{P}{\rho(\gamma - 1)} + Q_0 Z + \frac{u^2}{2} \right) + pu = -D\rho_0 \left(\frac{P_0}{\rho_0(\gamma - 1)} + Q_0 + \frac{D^2}{2} + \frac{P_0}{\rho_0} \right) \tag{4.1c}$$

$$Z = Z_0 \tag{4.1d}$$

where the subscript 0 refers to the pre-detonation condition and Z is the massfraction. Employing the relationship $\tilde{\lambda} = 1 - Z$, Eqs. (4.1c)–(4.1d) can be simplified to yield

$$\frac{\gamma}{\gamma - 1}\frac{P}{\rho} - Q_0\frac{P}{\rho}\tilde{\lambda} + \frac{u^2}{2} = \frac{\gamma}{\gamma - 1}\frac{P_0}{\rho_0} + \frac{u_0^2}{2} \tag{4.2a}$$

$$\tilde{\lambda} = \tilde{\lambda}_0 \tag{4.2b}$$

These equations are closed by using the definition of the overdrive factor of a ZND detonation

$$f = \left(\frac{D}{D_{CJ}}\right)^2 \tag{4.3}$$

where D is the detonation velocity and $D_{CJ} = M_{CJ}\sqrt{\gamma P_0/\rho_0}$ is the velocity of the corresponding Chapman–Jouguet wave (defined as the detonation in which the gas velocity at the end of the reaction zone and in the reference frame of the shock, equals to the speed of sound). The Chapman–Jouguet Mach number

$$M_{CJ}^2 = 1 + \frac{\gamma^2 - 1}{\gamma}q_0 + \sqrt{\frac{\gamma^2 - 1}{\gamma}q_0\left(2 + \frac{\gamma^2 - 1}{\gamma}q_0\right)} \tag{4.4}$$

The reference length is chosen as the half reaction length of the ZND profile $L_{1/2}$, i.e., the distance between the shock wave and the point where $Z = 0.5$, is used as the characteristic length.

4.2.2 Results and Discussion

Results of numerical simulations for two different cases of one-dimensional detonations are presented. A ZND profile is used as initial conditions. The parameters used for the one-dimensional detonation are the overdrive factor $f = 1.0$, the heat release $q_0 = 50$, the activation energy $E_a = 20$, and the specific heat ratio $\gamma = 1.2$. The initial pressure is 1.0. This combination resulted in a detonation Mach number of
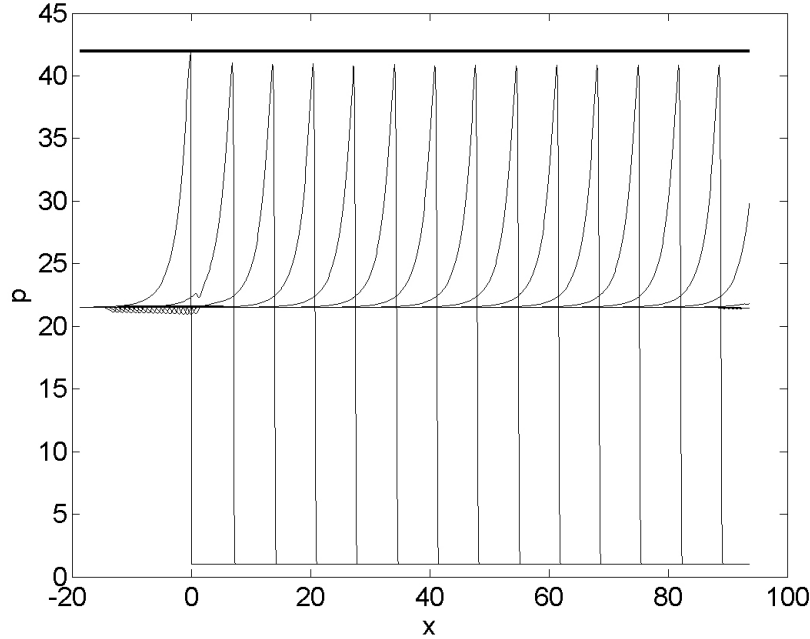
Figure 4.4. One-dimensional detonation wave simulated by using the 5th-order WENO scheme with $dx = L_{1/2}/8$.

6.216. The computational domain is $(-5, 5)$ and uses $N_x = 500$. Two different mesh resolutions ($dx = L_{1/2}/8$ and $dx = L_{1/2}/16$) were employed and they resulted in 8 and 16 points per half-reaction length respectively. The boundary condition imposed is the zero-order flux condition. The pressure profiles of a one-dimensional detonation wave propagation for 8 and 16 points per half reaction length are shown in Figs. 4.4 and 4.5 respectively. The computed ZND pressure with $\tilde{\lambda} = 0$ is indicated by the horizontal thick solid line and its value correspond to 42.06. With $\tilde{\lambda} = 1$, the pressure obtained is 21.53.

The time-step between each of the detonation-waves observed in the graph is 1.0. On comparison of Fig. 4.4 and Fig. 4.5, it reveals that the peak pressure is closer to the ZND pressure with $N_x = 500$ and $dx = L_{1/2}/16$ combination. Further increase in grid cells did not result in any improvement in the peak pressure than that was
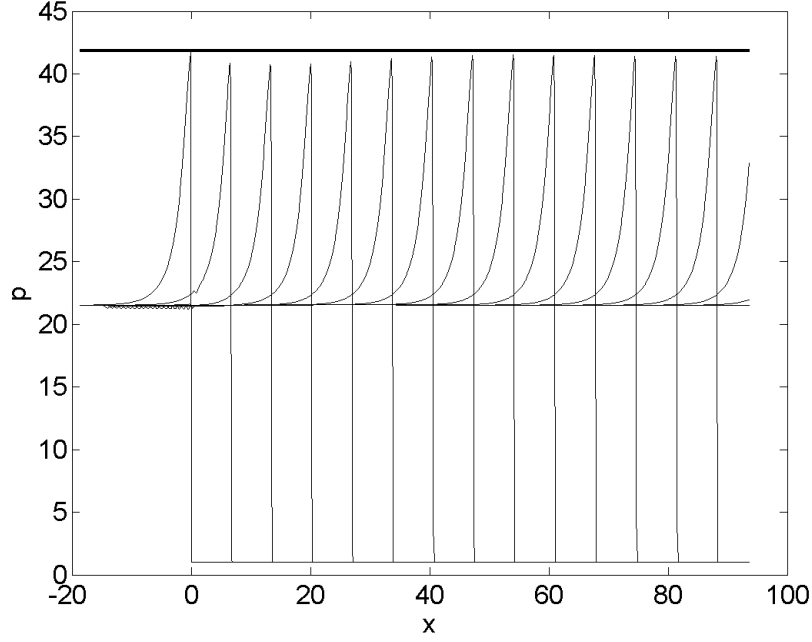
Figure 4.5. One-dimensional detonation wave simulated by using the 5th-order WENO scheme with $dx = L_{1/2}/16$.

observed in the case with $dx = L_{1/2}/16$. Hence, the results with higher half reaction length and grid cells indicate a satisfactory convergence of the solver. The results also corroborate with that of Dou et al. [6]. Hence, the chemical reactive solver was verified by simulating the propagation of a detonation wave in one dimension.

4.3 Validation of Three-Dimensional Euler Code

The one-dimensional version of the WENO Euler code [140] was modified into a three-dimensional WENO Euler code. The WENO reconstruction is carried out using dimension by dimension approach.

4.3.1   Interaction of a Shock Wave with Density Waves

The shock–density wave interaction problem is used to validate the three dimensional WENO Euler code. This problem is more complex than those used in the validation of the one-dimensional Euler code. It will be shown that a higher-order scheme will show its advantage when the problem contains both shocks and complex smooth regions.

4.3.2   Initial Condition and Results

The three-dimensional WENO Euler code is used to capture the physics of a shock wave at Mach 3 interacting with a sinusoidal density distribution. The computational domain is $(-5, 5)$ and the simulation was carried out with two different grid resolutions, namely, $\{N_1, N_2, N_3\} = \{50, 5, 5\}$ and $\{200, 5, 5\}$ where $\{N_1, N_2, N_3\}$ are the number of grid points in the (x, y, z) directions respectively. Zero-order boundary conditions are employed in all the three directions and dimension-by-dimension reconstruction is adopted. The initial condition used are

$$(\rho, u, P) = \begin{cases} 3.85714, 2.6294, 10.3333 & x < -4 \\ 1 + \epsilon \sin 5x, 0, 1 & x \geq -4 \end{cases}$$

Here, we take $\epsilon = 0.2$. The computed density is plotted for several time instances, namely $t = 0$, 1.0, 1.8 and 2.0.   The results pertaining to the resolution of $200 \times 5 \times 5$ is shown in Fig. 4.6. The graphs show the shock–density interaction visualizing the three-dimensional data in two dimension along a slice in z except the bottom right graph which is the one-dimensional visualisation of the three-dimensional data. These trends agree with the published results for a 5th-order WENO scheme[135]. Due to the drastic change in both velocity and density across the shock, it is observed that
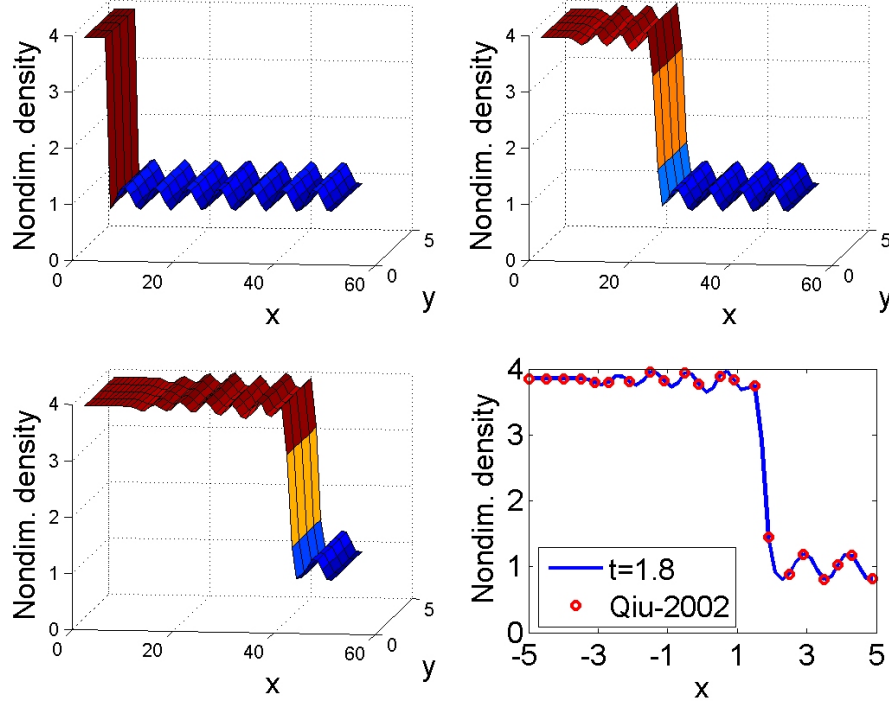
Figure 4.6. The shock-density wave interaction problem, $t = 0$, $t = 1.0$, $t = 1.8$ and $t = 2.0$ (in the clockwise direction).

the interaction ensued in suppression of sinusoidal oscillation post shock propagation. It is clear that the 5th-order WENO scheme resolves the salient features of the flow accurately.

4.4   Validation of Three-Dimensional Navier–Stokes Code

The three-dimensional Euler code was converted to a Navier–Stokes code by considering the transport terms. The code was validated using two different topics, viz., simulation of compressible homogeneous isotropic turbulence decay and simulation of interaction of shock wave and turbulence.

4.4.1 Compressible Homogeneous Isotropic Turbulence Decay

The simulation of weakly compressible homogeneous isotropic decaying turbulence is carried out to validate the solver. The initial energy spectrum is the Mansour–Wray spectrum [26]

$$E(k,0) = \frac{q^2}{2A} \frac{1}{k_p^{\sigma+1} k^\sigma} \exp\left[-\frac{\sigma}{2} \left(\frac{k}{k_p} \right)^2 \right] \tag{4.5}$$

where k_p is the wave number at which $E(k, 0)$ is maximum, σ is a parameter, and

$$A = \int k^\sigma \exp\left(-\frac{\sigma k^2}{2} \right) dk \tag{4.6}$$

The energy spectrum is related to the amplitude of the Fourier modes of the velocity components and also yields a random and isotropic field. This particular energy spectrum is chosen because it has proved capable of representing low and moderate Reynolds number turbulence with a good match to experimental data [26]. On the other hand, high Reynolds number turbulence can be represented accurately using Karman spectrum [9]. The velocity components are generated by three sets of random numbers that permit the uniform distribution of the angles $(\theta_1, \theta_2, \phi)$ on the interval $(0, 2\pi)$. The velocity components are

$$\tilde{u}_1 = \frac{\alpha |k| k_2 + \beta k_1 k_3}{|k| k_h} \tag{4.7a}$$

$$\tilde{u}_2 = \frac{-\alpha |k| k_2 + \beta k_3 k_2}{|k| k_h} \tag{4.7b}$$

$$\tilde{u}_3 = \frac{\beta k_h^2}{|k| k_h}. \tag{4.7c}$$

The tilde symbol indicates that these are complex quantities. The above expressions fulfill the requirement of a solenoidal velocity field in wave-number space $k_i u_i = 0$. Moreover, it can be shown that if

$$
\begin{aligned}
\alpha &= \frac{E(k,0)}{4\pi k^2} \exp(l\theta_1) \cos(\phi) \tag{4.8a} \\
\beta &= \frac{E(k,0)}{4\pi k^2} \exp(l\theta_2) \cos(\phi) \tag{4.8b}
\end{aligned}
$$

the three-dimensional energy spectrum of this field is equal to $E(k, 0)$. These initial conditions are used in [7].

4.4.2   Parallel Version of the Navier–Stokes Code

DNS is the most satisfactory approach for turbulence simulation. This method solves the equations governing turbulence without using any explicit or implicit modeling of any scale of motion. Unfortunately, for a simulation to resolve the finest scales of motion, both in time and space, the grid spacing and time step must be considerably small. The very small time step entails enormous computational power. Besides, DNS of reactive compressible turbulence aggravate the computational load further due to the need to resolve length and time scales of the reaction. All of these reasons point to the necessity of parallelizing the code. Parallelism is used to distribute the grid nodes to more than one processor, hence dividing the physical domain into areas, each of which is simulated on a different machine. Obviously, each computing node exchanges information at the boudaries.

Advanced computing infrastructure of the Texas Advanced Computing Center (TACC) Lonestar cluster located at the University of Texas at Austin is used to accomplish the studies relevant to the present research. The TACC Lonestar cluster is one of the largest academic computational resources in the nation [143]. The

Lonestar Linux cluster consists of 1300 nodes, with 2 dual-core processors per node, for a total of 5,200 cores. It is configured with 10.4 TB of total memory and 95 TB of local disk space. Nodes are interconnected with InfiniBand technology in a fat-tree topology with a 1GB/sec point-to-point bandwidth. A 10 PB capacity archival system is available for long-term storage and backup. TACC's visualization support is also used in postprocessing the three-dimensional data.

The three-dimensional compressible Navier–Stokes code with WENO solver is parallelized using MPI for message passing parallelism. The code uses a three-dimensional domain decomposition and MPI communication. Each MPI process is in charge of a piece of the three-dimensional domain. All MPI processes have the same number of grid points and the same computational load. Inter-processor communication is only between the nearest neighbors in a three-dimensional topology.

4.4.3 Results

Simulation of the temporal decay of weakly compressible homogeneous isotropic turbulence is carried out using four different grid resolutions (32^3, 64^3, 128^3, 256^3). The results are compared with three-dimensional incompressible turbulence simulation (see Appendix B) carried out earlier. The procedure adopted and the formulae used to analyze these data are explained in Appendix C. The computational domain is ($2\pi \times 2\pi \times 2\pi$) and the simulation was carried out using uniform grid spacing in the three directions. Periodic boundary conditions are employed in the three directions and dimension-by-dimension reconstruction is adopted. The density, turbulent Mach number, pressure, Reynolds number based on the Taylor length scale govern the generation of the initial turbulent field. Initialization of isotropic turbulence begins with uniform density and pressure and completely random velocity values. The initial energy spectrum is obtained using the Mansour–Wray energy model. The convective

numerical fluxes are computed using a 5th-order scheme. The viscous fluxes, which are diffusive in nature, are computed using a 4th-order central standard scheme.

There are three length scales which represent the turbulent flow, namely, the integral length scale, the Kolmogorov microscale and the Taylor microscale. The Taylor microscale represents the transition from the inertial subrange to the dissipation range and is the length scale where viscous dissipation starts to become important. The Reynolds number based on the Taylor length scale is obtained using

$$R_\lambda = \sqrt{\frac{20}{3}} \frac{\int_0^\infty E(k,t)dk}{\nu(\int_0^\infty k^2 E(k,t)dk)^{\frac{1}{2}}} \tag{4.9}$$

Note that R_λ is a fundamental quantity in isotropic turbulence which characterizes the energy spectrum. The initial Reynolds numbers based on the Taylor microscale are 162, 135, and 118 for the 64^3, 128^3, 256^3 grid cases respectively. The Taylor microscale can be computed using

$$\lambda = \sqrt{\frac{u_i' u_i'}{u_{1,1}' u_{1,1}'}} \tag{4.10}$$

The turbulent Mach number is given by

$$M_t = \frac{q}{a} \tag{4.11}$$

where $q = \sqrt{u_i' u_i'}$, u_i' is the fluctuation from the ensemble-averaged velocity and a is the mean speed of sound, where $a = \sqrt{\gamma \frac{P}{\rho}}$. Pressure, density are volume averaged at any given time instant. It must be remembered that the compressibility effects are small in the present turbulence study.

The validation of the 5th-order WENO scheme for turbulence simulation is accomplished by comparing the DNS results of incompressible turbulence simulation based on the Arakawa solver and the DNS results of weakly compressible turbulence obtained using the WENO scheme. It must be noted that the incompressible turbulence simulation based on Arakawa solver is validated against the experimental data of Comte-Bellot and Corrsin at $Re_\lambda = 60.7$ [144] and that of Mansour & Wray at $Re_\lambda = 56.2$ [26]. In both cases, all the parameters were maintained identical and were using 64^3 grid resolution. In the compressible homogeneous turbulence simulation, the initial turbulent Mach number is maintained as 0.282, isentropic index as 1.4, Lewis number as 1.0 and Prandtl number as 0.72. The Reynolds number is maintained to be 1000 in both the compressible HIT and incompressible HIT simulation. The initial energy spectrum with 64^3 grid resolution is shown in Fig. 4.7 where $(E(1), E(2), E(3))$ are the energy spectra in (x, y, z) respectively. The initial spectrum is close to each other because the compressibility is weak in case of the compressible turbulence. The rms values of the velocities in the three directions match closely with those obtained using the incompressible turbulence code. The results are shown in Fig. 4.8, where vrms(1), vrms(2), vrms(3) refer to the rms of velocities in the x, y, z direction respectively and prms is the rms of the pressure. Here, time is a nondimensional parameter and it is identical for both compressible and incompressible turbulence simulation. This time is the fraction of the distance across the initial energy containing scale which has been traversed by sound waves moving at the average sound speed in the initial state. The result of comparison of the energy spectra in the Kolmogorov scale at $Re_\lambda = 32$ and $Re_\lambda = 20$ of both incompressible turbulence and weakly compressible turbulence is shown in Figs. 4.9 and 4.10 respectively. Both the skewness and flatness of the velocity derivatives show good agreement with the trends observed in the incompressible turbulence results, see
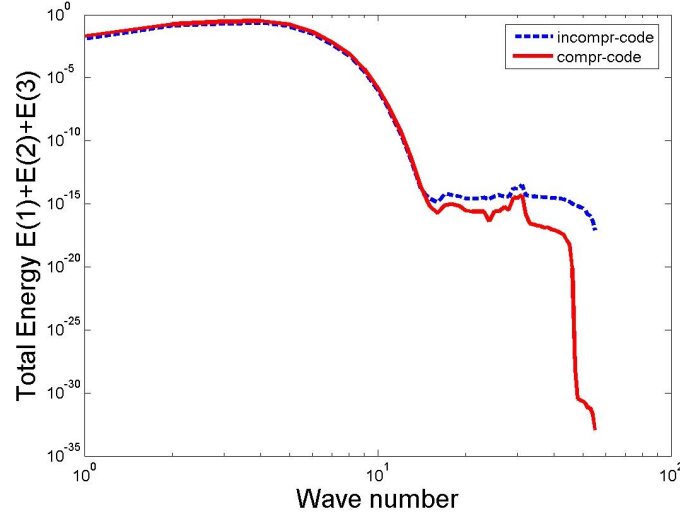
Figure 4.7. The initial energy spectrum, t=0.

Fig. 4.11. Subsequent to the initial large transient, the evolution results in a skewness in the range of approximately -0.4 through -0.6 as expected, see [68, 33].

Shown in Fig. 4.12 are the energy and enstrophy trend with time. The figure shows that the results of the weakly compressible turbulence simulation are in good agreement with incompressible turbulence results after some decay (precisely, t=10). The trend of dissipation rate, Taylor length scale, Kolmogorov length scale and Reynolds number based on the Taylor length scale shows good agreement between the incompressible turbulence simulation and weakly compressible turbulence simulation, see Fig. 4.13. The rms of vorticity also shows excellent agreement, see Fig. 4.14.

The three-dimensional weakly compressible turbulence results obtained using three different grid resolutions of 0.2 million grid cells (64^3), 2.1 million grid cells (128^3) and 16.8 million grid cells (256^3) are compared. Turbulence statisitical analyses carried out using these three set of data indicated good agreement and also
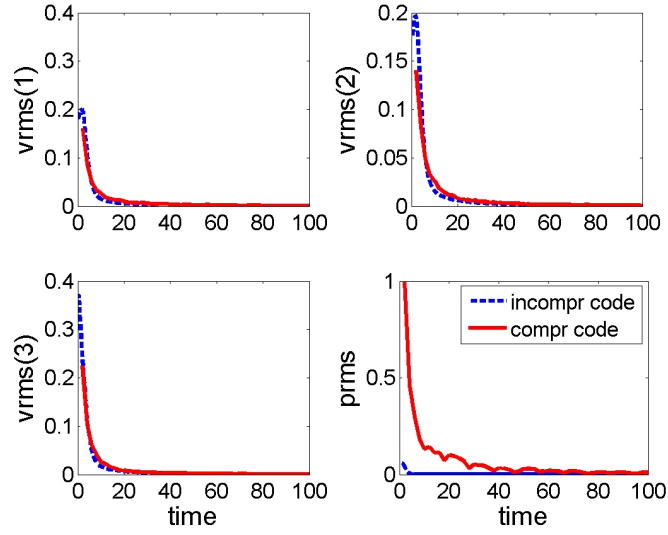
Figure 4.8. RMS of the velocities in the three directions and of the pressure.
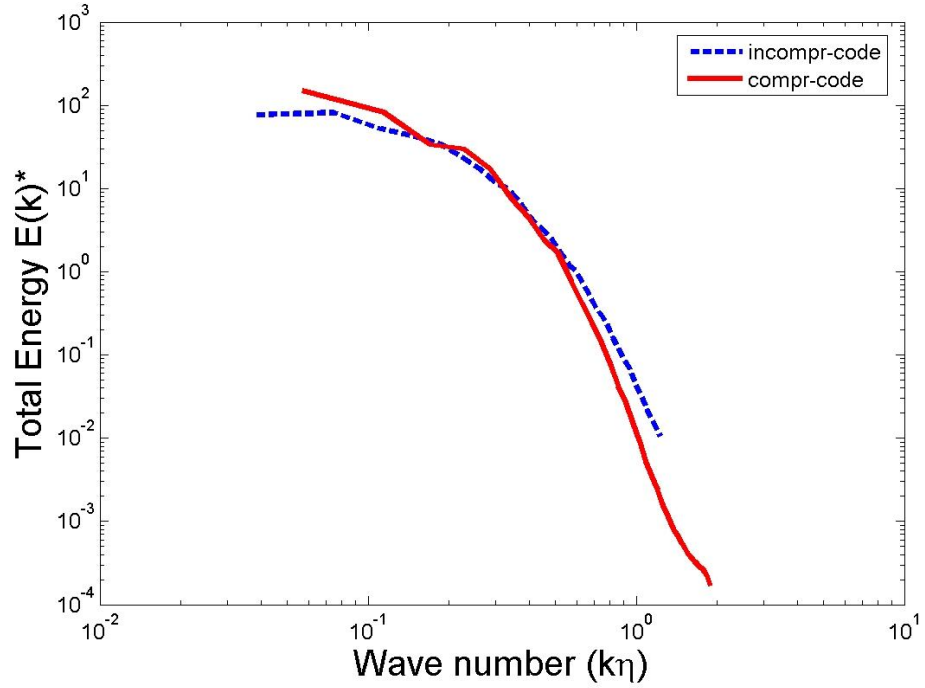

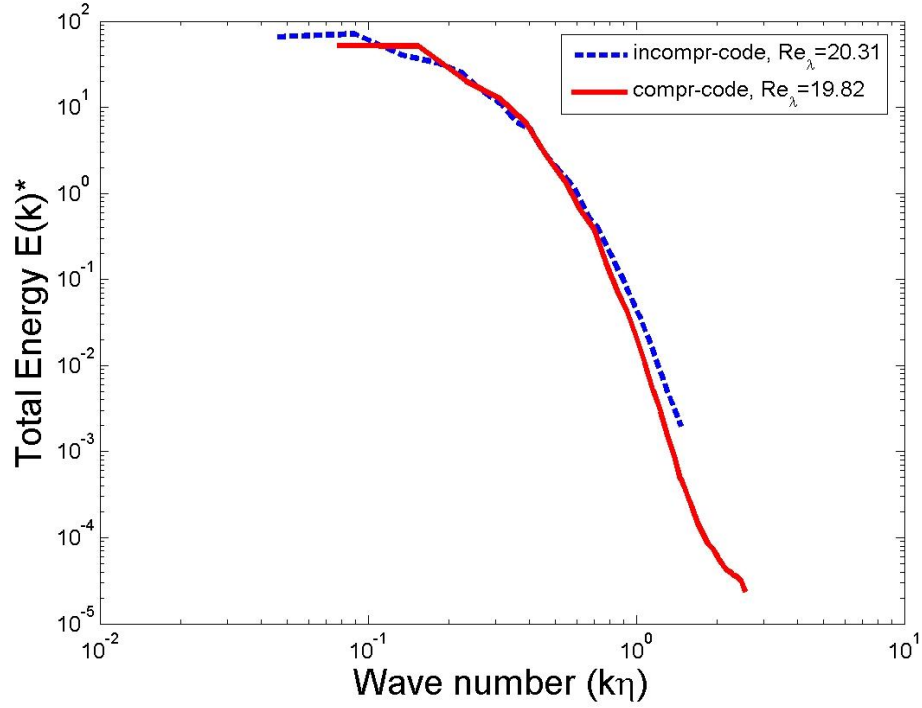Figure 4.9. The energy spectra in Kolmogorov scale at $Re_\lambda = 32$.

Figure 4.10. The energy spectra in Kolmogorov scale at $Re_\lambda = 20$.
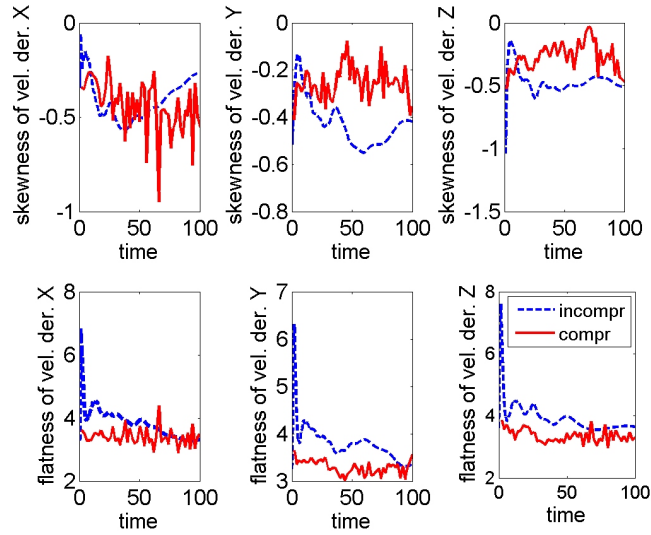

Figure 4.11. The skewness and flatness of the velocity derivatives.
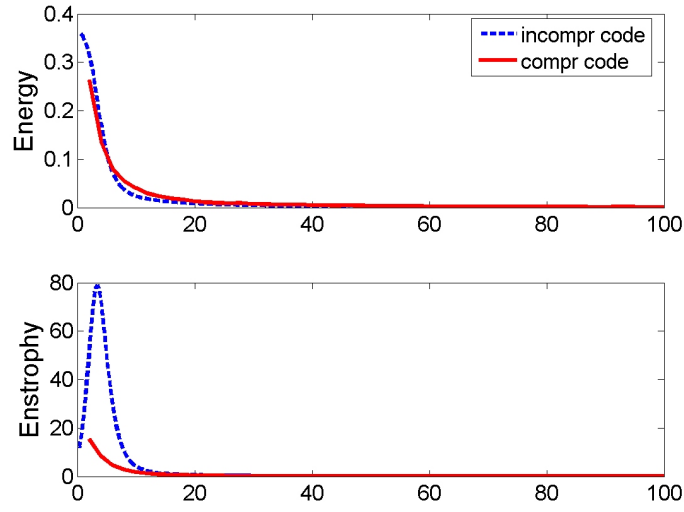
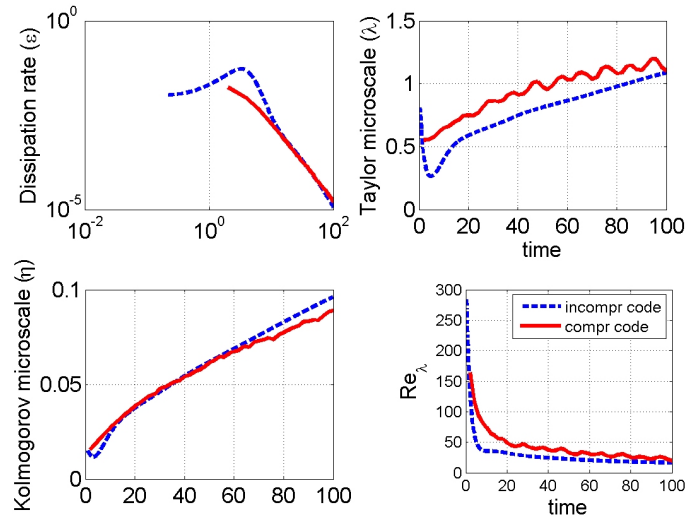Figure 4.12. The total energy and enstrophy pattern with time.

Figure 4.13. The trend of dissipation rate, turbulence length scales and Re_λ.
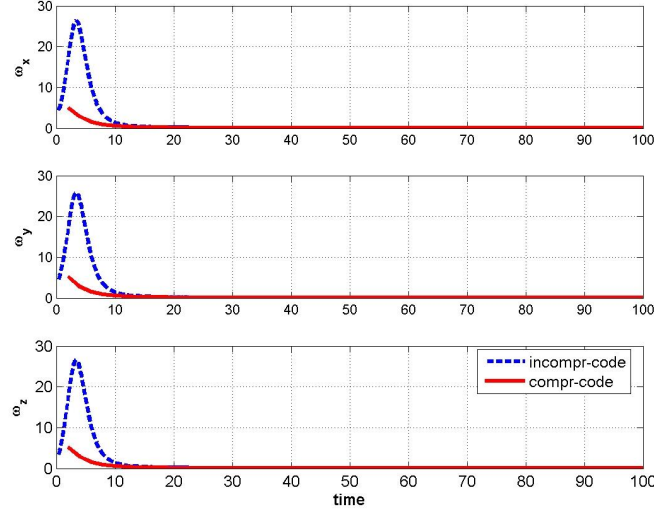
Figure 4.14. RMS value of the three vorticity components.

confirmed that the larger the number of grid cells the better the ability in capturing small scales. The initial energy spectra for the three grid resolution cases are shown in Fig. 4.15. The graph shows that the total energy spectra are identical for all the three grid resolutions upto a wavenumber of 10. Beyond wave number of 10, the plots show the data relevant to small scales. Higher the grid resolution longer the data of small scales. Indeed, the data beyond wave number of 10 seems to show unphysical small scales.

The total energy spectrum in the Kolmogorov scale at $Re_\lambda = 55$ and $Re_\lambda = 32$ for the three grid resolutions are shown in Fig. 4.16 and Fig. 4.17 respectively. Fig. 4.17 shows that the 128^3 and 256^3 resulted in pile up of energy at high wavenumbers and this indicates insufficient dissipation of energy. It is expected that in a higher Reynolds number case, there is an extended inertial range and it will fix the issue of energy pile up at high wavenumbers [68].
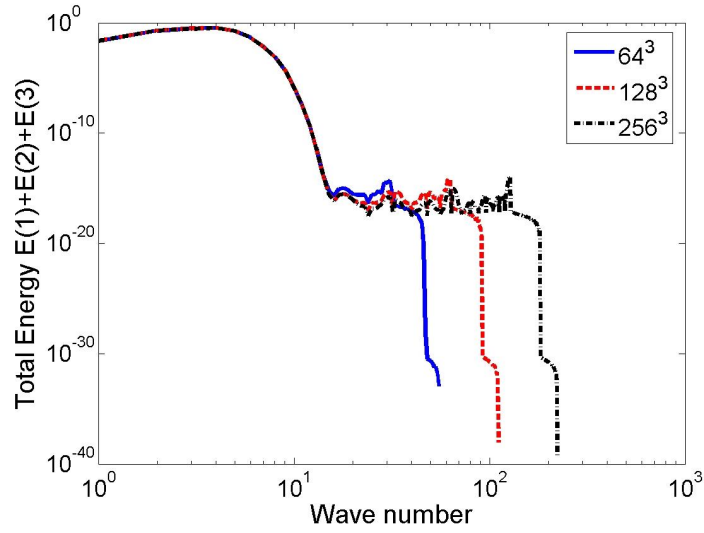
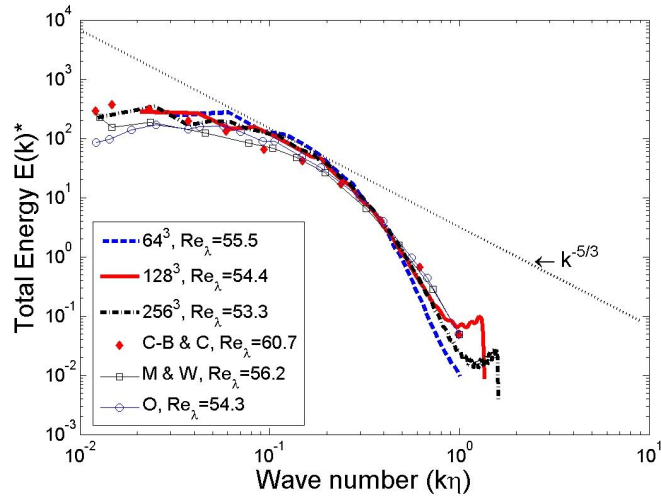Figure 4.15. The initial energy spectrum for the three grid resolutions.

Figure 4.16. The total energy spectrum in Kolmogorov scale at $Re_\lambda = 55$, C-B & C:Comte-Bellot & Corrsin; M & W: Mansour & Wray; O: Orlandi.
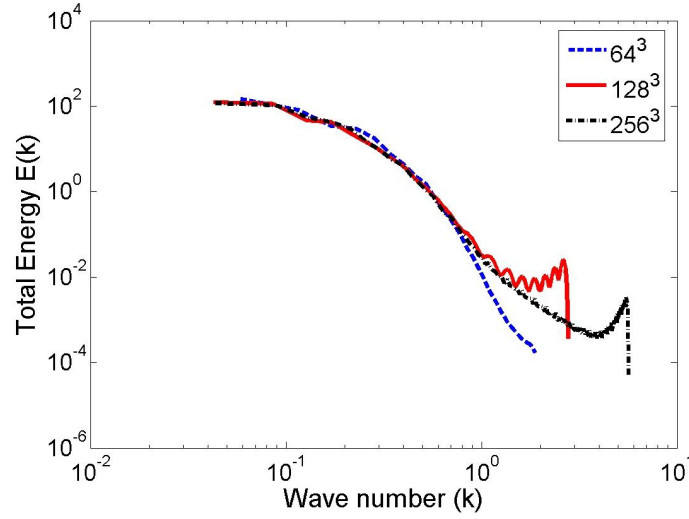
Figure 4.17. The total energy spectrum in Kolmogorov scale at $Re_\lambda = 32$.

Figure 4.16 also shows the comparison of the weakly compressible turbulence obtained using WENO solver with spectra from Compte-Bellot & Corrsin ($Re_\lambda = 60.7$) [144], Mansour & Wray ($Re_\lambda = 56.2$) [26] and Orlandi ($Re_\lambda = 54.3$) [27]. The figure shows that the results of grid resolution including and above 128^3 results in a trend which matches closely with the experimental data of Compte-Bellot & Corrsin and the other numerical simulations. The Kolmogorov $-5/3$ slope is shown as a dotted line. The data confirm that the flow evolves by Kolmogorov decay. Figure 4.18 shows typical initial energy spectra in the three directions for weakly compressible homogeneous isotropic turbulence using the 256^3 simulation. It indicates isotropy. The energy decay spectra of weakly compressible turbulence simulation using 128^3 grid resolution is shown in Fig. 4.19. The figure also indicates that the flow evolves towards a spectrum with a $k^{-5/3}$ law, i.e., Kolmogorov decay. The energy of fully developed isotropic turbulence decays in time while the scales of motion grow. As a result of the total kinetic energy(TKE) decay, the resulting Re_λ decreases with time.
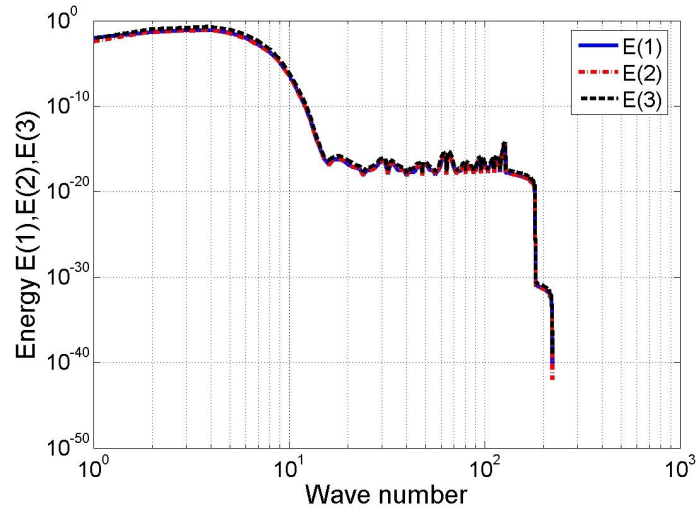
Figure 4.18. The energy spectra in three directions at $Re_\lambda = 118.5$, t=0, 256^3.

Consequently, a well resolved, fully developed field remain well resolved as the TKE decays. It also shows energy pile up at high wavenumbers in the plots corresponding to t=30, 60, and 100. This indicates insufficient dissipation of energy which could be due to insufficient Reynolds number [68].
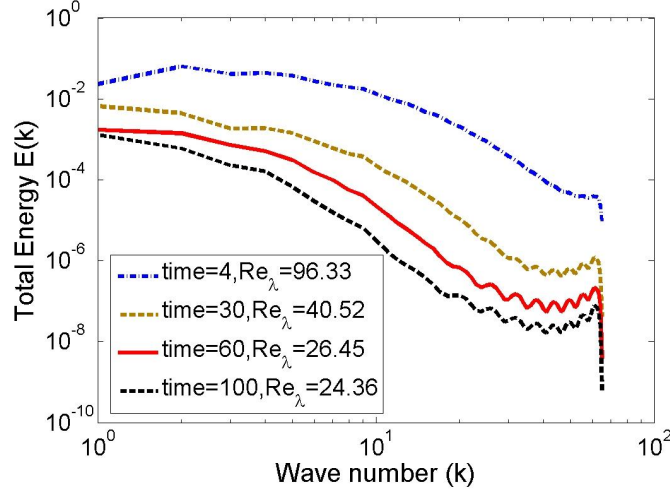
Figure 4.19. The total energy decay spectrum using the 128^3 case.

Turbulence statistics such as the dissipation rate, Reynolds number based on the Taylor length scale, Taylor length scale and Kolmogorov length scale for the three grid resolutions are displayed in Fig. 4.20. The trend of energy and enstrophy plot for the three grid resolution is shown in Fig. 4.21. The rms of the velocity in the three direction and the pressure are shown in Fig. 4.22. All the figures indicate isotropy. The rms of the three vorticity components are shown in Fig. 4.23.

The decay of the fluctuations of the thermodynamic parameters are shown in Fig. 4.24. The figure indicates that the 128^3 and 256^3 resolution results in identical decay trend. The turbulent Mach number is computed using the volume average of the turbulence data at each instant of time. Figure 4.25 shows the trend of turbulent Mach number with time of all the three grid resolution under examination. It is an indication of turbulence intensity. The turbulence decay causes decay of velocity, pressure, density and temperature and finally results in turbulent Mach number. Shown in Fig. 4.26 is the trend of Reynolds shear stress tensor $\tau_{ij} = \overline{\rho u_i' u_j'}$. In the
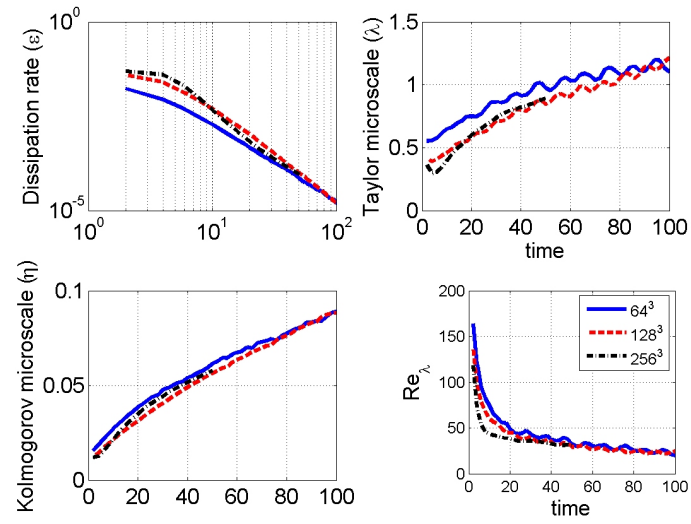
Figure 4.20. Trend of dissipation rate, turbulence length scales, and Reynolds number based on the Taylor length scale.
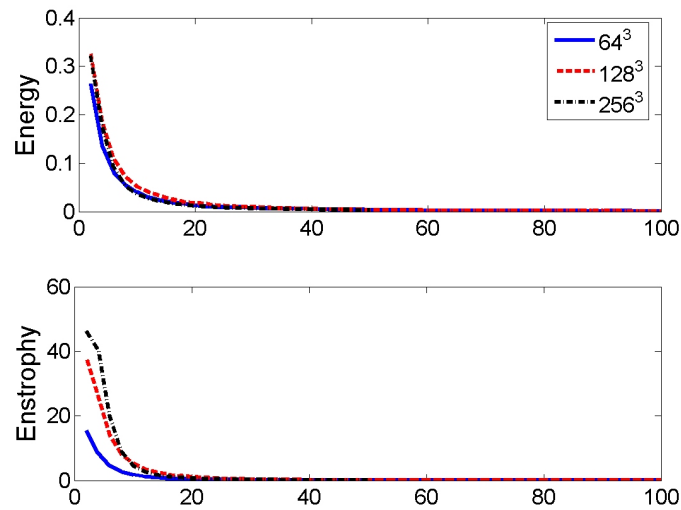

Figure 4.21. The energy and enstrophy decay.
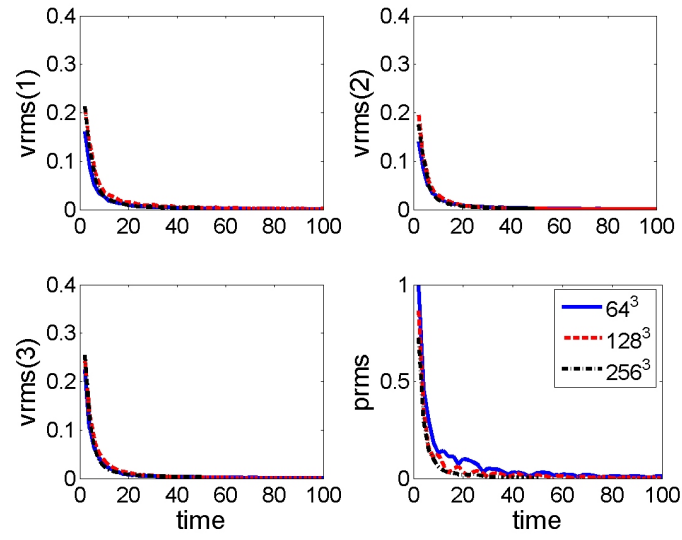
Figure 4.22. RMS of the three velocity components and the pressure.
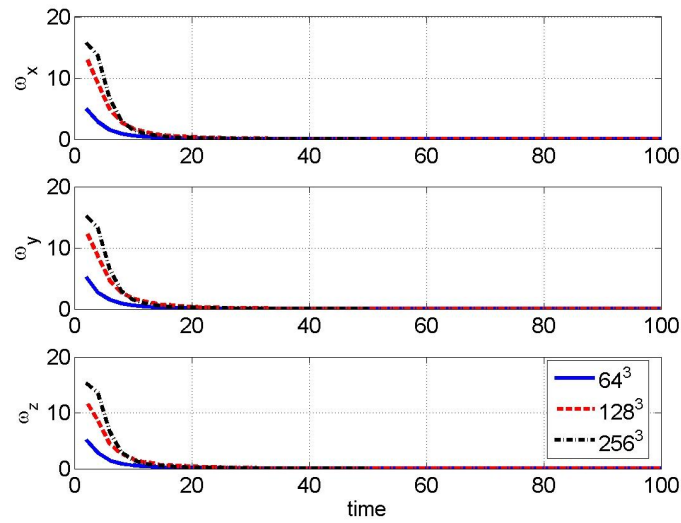
Figure 4.23. RMS of the three vorticity components.
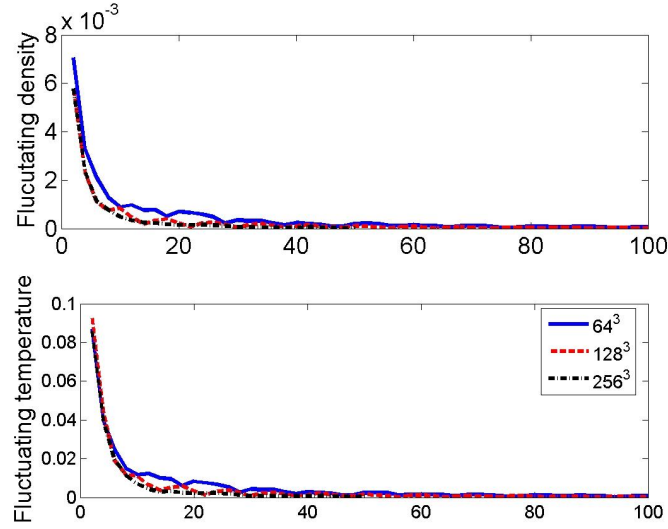
Figure 4.24. Trend of rms of density and temperature.

plot, ρ is the mean density obtained at any given time instant. These trends are identical to the trend observed in published numerical results [83].

Iso-surface of three-dimensional enstrophy is plotted with the help of the visualization support team at TACC. The volume vizualisation package 'VisIt' is used to obtain the plots. The plots are made by volume rendering of the iso-surface values of the enstrophy with the onion-peeling option. Usually, visualizations of two-dimensional projections of spatially complex three-dimensional fields reveal important details about the instantaneous structure of the turbulence. But, it is often difficult to interpret the three-dimensional structure from these images. The best method to examine and gain better understanding of these structures is to view animations of the same. Nevertheless, instantaneous visualization did provide useful information of the turbulent structures. Vorticity is an important parameter to depict the small scales. Comparison of Fig. 4.27 and Fig. 4.28 illustrates the effect of energy decay with time which is indicated by a fewer number of long thin tubular structures. Com-
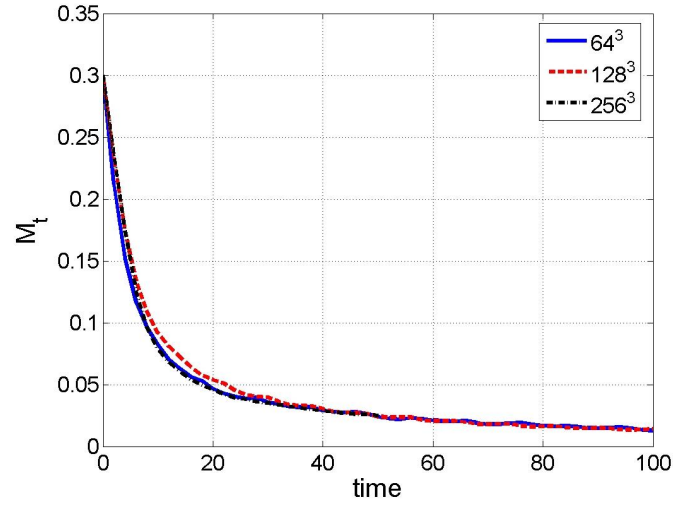
Figure 4.25. Trend of turbulent Mach number.
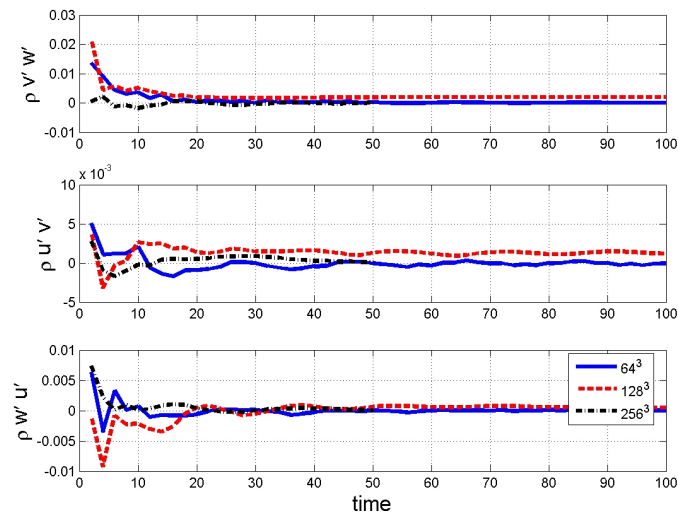
Figure 4.26. Trend of Reynolds stress tensor.
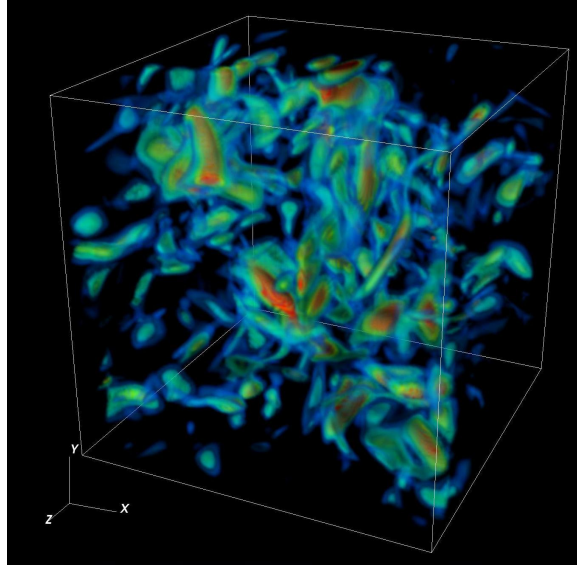
Figure 4.27. Snapshot of the three-dimensional enstrophy using the 128^3 simulation at $Re_\lambda = 34.85$, t=40.

parison of Fig. 4.27 and Fig. 4.29 shows better resolution of small scales result in 256^3 grid resolutions which are indicated by more number of much longer thin tube like structures. In general, all these three plots illustrate the straining of vortices which is a characteristics of three-dimensional turbulence. Finally, the computational requirement for the turbulence simulation is given in Table 4.1. In the table, N_x, N_y, N_z are the number of grids in the x, y, z directions respectively and the product of l_x, l_y and l_z gives the total number of processors used.

Table 4.1. Computational requirement.

Case	N_x	N_y	N_z	l_x	l_y	l_z	time consumed hr:min
1	32	32	32	2	2	2	0:24
2	64	64	64	4	4	4	9:35
3	128	128	128	6	6	6	30:00
4	256	256	256	6	6	6	141:30
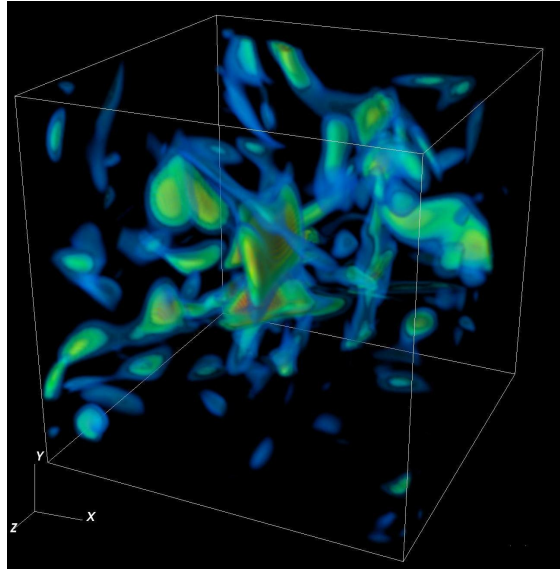
Figure 4.28. Snapshot of the three-dimensional enstrophy using the 128^3 simulation at $Re_\lambda = 24.41$, t=90.

Figure 4.29. Snapshot of the three-dimensional enstrophy using the 256^3 simulation at $Re_\lambda = 32.76$, t=40.

Hence, the accomplishement of simulation of the weakly compressible homogeneous isotropic turbulence revealed the suitability of WENO scheme. The grid independence study revealed that a minimum of 128^3 resolution is salient to capture the turbulence with reasonable accuracy and hence both the shock-turbulence interaction and detonation-turbulence interaction used 128^3 grid cells.
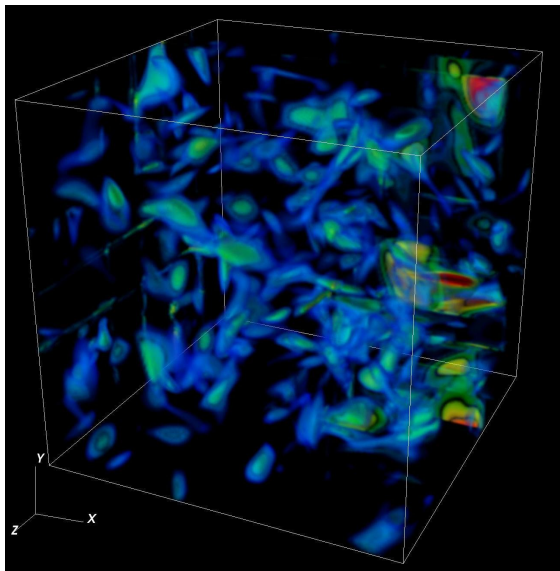
4.5   Interaction of Shock Wave with Compressible HIT

The interaction of a shock wave with compressible HIT using DNS is carried out as the last validation for the Navier–Stokes solver. The simulation is carried out with several grid resolutions: 32^3, 64^3, 128^3. Zero-order flux boundary condition is imposed in the streamwise direction while periodic boundary conditions are imposed in the y and z directions. Three different shock Mach numbers (1.5, 3.0, 4.156) were employed in this study. The computational domain is a cube with a dimension of $(2\pi \times 2\pi \times 2\pi)$. An evenly spaced Cartesian grid discretizes this domain into N^3 points. The following four parameters govern the generation of the initial turbulent field, viz., density, turbulent Mach number, pressure, and the Reynolds number based on the Taylor length scale. Initialization of isotropic turbulence begins with uniform density and pressure and completely random velocity values. The initial energy spectra are obtained using the Mansour–Wray energy model. It is deemed that a field has reached a proper state of isotropic turbulence when the skewness of the velocity derivatives become the desired value observed in the experimental data. The velocity derivative based skewness value in three directions were around -0.4 to -0.5. It must be remembered that the velocity derivative skewness value depends on several factors causing the turbulence such as compressibility, Re_λ, velocity, etc and hence one must be careful in selecting the value. Once the turbulence simulation reaches the desired skewness value, a normal shock wave is allowed to propagate through the cube. The

WENO scheme's capability to capture accurately the flow discontinuties is made use of in this interaction analysis.

The length scale L is $1/k_0$, the density scale is the mean pre-shock value, the velocity scale is the turbulence rms velocity, and the pressure scale is the product of the density scale and velocity scale squared. The post- and pre- shock conditions in the simulation of shock–turbulence case are given below:

$$p_l = \frac{u_{rms}^2 \left(2\gamma M_s^2 - \gamma + 1\right)}{\left(\gamma^2 + \gamma\right) M_t^2} \tag{4.12a}$$

$$\rho_l = \frac{M_s^2 \left(1 + \gamma\right)}{2 + \left(\gamma - 1\right) M_s^2} \tag{4.12b}$$

$$u_l = \frac{2u_{rms} \left(M_s^2 - 1\right)}{\left(1 + \gamma\right) M_s M_t} \tag{4.12c}$$

$$p_r = \frac{u_{rms}^2}{\gamma M_t^2} \quad ; \quad \rho_r = 1 \quad ; \quad u_r = 0 \tag{4.12d}$$

Here, M_s and M_t are the shock and turbulent Mach numbers respectively.

4.5.1 Results

The influence of the shock wave on the nature of the homogeneous isotropic turbulence is investigated. Figure 4.30 shows the total energy spectrum before (t=0) and after the propagation of the shock wave(t=1). Shock Mach number is 4.156 in this case. Significant scale dependent amplification is observed: more amplification at small scales and moderate scales than at large scales. The analysis of the energy in three different directions revealed that more amplification is seen with energy in longitudinal direction than those in transverse directions. The total energy levels were raised at high wave numbers as also observed by Lele et al[9]. It must be noted that the decay of post-shock spectrum is also observed.
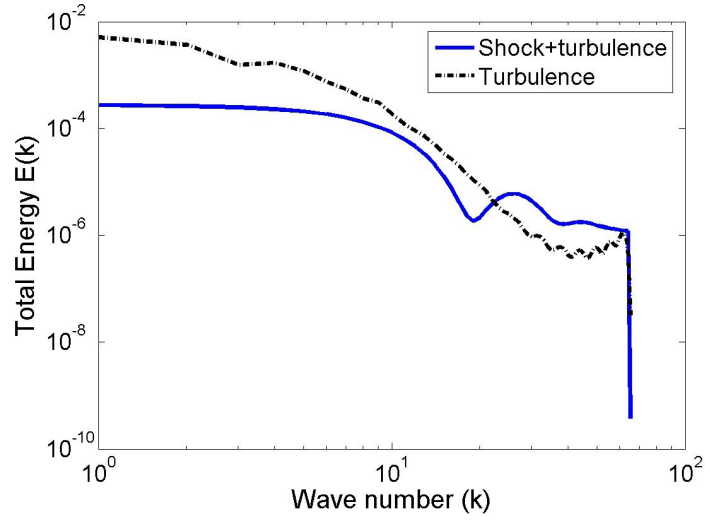
Figure 4.30. Comparison of total energy spectrum of pre- and post-shock propagation, 128^3.
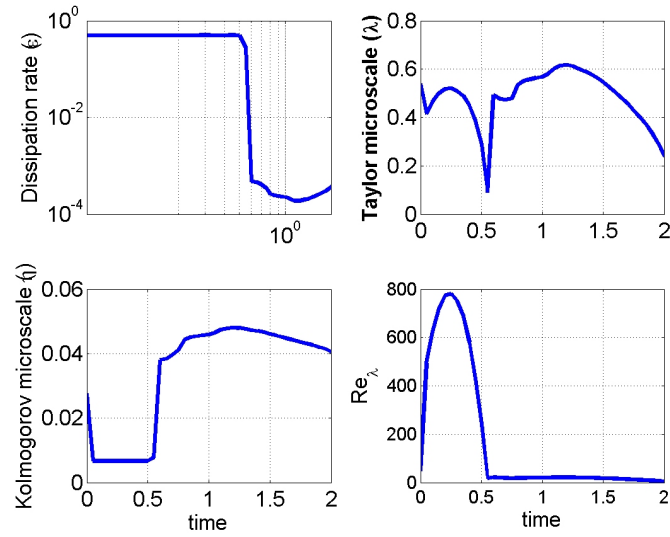
Figure 4.31. Trend of dissipation rate, turbulence length scales and Re_λ.
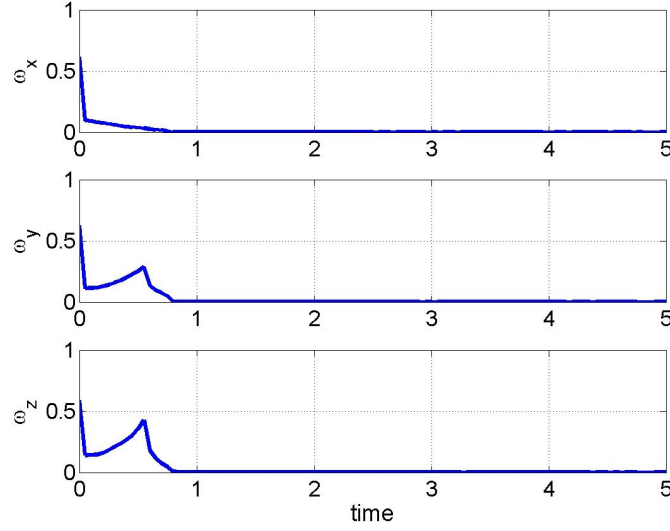
Figure 4.32. RMS of the three vorticity components.

Figure 4.31 illustrates the trend of dissipation rate, and other turbulence statistical parameters. It shows the interaction ensued an increase in length scales and sudden drop in dissipation rate. As the shock propagates through the turbulent field, the large scale turbulent motions are enhanced more than the small scale motions, leading to the overall increase of turbulence length scales, especially of microscales. Figure 4.32 shows that the transverse vorticities increase drastically upto t=0.7 and then decreases gradually whereas the streamwise vorticity is marginally affected by the shockwave. The marginal increase in streamwise vorticity is a nonlinear process occuring due to the intensified vorticity in the y and z directions. This trend is corroborated by comparison with numerical results of Lee et al. [145, 146] and Cohen et al [84]. However, linear interaction analysis predicts no amplification of the streamwise vorticity [145, 146].

Figure 4.33 depicts the trend of Reynolds stresses with shock turbulence interaction. The post-shock data indicates that the Reynolds stress about streamwise
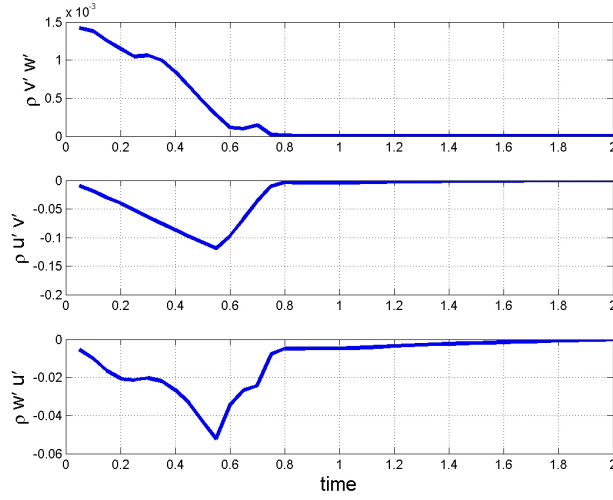
Figure 4.33. Trend of Reynolds stresses in shock-turbulence interaction case.

direction decreases continously whereas the Reynolds stresses about transverse directions increase, see Lee et al. [145] and Jamme et al. [83]. Figure 4.34 depicts the plot of shock–turbulence interaction using 32^3 grid resolution with deformation. The initial turbulent Mach number was 0.05. Shock Mach number is 1.5 in this case study. The comparison of the two figures in the subfigure also shows the propagation of the shock wave. The ordinate refers to the density. Due to the interaction of the turbulence, corrugation of the shockwave is observed with density plot.

Effect of shock Mach number on energy is shown in Fig. 4.35. It shows the post shock turbulence total energy spectra at time=1 for both shock Mach numbers of 3.0 and 4.156. It reveals that higher shock Mach number results in rapid energy cascade. The influence of shock Mach number on turbulence statistics are shown in Figure 4.36. The turbulent length scale show more amplification with large shock Mach number because the velocity change is more in the case of higher shock Mach number. Rapid dissipation is observed in higher shock Mach number interaction.
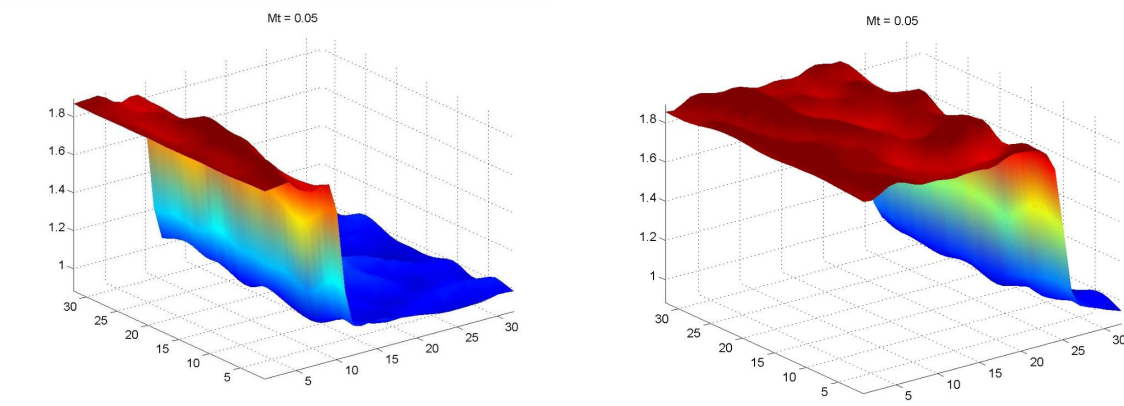
Figure 4.34. Effect of turbulence on shockwave due to their interaction, t = 0.2 (left) and t = 0.6 (right).
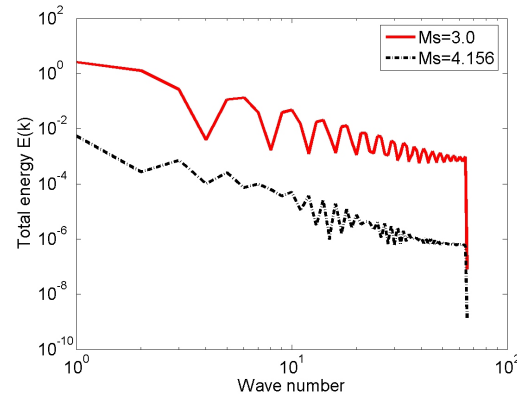
Figure 4.35. Effect of shockwave on turbulence, Energy spectrum at t=1.
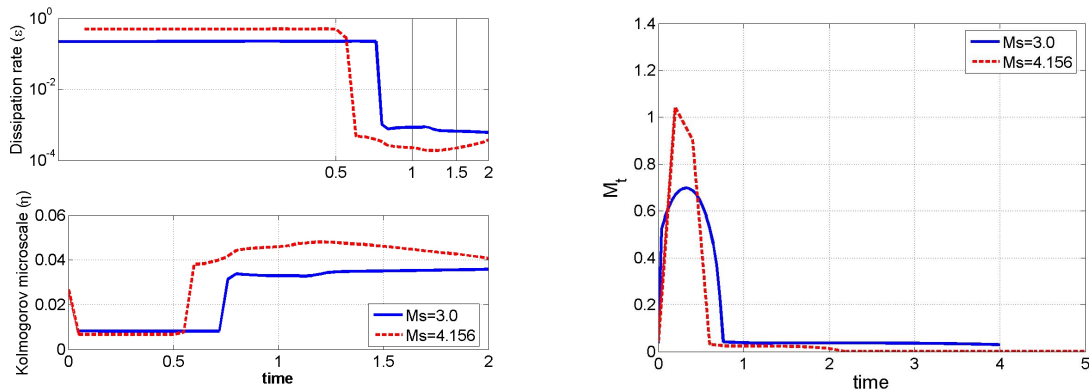
Figure 4.36. Effect of shockwave on turbulence, turbulence statistics (left) and turbulent Mach number (right).

Turbulent Mach number also indicates higher amplification with higher shock Mach number case.

Hence, the interaction of the turbulence with shockwave is validated and a good agreement of the energy spectra, vorticity spectra, and other turbulence statistical parameters with published research are observed.

CHAPTER 5

INTERACTION OF DETONATION WAVE WITH CHIT

5.1 Computational Setup for DNS of Detonation Wave with CHIT

The DNS code was extended to study the interaction of a detonation wave with CHIT. All the numerical and initial conditions were the same as for the shock interaction case described in the previous chapter. Moreover, the viscous decay process was characterized by the Reynolds, Lewis and Prandtl numbers. A power law with an exponent of $n = 0.7$ was used for the viscosity–temperature relation. The Lewis and Prandtl numbers are independent of the fluid solution, leading to linear scaling between viscosity, thermal conductivity and diffusivity.

The turbulent length scale $L = 1/k_0$, the density scale is the mean pre-detonation value, the velocity scale is the turbulence velocity rms, and the pressure scale is the product of the density scale and velocity scale squared. These scales are defined pre-detonation propagation. The pre- and post- detonation conditions in the simulation of detonation–turbulence are given below

$$\rho_r = 1, \quad p_r = \rho_r \frac{u_{rms}^2}{\gamma M_t^2}, \quad u_r = -M_{Det}\sqrt{\frac{\gamma p_r}{\rho_r}} \tag{5.1a}$$

$$p_l = \frac{1 + \gamma M_{Det}^2 + \sqrt{\gamma \left(\gamma \left(M_{Det}^2 - 1\right)^2 - 2\left(\gamma^2 - 1\right)\tilde{\lambda}M_{Det}^2 Q\right)}}{\gamma + 1} \tag{5.1b}$$

$$u_l = \frac{M_{Det}\sqrt{\gamma p_l}\left(\gamma\left(2 + (\gamma - 1)M_{Det}^2\right) + 2(\gamma - 1)\tilde{\lambda}Q\right)}{\gamma + \gamma^2 M_{Det}^2 + \sqrt{\gamma\left(\gamma\left(M_{Det}^2 - 1\right)^2 - 2\left(\gamma^2 - 1\right)\tilde{\lambda}M_{Det}^2 Q\right)}} \tag{5.1c}$$

$$\rho_l = \rho_r \frac{u_r - w_s}{u_l - w_s} \tag{5.1d}$$

where $\tilde{\lambda}$ is reaction progress and is given by the expression $\tilde{\lambda} = \int_0^x \frac{r(T)}{u}$. $\tilde{\lambda} = 0$ corresponds to completely unburnt state and $\tilde{\lambda} = 1$ corresponds to completely burnt state. Also, M_{Det} is given by $M_{Det} = D/\sqrt{\gamma P_0/\rho_0}$.

5.1.1 Effect of Heat Release

The study was carried out with three values of the non-dimensional heat release Q, three values of the non-dimensional activation energy E and with three different grid resolutions as shown in Table 5.1. The two parameters of greatest interest are the turbulent Mach number M_t and a new non-dimensional number N which represents the ratio of the reaction-to-turbulence length scale. These parameters establish a relationship in the characteristic lengths and times between the two fundamental processes, viz., the detonation and the turbulence. The viscous decay is in fact too slow to contribute to the interaction; thus the Reynolds, Lewis and Prandtl numbers are fixed. The number of points in the half-reaction length was maintained as 12 in the 128^3 grid resolution case. The other input parameters were $f = 1.2$, $k_p = 3$, $\sigma = 4$, $Pr = 0.72$, $Re = 1000$, $Le = 1$, and $\gamma = 1.2$. As previously done in the shock-turbulence interaction case, the detonation wave is allowed to propagate through the computational domain once the turbulence simulation reaches the desired skewness value as seen in experiments. The skewness of the velocity derivative in the three directions pre-detonation were -0.48, -0.51 and -0.49 respectively for the 128^3 grid resolution case. It employs coupled reaction-transport solving method. Time of flight of the detonation wave through the computational domain for the cases of $\{E, Q\} = \{10, 10\}$, $\{17, 17\}$, and $\{20, 20\}$ are 0.8335, 0.6673, 0.6212 respectively. The values $\{E, Q\} = \{17, 17\}$ correspond to the fuel of $H_2 - O_2 - N_2$ combination. By varying the value of N_2, the value of Q can be varied. The variation in amount of catalyst results in variation in activation energy.

Table 5.1. The initial condition of the numerical simulations.

Case	N_x	N_y	N_z	M_t	Re_λ	E	Q	M_{Det}
1	32	32	32	0.0534	25.72	10	10	3.327
2	32	32	32	0.0534	25.72	17	17	4.156
3	32	32	32	0.0534	25.72	20	20	4.464
4	64	64	64	0.25	70.21	17	17	4.156
5	128	128	128	0.064	49.35	10	10	3.327
6	128	128	128	0.064	49.35	17	17	4.156
6	128	128	128	0.064	49.35	20	20	4.464

Figure 5.1 shows the variation of the turbulent Mach number with the non-dimensional time for both shock–turbulence and detonation–turbulence interactions. The shock–turbulence interaction was evaluated with a freestream Mach number identical to that of the detonation analysis, $M_0 = 4.156$. The figure also compares the post-interaction total energy spectrum. The black dashed line indicates the turbulence before passage of detonation and the corresponding time is taken as t=0. This turbulence data is obtained using 128^3 simulation results discussed previously. Both the shock-turbulence interaction and detonation-turbulence interaction use identical initial turbulence conditions. The results reveal that the detonation–turbulence interaction(t=1) shows more amplification in the energy in the moderate to high wave number range whereas the shock–turbulence interaction(t=1) shows amplification in the high wave number range only. Precisely, the interaction resulted in significant scale dependent amplification as it was observed in shock-turbulence interaction: more amplification at moderate to small scales than at large scales. The analysis of the energy in three different directions revealed that more amplification is seen with energy in longitudinal direction than those in transverse directions, see Figure 5.2.
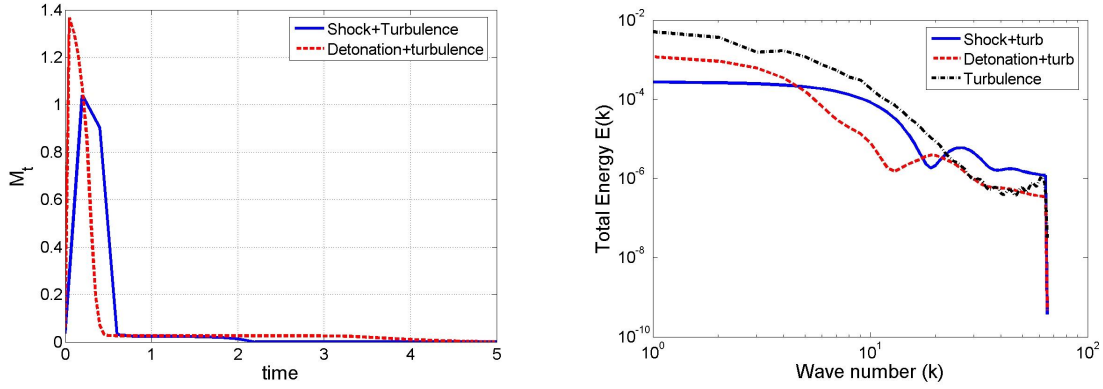
Figure 5.1. Comparison of shock–turbulence and detonation–turbulence interaction, 128^3, Turbulent Mach number (left) and Energy decay spectra (right).

Figure 5.3 shows an earlier drop in the dissipation rate that is more gentle in the detonation–turbulence interaction than in the shock–turbulence interaction. The figure also shows that there is a higher level in the Kolmogorov length scale for the detonation–turbulence interaction than for the shock–turbulence interaction. The effect of heat release and activation energy on the statistical parameters of the turbulence and energy are examined. Figure 5.4 illustrates that the heat release leads to an increased level of fluctuation in the post-shock region. The right side of the figure shows that the rms values of the velocity and pressure go hand-in-hand with the heat release. The rms velocity in the streamwise direction is initially three orders of magnitude higher than those in the transverse directions immediately after the wave passage. However, the rms values decrease rapidly and reaches values comparable to the transverse directions when $t > 0.5$. The rapid straining in the axial direction therefore results in considerable nonisotropy but the return to isotropy also occurs very rapidly.

The detonation–turbulence interaction results in a sharp drop in vorticity fluctuation initially and which then rose moderately until the resumption of the turbulence
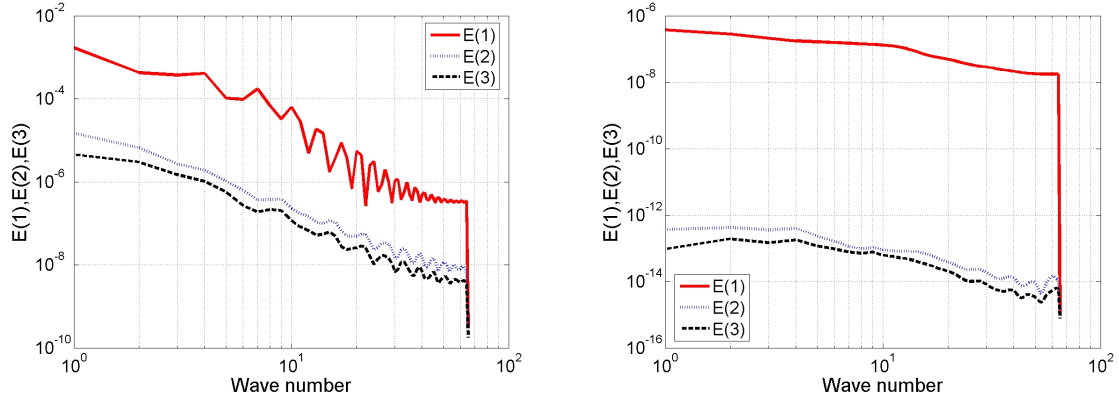
Figure 5.2. Detonation–turbulence interaction of the case with E=17, Q=17, 128^3, t=1 (left) and t=5 (right).

decay. Increasing the heat release speeds up the rise and fall of this vorticity "hump," see Fig. 5.5. The right side of the figure indicates the change in the Reynolds stresses due to detonation–turbulence interaction. The variation in heat release did not have much effect on the trend of Reynolds stresses with time.

The variation of heat release and activation energy resulted in higher amplification of thermodynamic parameters, see Fig. 5.6. The right-side subfigures indicate that the detonation–turbulence interaction also resulted in an increase in turbulence length scales (Kolmogorov length scale and Taylor microscale). The higher the heat release, the greater is the length scale increase. As the detonation wave propagates through the turbulent field, the large scale turbulent motions are enhanced more than the small scale motions, leading to the overall increase of turbulence length scales, especially of microscales. Further, the drastic drop in dissipation rate indicates that there is a drastic drop in turbulent kinetic energy due to the detonation–turbulence interaction. There is an increase in the dissipation of turbulent kinetic energy with an increase in the heat release parameter. The Reynolds number based on the Taylor
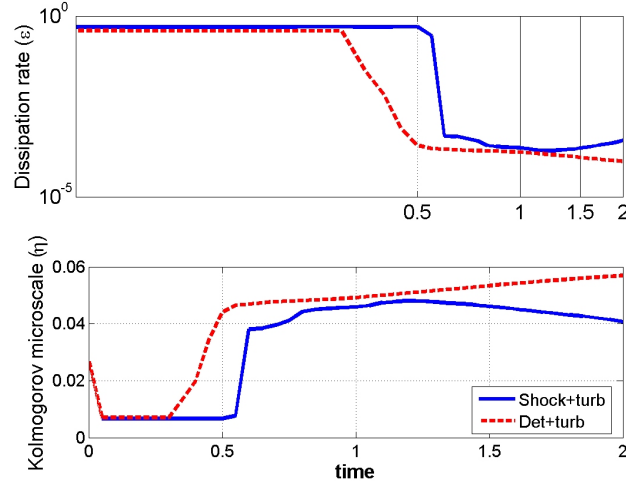
Figure 5.3. Comparison of dissipation rate and Kolmogorov length scale.

microscale is higher for higher heat release and there is a faster decline in Re_λ with an increase in the heat release parameter.

The post-detonation total energy spectrum for the turbulence–detonation interaction is shown in Fig. 5.7. The left subfigure corresponds to the post-detonation spectrum obtained at $t = 1$. It indicates that the energy at high wave numbers varies inversely with the heat release. The spikes indicate the occurence of resonance. The total energy spectrum plot obtained at $t = 5$ indicates that the energy decay is faster in the highest energy release whereas it is slower in the lowest heat release. It also showed rapid cascade of energy to small scales.

Due to the interaction of the turbulence, the detonation wave becomes corrugated as seen, for example, in density plots. Figures 5.8 and 5.9 depict isometric plots of the detonation–turbulence interaction using the 64^3 grid. The initial turbulence Mach number was maintained as 0.25 in this case. The comparison of the two figures in the subfigure also shows the propagation of the detonation wave. The
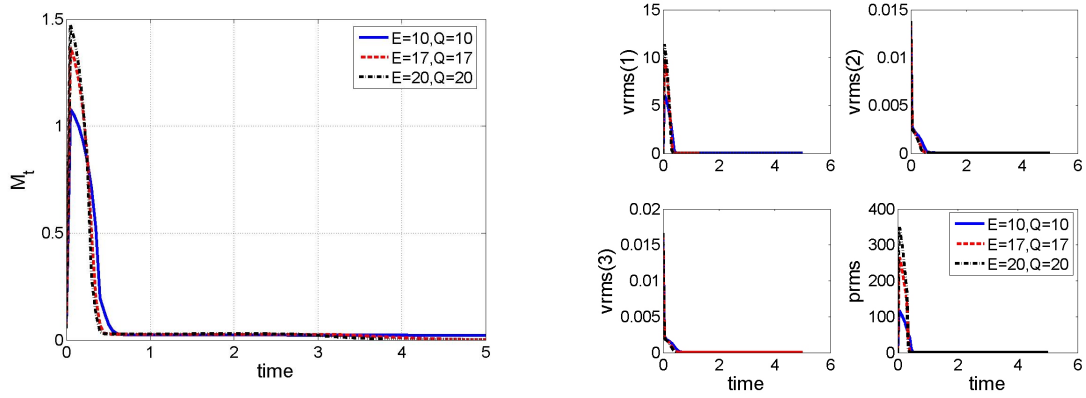
Figure 5.4. Effect of heat release on turbulent Mach number and rms of velocities and pressure.
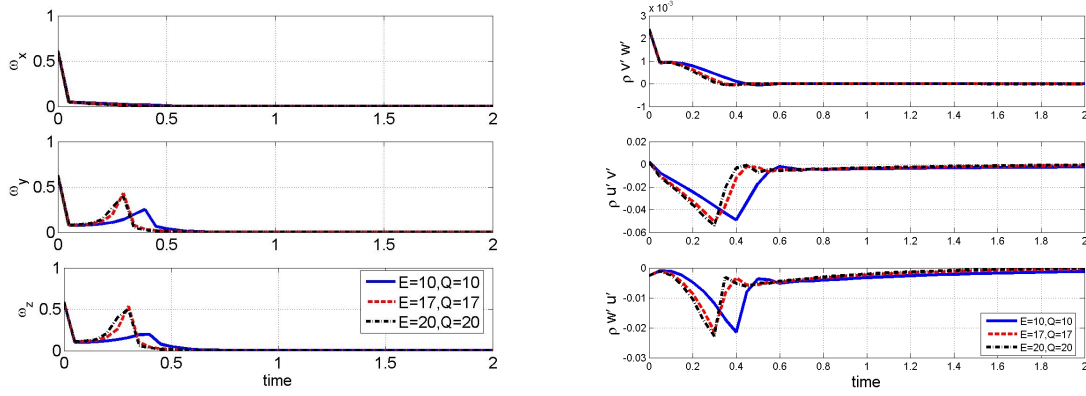
Figure 5.5. Effect of heat release on rms of vorticity and Reynolds stresses.
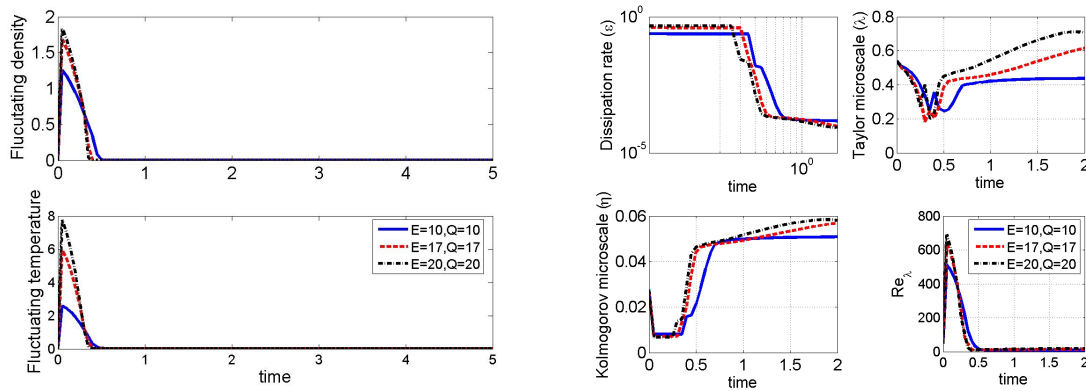
Figure 5.6. Effect of heat release on rms of thermodynamic parameters and turbulence statistics.
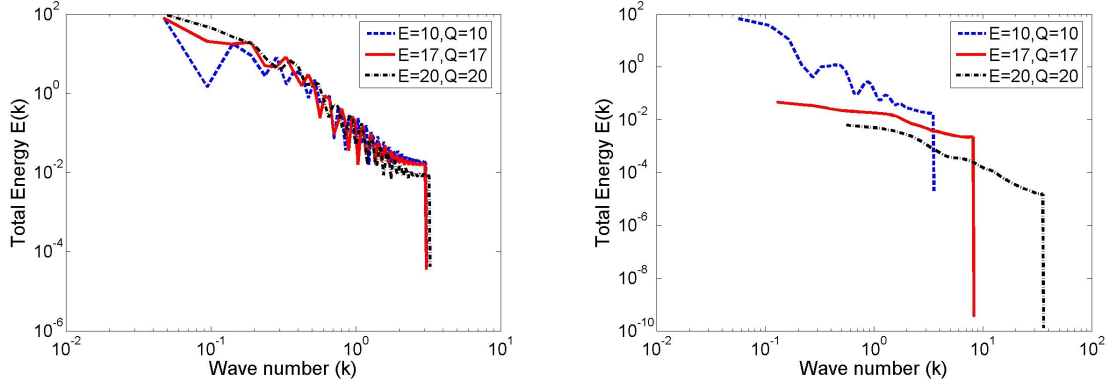
Figure 5.7. Effect of heat release on energy spectra, 128^3, $t = 1$ (left) and 5 (right).
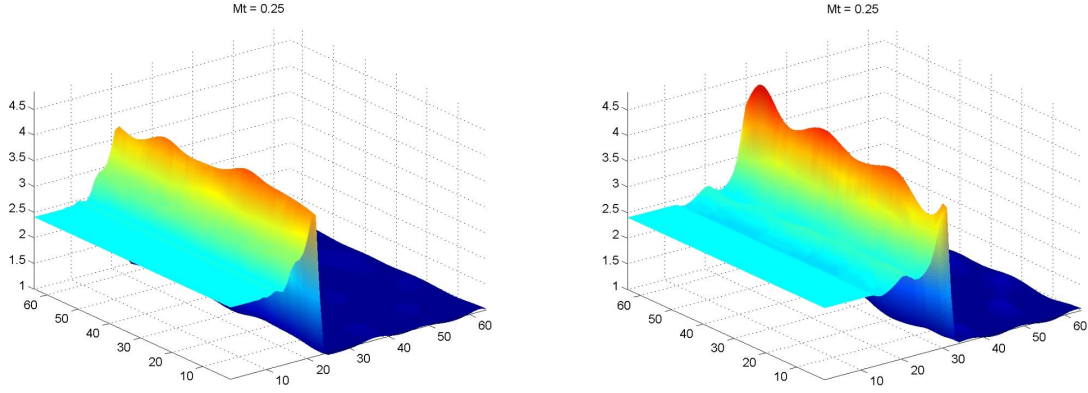
Figure 5.8. Effect of turbulence on detonation wave, $t = 0.13$ (left) and 0.25 (right).

ordinate refers to the density. The two horizontal axes indicate x and y directions respectively.

5.1.2 Effect of N

Three different N values of 0.95, 1.0 and 1.5 were used to investigate its effect on detonation–turbulence interaction. The numerical setup was the same as in the previous section. The non-dimensional heat release was maintained as 17 and the non-dimensional activation energy was taken as 17. The grids were 128^3. The left subfigures of Fig. 5.10 depicts the influence of N on the turbulence statistical param-
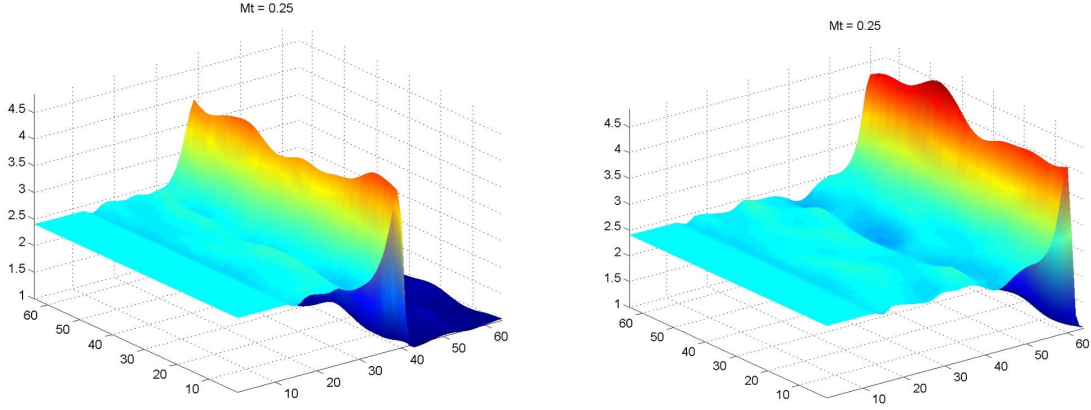
Figure 5.9. Effect of turbulence on detonation wave, $t = 0.5$ (left) and 0.6 (right).
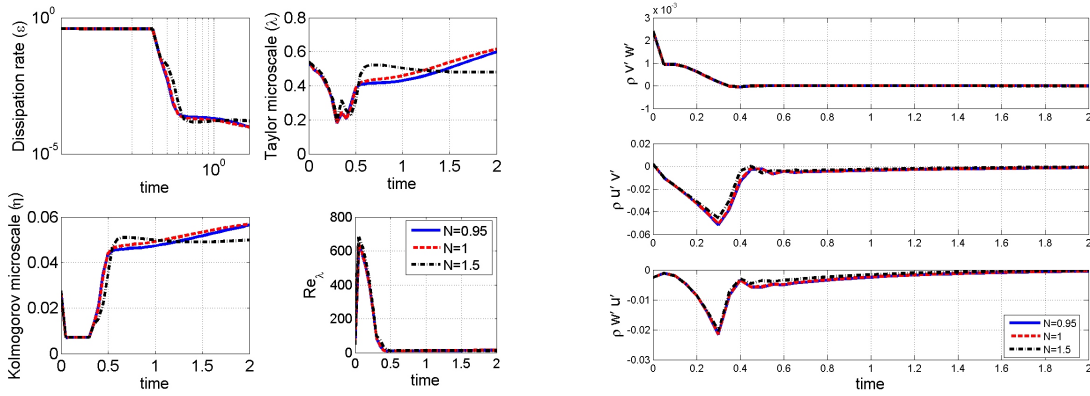
Figure 5.10. Effect of N on turbulence statistical parameter (left) and Reynolds stresses (right).

eters. There is a monotonous increase in the Taylor and Kolmogorov microscales with N while the reaction length scale and the turbulence length scale are close to each other. When N is very high, the turbulence microscales show a long-term decrease with time in the post-detonation region. The right subfigure shows that the variation in N hardly affects the trend of Reynolds stresses. The statistics are obtained as volume averaged result in the computational domain at any given time instant.

The left subfigures of Fig. 5.11 shows that the rms of the velocity components are hardly affected by the variation in N although the rms pressure plot shows a
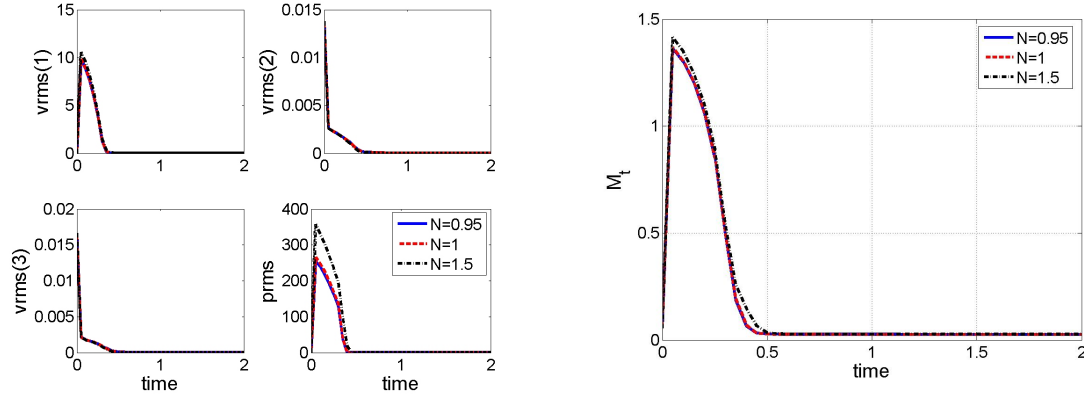
Figure 5.11. Influence of N on rms of the velocity and pressure (left) and turbulent Mach number (right).

significant rise at the highest N value followed by a rapid decay. The right subfigure of Fig. 5.11 indicates that the turbulent Mach number rise is proportional to N. It confirms that the intensity of turbulence increases with N. The variation in fluctuating thermodynamic parameters go hand in hand with the variation in N, see left subfigures of Fig. 5.12. The variation in N did not result in any change in the trend of the vorticity components, see right subfigures.

Figure 5.13 depicts the total energy spectra with time and the influence of N. Observation of the post-detonation energy spectrum at t=1 revealed hardly any change due to N. But the observation after considerable time (precisely, t=5) from the propagation of the detonation wave showed that the energy decay with wave number is more rapid when $N = 1.5$.

It must be noted that the simulation of each run of detonation wave with turbulence consumed 2 hours and 30 minutes on 216 processors (ie., 54 nodes) for the grid resolution of 128^3.
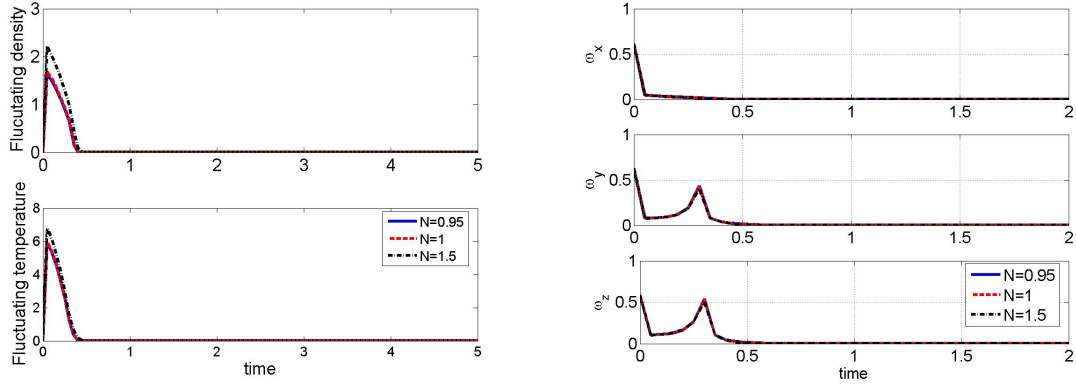
Figure 5.12. Influence of N on thermodynamic parameters (left) and rms of vorticity (right).
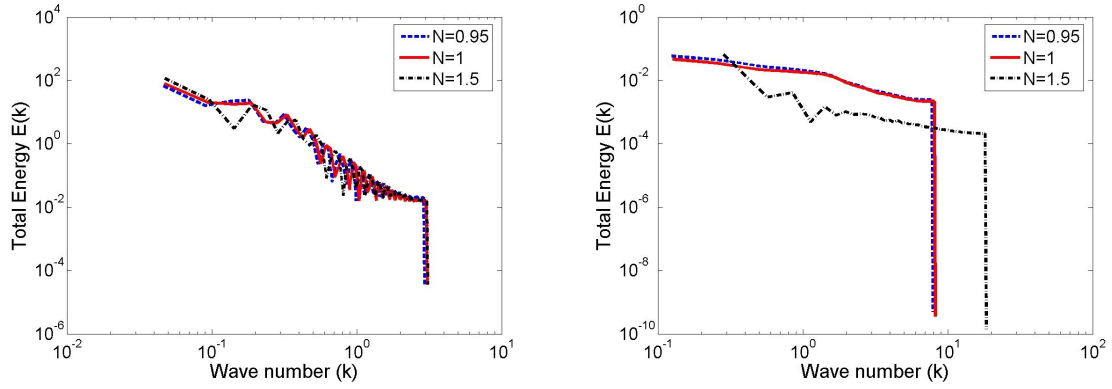
Figure 5.13. Influence of N number on energy spectra, 128^3 at t=1 (left) and t=5 (right).

CHAPTER 6

CONCLUSIONS AND RECOMMENDATIONS

6.1 Conclusions

The interaction of the detonation wave with CHIT was accomplished successfully. DNS was performed for turbulence interacting with three different heat release rate and activation energy combinations. A mesh independency study revealed that a minimum grid size of 128^3 is necessary to capture the detonation wave and turbulence satisfactorily to all possible scales. The study was repeated with varying a new non-dimensional number N which characterizes the detonation-to-turbulence length scales.

In summary, the detonation wave and turbulence interaction resulted in the following observations:

1. The detonation wave becomes corrugated.

2. The detonation–turbulence interaction increased the turbulent energy at higher wave numbers in the moderate to low scales whereas the shock–turbulence interaction resulted in increase in energy at small scales only. This extra amplification in energy is attributed to the effect of increase in streamwise velocity.

3. There is a rapid energy decay with wave number after the detonation wave passage, with the decay being more rapid with higher heat release.

4. The higher the heat release, the higher the amplification of the rms of velocities, turbulent Mach number and thermodynamic parameters.

5. The detonation–turbulence interaction resulted in a higher increase in turbulence length scale than that was observed in shock–turbulence interaction case. Also the increase in length scales is directly proportional to the heat release.

6. Rapid cascade of energy to small scales was observed in the post-detonation energy spectrum.

7. Vorticity fluctuations in the streamwise direction indicate marginal change whereas the ones corresponding to transverse directions show a drastic rise initially followed by a gradual decrease in the post-detonation turbulence data. It also revealed that the higher the heat release more rapid the change in vorticity fluctuations.

8. Reynolds stresses in the transverse directions reveal rapid rise in their value after detonation wave passage whereas the Reynolds stress about the streamwise direction was hardly affected by the detonation wave.

9. The higher the value of N, the higher the amplification in turbulence statistical parameters.

10. The variation in N did not affect the vorticity rms values and hardly affected the Reynolds stresses.

11. The amplification in rms of pressure and thermodynamic variables is proportional to N.

12. Post-detonation turbulence interaction revealed that an increase in N increases the rate of decay of the spectrum with wave number.

6.2 Recommendations

To avoid complications of multi-step chemical kinetics, a one-step chemical reaction is employed in the present research. It is envisaged that multi-step chemical kinetics models will aid to explore better physics behind the detonation and chem-

istry. The multi-step chemical kinetics will also help in capturing the physics behind the transition from deflagaration to detonation, provided the computational setup considers the wall-effects and unsteady flow. The high wavenumber resolution indicated some numerical dissipation due to WENO scheme. Suppression of numerical dissipation of the WENO scheme and usage of high Reynolds number will ensue in much better resolution of the very small scales.

APPENDIX A

TWO–DIMENSIONAL INCOMPRESSIBLE
TURBULENCE SIMULATION

In this appendix, the procedure followed to carry out the two-dimensional incompressible turbulence simulation and results are presented. Two-dimensional simulations are performed to understand the fundamental aspects of turbulence and its modeling. It must be recalled that the realization in the laboratory of a perfect two-dimensional flow is extremely difficult [147] whereas numerical simulation has been successfully accomplished by many researchers. The simulation was accomplished using the concepts and algorithms, see Orlandi [27].

A.1 Governing equations and procedure

The two-dimensional, incompressible Navier–Stokes equations in primitive variables are

$$\frac{\partial u_j}{\partial x_j} = 0 \tag{A.1a}$$

$$\frac{\partial u_i}{\partial t} + \frac{\partial u_i u_j}{\partial x_j} = -\frac{\partial p}{\partial x_i} + \frac{1}{Re} \frac{\partial^2 u_i}{\partial x_j^2} \tag{A.1b}$$

where $(i,\, j) = (1,\, 2)$, u_i are the velocity components, t is time and p is pressure. The variables are non-dimensionalized with respect to a reference length scale L and a velocity scale U; the Reynolds number is

$$Re = \frac{UL}{\nu} \tag{A.2}$$

It has been a common practice to solve the Navier–Stokes equations in one of the three forms, namely, the vorticity–velocity, the vorticity-streamfunction, and primitive variable formulations. For the present simulation of two-dimensional turbulence, the numerical code was formulated in vorticity-streamfunction by performing

the curl operator to Eq. (A.1). This operation eliminates the pressure term and yields a transport equation for the vorticity as

$$\omega = \frac{\partial u_2}{\partial x_1} - \frac{\partial u_1}{\partial x_2} \tag{A.3}$$

Next, the relationship between the stream function ψ and velocity components are given by the relationship,

$$u_1 = \frac{\partial \psi}{\partial x_2}, \ u_2 = -\frac{\partial \psi}{\partial x_1} \tag{A.4}$$

Finally, the stream function results in mass continuity being unconditionally satisfied (provided the stream function is continuous). The incompressible, two-dimensional momentum and mass conservation equations for a Newtonian fluid then can be combined into one equation as

$$\frac{\partial \omega}{\partial t} + J(\omega, \psi) = \frac{1}{Re} \nabla^2 \omega \tag{A.5}$$

Here, $J(.,.)$ is the Jacobian of the arguments. The kinematic relationship between vorticity and the stream function is given as

$$\nabla^2 \psi = -\omega \tag{A.6}$$

These equations are solved using the Arakawa scheme of fourth-order accuracy [148] while enforcing periodic boundary condition in both directions. The evolution of two-dimensional turbulence depends on initial conditions. The initial stream function with

the desired energy spectrum $E(k,0)$ is assigned by using the real and imaginary parts of the Fourier coefficients. The discrete Fourier transform is

$$\psi(x_1, x_2) = \sum_{k_1=0}^{N_1-1} \sum_{k_2=-N_2/2}^{N_2/2-1} \hat{\psi}(k_1, k_2) e^{ik_1 x_1} e^{ik_2 x_2} \tag{A.7}$$

The energy in the wave-number space is obtained using the relationship between velocity and stream function, as

$$E(k_1, k_2) = (k_1^2 + k_2^2)\, \hat{\psi}(k_1, k_2)\, \hat{\psi}^*(k_1, k_2) \tag{A.8}$$

At each wave number $k = \sqrt{k_1^2 + k_2^2}$, the energy $E(k)$ is given by the contribution of each $E(k_1, k_2)$. The real coefficient $\psi_R(k_1, k_2)$ and the imaginary coefficient $\psi_I(k_1, k_2)$ can be expressed as

$$\psi_R(k_1, k_2) = a(k_1, k_2) \cos[2\pi b(k_1, k_2)] \tag{A.9a}$$

$$\psi_I(k_1, k_2) = a(k_1, k_2) \sin[2\pi b(k_1, k_2)] \tag{A.9b}$$

where $a(k_1, k_2)$ and $b(k_1, k_2)$ are random numbers with amplitudes between 0 and 1. The inverse Fourier transform then gives the stream function in physical space $\psi(x_1, x_2)$; its Laplacian gives the vorticity.

The initial energy spectrum used for the simulation is

$$E(k, 0) = C_2 k^4 e^{(-k/k_0)^2} \tag{A.10}$$

where C_2 is a constant used to adjust the peak energy location. The expression (A.10) gives more energy at large scales and also ensures the scales are small enough to let a
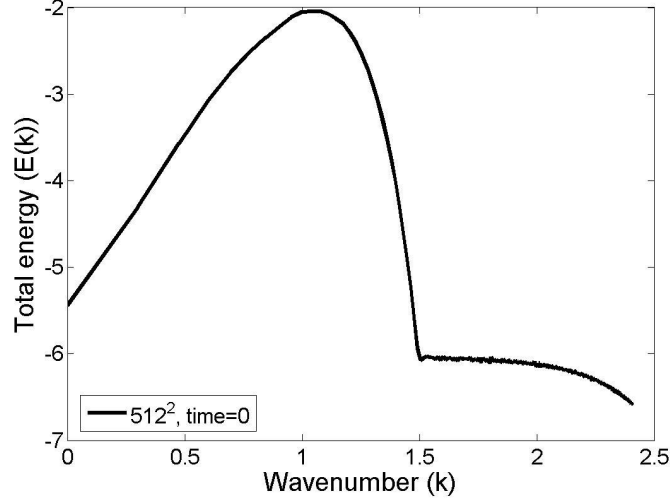
Figure A.1. The initial energy spectrum.

large number of merging to occur between $t = 0$ and $t = 50$, where t is time. Hence the spectrum results in a large number of vortex patches at the end of the simulation.

A.2 Results and conclusion

The computational domain was $2\pi \times 2\pi$. Three grid resolutions 128^2, 256^2, 512^2 were attempted which allowed the dependence of the evolution of the vorticity field on the resolution to be investigated. A sufficiently high Reynolds number ensures good accuracy. But, a lower Reynolds number is used in the present calculation. The simulations at $Re = 3000$ were able to produce a decaying energy spectra with a power law in a wide range of wave numbers.

The initial energy spectrum is shown in Fig. A.1   It is well-known that decaying turbulence depends on the initial conditions. The energy spectra in Fig. A.2 show that the maximum energy is at large scales and this is clear evidence of the greater number of mergings during the evolution. The evolution of two-dimensional
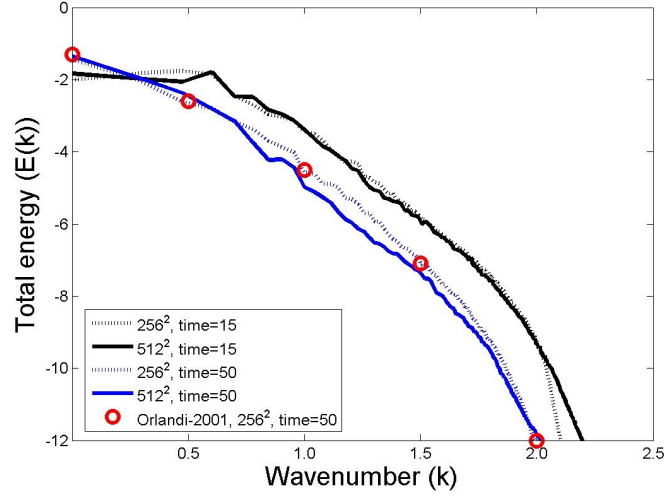
Figure A.2. Energy spectra at time=15 and 50 for 256^2 and 512^2.

turbulence depends on the initial conditions and the physical reason is related to the inverse energy cascade. The inverse energy cascade consists of the merging of vortices that depends on their sizes and space. The cascade towards small scales is usually called direct while that towards large scales is called inverse. The inverse energy cascade is the physical phenomenon that distinguishes the two-dimensional and three-dimensional turbulence. In three-dimensional turbulence, the energy goes from large to small scales, hence for isotropic turbulence, at high Reynolds number, there exists a universal behavior independent of the initial conditions.

Figure A.3 shows a similar observation of the enstrophy spectra. It can also be observed that higher grid sizes yield better resolution of vortices. Comparison of the trend of 256^2 and 512^2 results reveal that the 512^2 grid size shows more small scale data at time=50. Visualizations of the vorticity field permits a qualitative understanding of the turbulence kinematics. Figure A.4 shows the contour plot of vorticity field at $t = 0$.
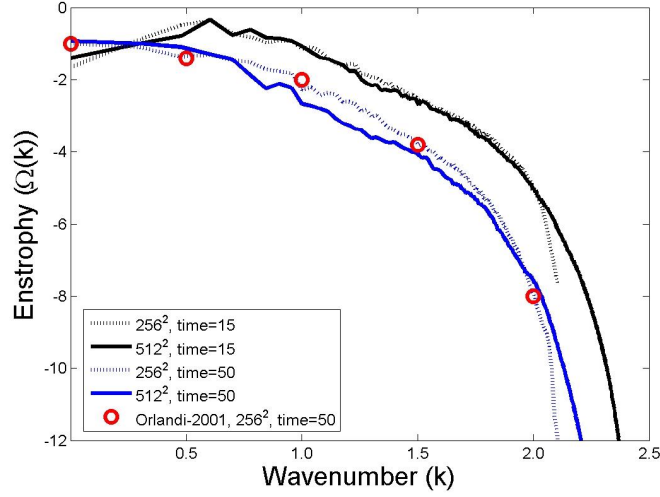
Figure A.3. Enstrophy spectra at $t = 15$ and 50 for 256^2 and 512^2.

In two-dimensional turbulence, the nonlinear interactions transfer energy primarily to the large scales [20]. Similar phenomena are observed in Figure A.5. As expected in decaying turbulence, interaction with other vortices results in fewer numbers of vortical structures as shown in Figure A.6. The simulation with several grid resolutions helped to investigate the dependence of vorticity evolution. The results of 128^2 (not shown here) shows a simulation which is not well resolved. The 256^2 and 512^2 were observed to show sufficiently resolved scales. They indicated the elongated vortical regions clearly which is due to enstrophy cascade.

In a nutshell, numerical simulations of temporally decaying two-dimensional turbulence show that merging of vortices results in maximum energy at large scales. The vorticity, energy and enstrophy spectra are in agreement with published results.
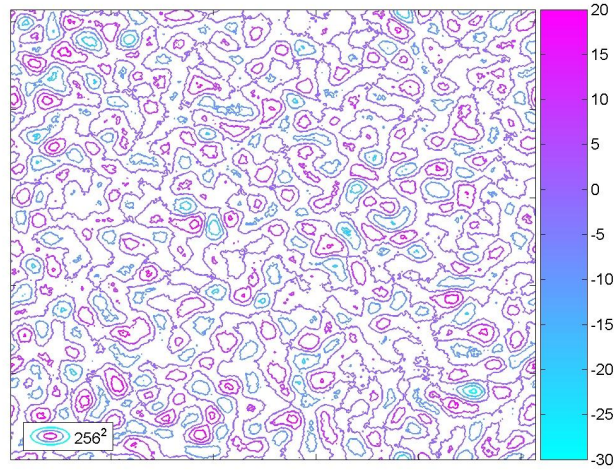
Figure A.4. Contours of Vorticity at $t = 0$.
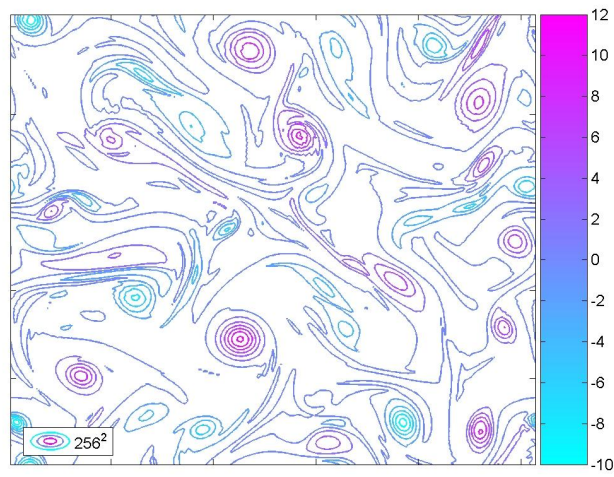
Figure A.5. Contours of Vorticity at $t = 15$.
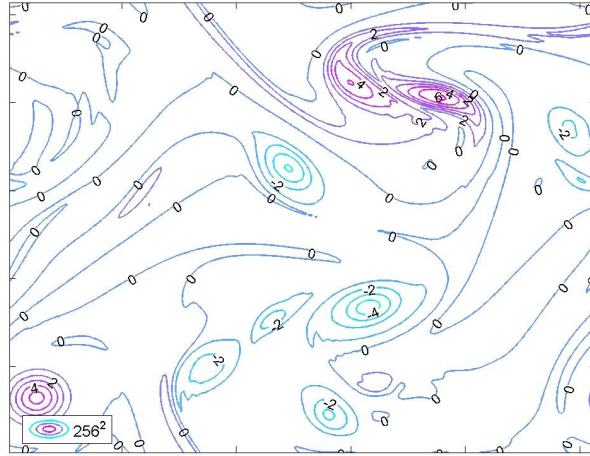
Figure A.6. Contours of Vorticity at $t = 50$.

APPENDIX B

THREE–DIMENSIONAL INCOMPRESSIBLE TURBULENCE SIMULATION

In this appendix, the procedure to carry out three-dimensional incompressible turbulence simulation and the simulation results are discussed. Direct numerical simulation is accomplished using the concepts and algorithms given by Orlandi [27].

B.1 Governing equations and procedure

Global conservation properties are analyzed to describe the time evolution of the turbulence spectrum. DNS is performed by solving the Navier–Stokes equation with three periodic directions. The important feature of three-dimensional turbulence is the vortex stretching which supports the energy cascade from large to small scales. The Navier–Stokes equations, for an incompressible flow, in conservative form are

$$\frac{\partial u_j}{\partial x_j} = 0 \tag{B.1a}$$

$$\frac{\partial u_i}{\partial t} + \frac{\partial u_i u_j}{\partial x_j} = -\frac{\partial p}{\partial x_i} + \frac{1}{Re}\frac{\partial^2 u_i}{\partial x_j^2} \tag{B.1b}$$

where u_i are the velocity components, t is time and p is pressure. The variables are non-dimensionalized with respect to a reference length scale L and a velocity scale U; the Reynolds number is

$$Re = \frac{UL}{\nu} \tag{B.2}$$

The initial perturbation field is generated in a cube of dimension $2\pi \times 2\pi \times 2\pi$. Finite difference discretization is employed along with the Arakawa 4th-order scheme for the nonlinear terms [148]. Arakawa suggests that the conservation of each of the quadratic invariants is sufficient to avoid computational instabilities; however, to get better accuracy, it is desirable to conserve both the quadratic invariants. The proof of conservation properties of the Jacobian expressions is discussed in [148]. Time integration is carried out using the third-order Runge–Kutta scheme. The solution scheme conserves kinetic energy and enforces zero divergence.

B.2 Initial conditions

The simulation of isotropic decaying turbulence is carried out as one of the initial steps of this research. The initial energy spectrum is the Mansour–Wray spectrum [26]:

$$E(k,0) = \frac{q^2}{2A} \frac{1}{k_p^{\sigma+1} k^\sigma} \exp\left[-\frac{\sigma}{2} \left(\frac{k}{k_p} \right)^2 \right] \tag{B.3}$$

where k_p is the wave number at which $E(k, 0)$ is maximum, σ is a parameter, and

$$A = \int k^\sigma \exp\left(-\frac{\sigma k^2}{2} \right) dk \tag{B.4}$$

The energy spectrum is related to the amplitude of the Fourier modes of the velocity components and also provides random and isotropic field. This particular energy spectrum is chosen because it has proved itself to represent the low and moderate Reynolds number turbulent flow with a good match to experimental data [26]. The velocity components are generated by three sets of random numbers that permit the uniform distribution of the angles $(\theta_1, \theta_2, \phi)$ on the interval $(0, 2\pi)$. The velocity components are

$$\tilde{u}_1 = \frac{\alpha |k| k_2 + \beta k_1 k_3}{|k| k_h} \tag{B.5a}$$

$$\tilde{u}_2 = \frac{-\alpha |k| k_2 + \beta k_3 k_2}{|k| k_h} \tag{B.5b}$$

$$\tilde{u}_3 = \frac{\beta k_h^2}{|k| k_h}. \tag{B.5c}$$

The tilde symbol indicates that these are complex quantities. The above expressions fulfill the requirement of a solenoidal velocity field in wave-number space $k_i u_i = 0$. Moreover, it can be shown that if

$$\alpha = \frac{E(k,0)}{4\pi k^2} \exp(l\theta_1) \cos(\phi) \tag{B.6a}$$

$$\beta = \frac{E(k,0)}{4\pi k^2} \exp(l\theta_2) \cos(\phi) \tag{B.6b}$$

the three-dimensional energy spectrum of this field is equal to $E(k, 0)$. These initial conditions are used in [7].

B.3 Results and conclusion

Temporal simulation of isotropic decaying turbulence is performed. Three different grids $(32^3, 64^3, 128^3)$ are used to check for adequate resolution of the turbulent flow. The procedure adopted and the formulae used to analyze these data are explained in Appendix C. The initial Reynolds numbers based on Taylor's length scale are 54.3, 64, and 107 respectively. Turbulence statistics such as velocity derivative, skewness, vorticity and dissipation rate show excellent agreement with both experimental and published numerical results. The initial energy spectrum is shown in Fig. B.1 where $(e(1), e(2), e(3))$ are the energy spectra in (x, y, z) respectively. The wave number in the abscissa is given by $k = \sqrt{k_1^2 + k_2^2 + k_3^2}$.

The evolution of the energy spectrum with the (nondimensional) time for $Re = 3000$ and $Re = 10^8$ are obtained. This appendix discusses the results of turbulence decay at low Reynolds number and its turbulence statistics in detail and a brief mention about the energy spectra trend for high Reynolds number case. Fig. B.2 shows the result for $Re = 3000$ and $k_p = 8$. This combination of k_p and Re is chosen to obtain the required initial Reynolds number based on Taylor scale. The energy
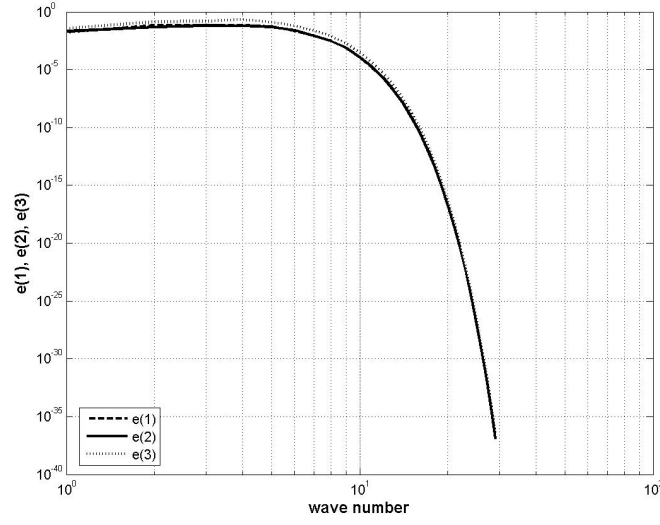
Figure B.1. The initial energy spectrum.

cascade is observed to show a decay of 12%. It is well-known that at high Re_λ, the inertial range follows the decay law $E(k) \simeq k^{-5/3}$. Keen observation of this graph will reveal that the inertial range shows the Kolmogorov decay.

The energy decay spectra with time variation is shown in Fig. B.3. The time evolution of the energy spectra in Kolmogorov scale units are shown in Fig. B.4. The energy spectra in Kolmogorov scale units are compared with the experimental data of Comte–Bellot & Corrsin and also with published numerical results [27, 26] and the present simulation using 128^3 resolution show good agreement, see Fig. B.5.

The skewness and flatness of the velocity derivatives in the (x, y, z) directions are shown in Fig. B.6. Subsequent to the initial large transient, the evolution results in a skewness in the range of -0.4 through -0.6 as expected [68, 33]. The evolution of the dissipation rate in the temporal decay for the 128^3 case is shown in Fig. B.7.

In three dimensions, vortex stretching generates vorticity components of the same order in each direction. This is the direct energy cascade, transferring energy by
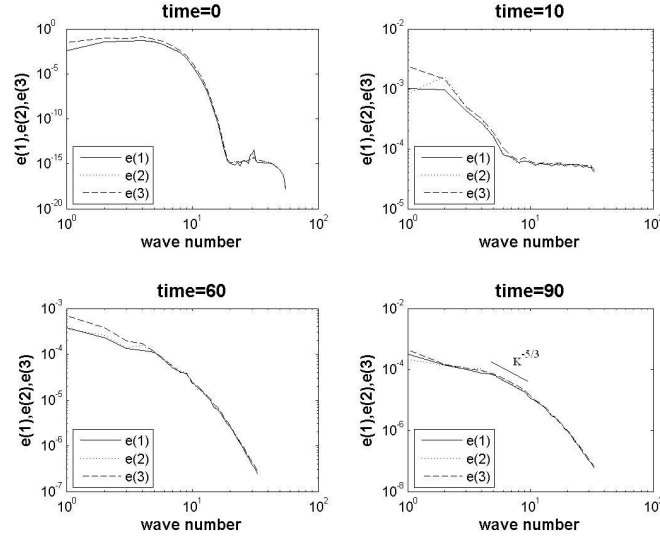
Figure B.2. The evolution of the energy spectrum for $Re = 3000$ and $k_p = 8$.

nonlinear interactions to small scales. The smallest scales are linked to the kinematic viscosity. The viscosity then dissipates the kinetic energy into heat due to friction. The evolution of the vorticity spectra about all three direction is shown in Fig. B.8. The figure shows the stretched vortices along with vortices of small scales. Lastly, simulation was carried out with very high Reynolds number to study the turbulence decay trend. For the case of $Re = 10^8$ and $k_p = 8$, Fig. B.9 shows that the low wave-number spectrum tends, preferably, to the k^2 law decay.

In summary, numerical simulations of temporally decaying isotropic turbulence show that the k^2 decay law occurs in the low wave-number range for $Re = 10^8$ whereas they capture the Kolmogorov slope of $k^{-5/3}$ in the inertial range for $Re = 3000$. The vorticity plot shows the stretching of vortices clearly. There is a good agreement of the velocity spectra, vorticity spectra, energy spectra, and other turbulence statistical parameters with published data.
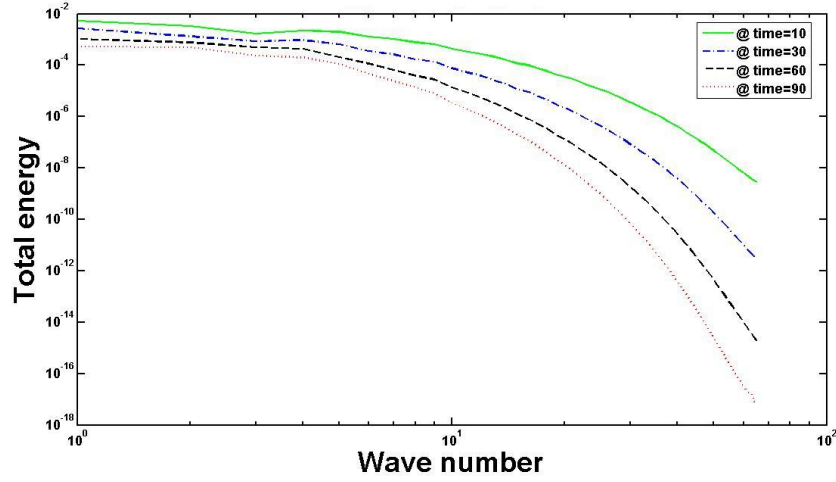
Figure B.3. The time evolution of the energy spectra in Kolmogorov scale units.
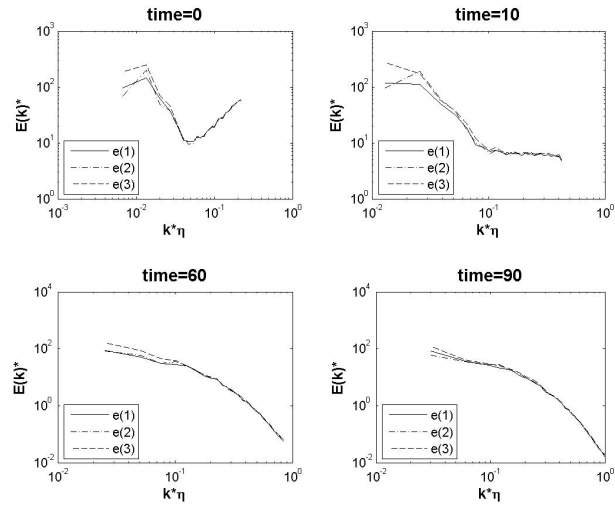
Figure B.4. The time evolution of the energy spectra in Kolmogorov scale units.
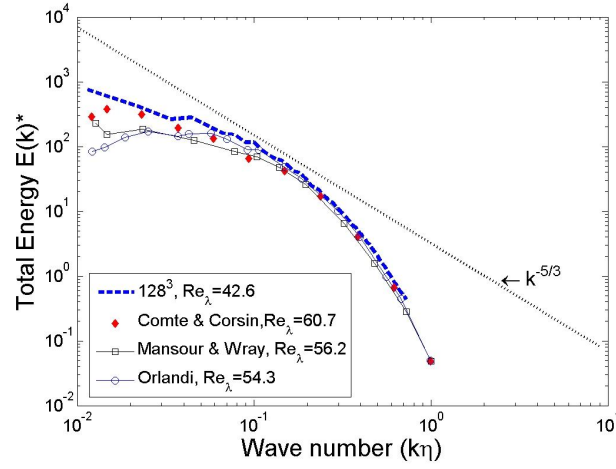
Figure B.5. The energy spectra in Kolmogorov scale units at Re_λ=42.6.
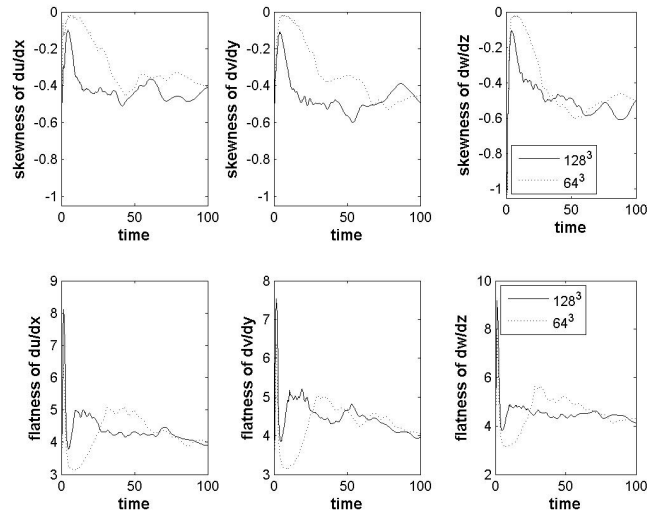
Figure B.6. The skewness values and flatness values of the velocity derivatives.
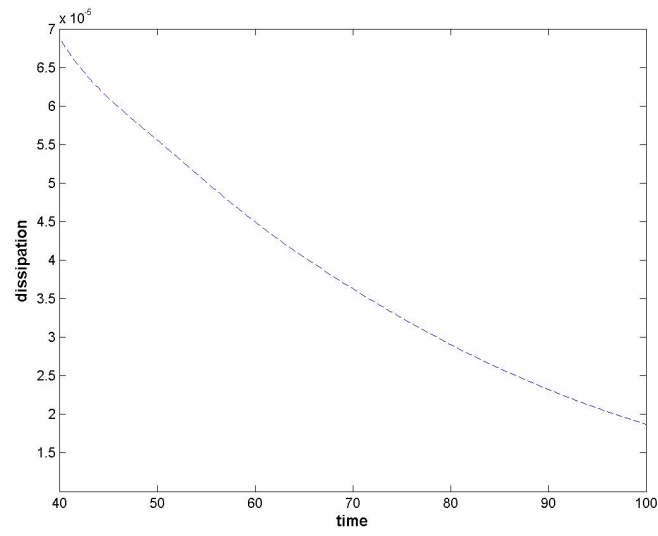
Figure B.7. The evolution of the dissipation rate.
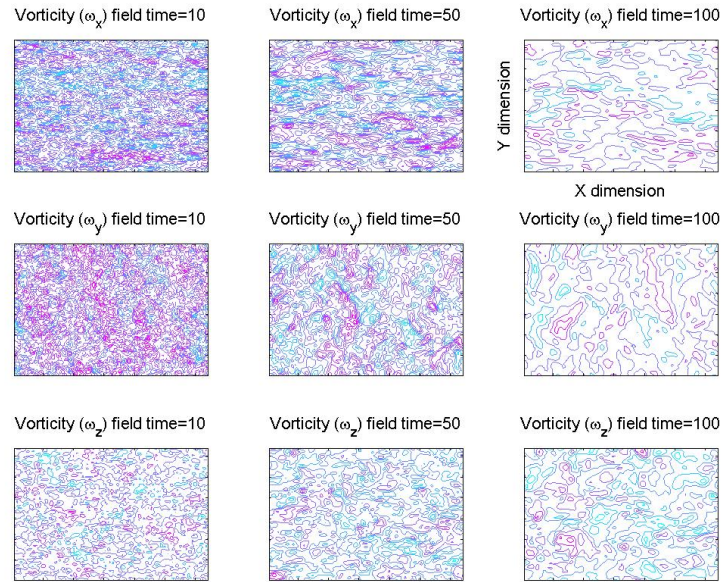
Figure B.8. The evolution of vorticity distribution.
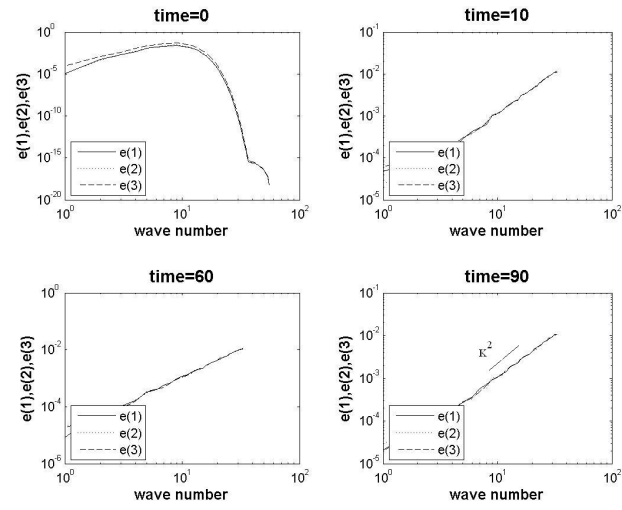
Figure B.9. The evolution of the energy spectra for $k_p = 8$ and $Re = 10^8$.

APPENDIX C

TURBULENCE STATISTICS OF THREE–DIMENSIONAL TURBULENCE AND THEIR ANALYSIS METHOD

In this appendix, the procedure to carry out analyses of both the three-dimensional incompressible turbulence simulation and compressible turbulence simulation are discussed.

C.1 Definition of turbulent quantities

The procedure to analyse the turbulent flow is discussed here. Averaging is performed in three directions. The justification of a sufficient number of samples necessary to get a meaningful statistical quantity is made by ensuring at least 2.09×10^6 samples are obtained using the simulation. This is reasonable for low-order statistics. Isotropic turbulence means it has nil mean velocity. The averaging procedure for a generic quantity is obtained using

$$< q >= \frac{1}{N_1 N_2 N_3} \sum_{l=0}^{N_1} \sum_{m=0}^{N_2} \sum_{n=0}^{N_3} q \qquad (C.1)$$

The turbulent stress $< u_i^{'2} >$ is obtained along with the skewness s_i and the flatness f_i

$$s_i = \frac{< u_i^{'3} >}{< u_i^{'2} >^{3/2}} \qquad (C.2)$$

$$f_i = \frac{< u_i^{'4} >}{< u_i^{'2} >^2} \qquad (C.3)$$

On the evaluation of these quantities, the velocity components $u_i^{'}$ are those at the location of the cell. On the other hand, in the evaluation of the stresses $< u_i^{'} u_j^{'} >$ with $i \neq j$ since each $u_i^{'}$ is defined at different locations, a linear interpolation permits the correlations at the center of the cell to be evaluated.

The skewness S_i and flatness F_i of the spatial derivatives $\partial u_i / \partial x_i$ are further important quantities in isotropic turbulence. Frisch [18] claims that the skewness

is the measure of vortex stretching and, in isotropic turbulence, it is related to the energy transfer term through the relationship

$$\left\langle \left(\frac{\partial u_i}{\partial x_i}\right)^3 \right\rangle = -\frac{2}{35} \int_0^\infty k^2 T(k) dk \tag{C.4}$$

Following Batchelor [20], since

$$\left\langle \left(\frac{\partial u_1}{\partial x_1}\right)^2 \right\rangle = \int_0^\infty k^2 E(k) dk \tag{C.5}$$

the skewness of the spatial derivative $\partial u_1/\partial x_1$ is

$$S_1 = -\left(\frac{135}{98}\right)^{1/2} \frac{\int_0^\infty k^2 T(k) dk}{(\int_0^\infty k^2 E(k) dk)^{3/2}} \tag{C.6}$$

The energy transfer at each wavenumber is a combination of the transfer by triadic interactions. From the energy transfer equation [19]

$$\frac{\partial E(k,t)}{\partial t} = T(k) - 2\nu k^2 E(k,t) \tag{C.7}$$

It turns out that $\int_0^\infty k^2 T(k) dk$ is the time rate of change of the enstrophy due to non-linear interactions. Since in three dimensions, the enstrophy is flowing from large to small scales, the numerator of Eq. (C.6) is positive; hence the skewness in isotropic turbulence is negative.

In the analysis of turbulent flows, the energy spectra give insights into turbulence structures. In order to do this, we use the Fourier transform to convert the data from physical to wave-number space. The Fourier transform in all three directions

permits the three-dimensional energy spectrum to be obtained. After a real FFT, two complex FFT transforms yields the energy spectrum $E_i(k)$.

$$E_i(k) = \sum_{k_1=0}^{N_1} \sum_{k_2=1}^{N_2/2} \sum_{k_3=0}^{N_3} u_i(k_1, k_2, k_3)\, u_i^*(k_1, k_2, k_3) \tag{C.8}$$

where the direction 2 is where the real FFT has been used. For the wave number $k_2 = 0$ the energy is

$$E_i(k) = \sum_{k_1=0}^{N_1} \sum_{k_3=0}^{N_3} 2u_i(k_1, 0, k_3)\, u_i^*(k_1, 0, k_3) \tag{C.9}$$

To check that the calculation of the spectrum is correct, it should be verified that

$$< u_i^2 >= \int_0^\infty E_i(k) dk \tag{C.10}$$

The spectrum is also calculated in Kolmogorov variables, where the wave number is multiplied by the Kolmogorov length scale η

$$\eta = \frac{\nu^3}{\epsilon} \tag{C.11}$$

and the spectra $E(k, t)$ by $(\nu^5 \epsilon)^{-1/4}$. The dissipation is evaluated in wave-number space as

$$\epsilon = 2\nu \int_0^\infty k^2 E(k, t) dk \tag{C.12}$$

or in physical space as

$$\epsilon = 4\nu < S_{ij} S_{ji} > \tag{C.13}$$

with

$$S_{ij} = \frac{1}{2} \left(\frac{\partial u_i}{\partial x_j} + \frac{\partial u_j}{\partial x_i} \right) \tag{C.14}$$

In homogeneous turbulence, $\epsilon = 2\nu\Omega$ with the enstrophy $\Omega = \frac{1}{2} < \omega_i\omega_i >$. The Reynolds number based on the Taylor length scale is obtained using

$$Re_\lambda = \sqrt{\frac{20}{3}} \frac{\int_0^\infty E(k,t)dk}{\nu(\int_0^\infty k^2 E(k,t)dk)^{\frac{1}{2}}} \tag{C.15}$$

Note that Re_λ is a fundamental quantity in isotropic turbulence which characterizes the energy spectrum. The enstrophy is found using the relation

$$\Omega^2 = \frac{1}{2}(\omega_x^2 + \omega_y^2 + \omega_z^2) \tag{C.16}$$

where

$$\omega_x = \frac{\partial w}{\partial y} - \frac{\partial v}{\partial z}, \quad \omega_y = \frac{\partial u}{\partial z} - \frac{\partial w}{\partial x}, \quad \omega_z = \frac{\partial v}{\partial x} - \frac{\partial u}{\partial y} \tag{C.17}$$

The Reynolds stress is computed using the following equation in compressible turbulence simulation.

$$\tau_{ij} = \overline{\rho u_i' u_j'} \tag{C.18}$$

REFERENCES

[1] S. Lee, S. K. Lele, and P. Moin, "Interaction of isotropic turbulence with shock waves: effect of shock strength." *Journal of Fluid Mechanics*, vol. 340, pp. 225–247, 1997.

[2] H. S. Ribner, "Spectra of noise and amplified turbulence emanating from shock-turbulence interaction," *AIAA*, vol. 25, pp. 436–442, 1987.

[3] L. Massa and F. K. Lu, "Turbulence detonation linear interaction analysis," *AIAA*, vol. 2009, p. 20, 2009.

[4] J. M. Powers, "Review of multiscale modeling of detonation," *Journal of Propulsion and Power*, vol. 22, pp. 1217–1229, 2006.

[5] H. S. Ribner, "Shock-turbulence interaction and the generation of noise," *NACA-1233*, 1955.

[6] H. S. Dou, H. M. Tsai, B. C. Khoo, and J. Qiu, "Simulations of detonation wave propagation in rectangular ducts using a three-dimensional WENO scheme," *Combustion and Flame*, vol. 154, pp. 644–659, 2008.

[7] R. S. Rogallo, "Numerical experiments in homogeneouos turbulence," *NASA TM-81315*, 1981.

[8] ——, "An ILLIAC program for the numerical simulation of homogeneous incompressible turbulence," *NASA TM 73203*, 1977.

[9] S. K. Lele, "Compressibility effects on turbulence," *Annual Review Fluid Mechanics*, vol. 26, pp. 211–254, 1994.

[10] L. Moriconi and R. Rosa, "Theoretical aspects of homogenous isotropic turbulence," *Journal of the Brazilian Society of Mechanics Science and Engineering*, vol. XXVI, pp. 391–399, 2004.

[11] Z. S. She and E. Jackson, "On the universal form of energy spectra in fully developed turbulence," *Physics of Fluids A*, vol. 5, pp. 1526–1528, 1993.

[12] P. Chassaing, "The modeling of variable density turbulent flows," *Flow, Turbulence and Combustion*, vol. 66, pp. 293–332, 2001.

[13] D. H. Porter and P. R. Woodward, "Inertial range structures in decaying compressible turbulent flows," *Physics of Fluids*, vol. 10, pp. 237–245, 1998.

[14] S. Cerutti, C. Meneveau, and O. M. Knio, "Spectral and hyper eddy viscosity in high-Reynolds number turbulence," *Journal of Fluid Mechanics*, vol. 421, pp. 307–338, 2000.

[15] A. W. Vreman, "Direct and large eddy simulation of the compressible turbulent mixing layer," Ph.D. dissertation, Universiteit de Twente, Netherland, 1995.

[16] M. Neda, "Numerical analysis and phenomenology of homogeneous isotropic turbulence generated by higher order models of turbulence," Ph.D. dissertation, University of Pittsburg, 2007.

[17] S. B. Pope, *Turbulent flows*. New York, USA: Cambridge University Press, 2000.

[18] U. Frisch, *Turbulence*. Cambridge, USA: Cambridge University Press, 1995.

[19] J. O. Hinze, *Turbulence*. New York, USA: Mc-Graw-Hill, 1975.

[20] G. K. Batchelor, *The theory of homogeneous turbulence*. Cambridge, USA: Cambridge University Press, 1953.

[21] F. Bataille and Y. Zhou, "Nature of the energy transfer process in compressible turbulence," *Physical Review E*, vol. 59, pp. 5417–5426, 1999.

[22] Y. Jang and S. M. de Bruyn Kops, "Psuedo spectral numerical simulation of miscible fluids with a high density ratio," *Computers and Fluids*, vol. 36, pp. 238–247, 2007.

[23] W. Jianping and T. Hasegawa, "Numerical simulation on compressible turbulence by spectral method," *Chinese Journal of Mechanics Press*, vol. 14, pp. 193–207, 1998.

[24] T. A. Zang, R. B. Dahlburg, and J. P. Dahlburg, "Direct and large eddy simulation of three dimensional compressible navier stokes turbulence," *Physics of Fluids A*, vol. 4, pp. 127–140, 2005.

[25] A. J. Lowe and P. A. Davidson, "The evolution of freely-decaying, isotropic, two-dimensional turbulence," *European Journal of Mechanics*, vol. 24, pp. 314–327, 2005.

[26] N. N. Mansour and A. A. Wray, "Decay of isotropic turbulence at low Reynolds number," *Physics of Fluids*, vol. 6, pp. 808–814, 1994.

[27] P. Orlandi, *Fluid Flow Phenomena.* Netherlands: Kluwer Academic Publishers, 2001.

[28] S. Lee, S. K. Lele, and P. Moin, "Simulation of spatially evolving turbulence and the applicability of Taylor's hypothesis in compressible flow," *Physics of Fluids A*, vol. 4, pp. 1521–1530, 1992.

[29] ——, "Eddy shocklets in decaying compressible turbulence," *Physics of Fluids A*, vol. 3, pp. 657–664, 1991.

[30] S. Pirozzoli and F. Grasso, "Direct numerical simulations of isotropic compressible turbulence influence of compressibility on dynamics and structures," *Physics of Fluids*, vol. 16, pp. 4386–4407, 2004.

[31] S. Sarkar, "The pressure dilatation correlation in compressible flows," *Physics of Fluids A*, vol. 4, pp. 2674–2682, 1992.

[32] B. K. Shivamoggi, "Multifractal aspects of the scaling laws in fully developed compressible turbulence," *Annals of Physics*, vol. 243, pp. 169–176, 1995.

[33] C. Meneveau and T. S. Lund, "On the Lagrangian nature of the turbulence energy cascade," *Physics of Fluids*, vol. 6, pp. 2820–2825, 1994.

[34] O. Zeman, "On the decay of compressible isotropic turbulence," *Physics of Fluids A*, vol. 3, pp. 951–955, 1991.

[35] H. Miura and S. Kida, "Acoustic energy exchange in compressible turbulence," *Physics of Fluids*, vol. 7, pp. 1732–1742, 1995.

[36] X. D. Cai, E. E. O'Brien, and F. Ladeinde, "Thermodynamic behaviour in decaying, compressible turbulence with initally dominant temperature fluctuations." *Physics of Fluids*, vol. 9, pp. 1754–1763, 1997.

[37] G. Erlebacher and S. Sarkar, "Statistical analysis of the rate of strain tensor in compressible homogeneous turbulence," *Physics of Fluids*, vol. 5, pp. 3240–3254, 1993.

[38] S. Goto, "A physical mechanism of the energy cascade in homogeneous isotropic turbulence," *Journal of Fluid Mechanics*, vol. 605, pp. 355–366, 2008.

[39] O. Roussel, K. Schneider, and M. Farge, "Coherent vortex extraction in 3D homogeneous turbulence comparison between orthogonal and biorthogonal wavelet decompositions," *Journal of Turbulence*, vol. 6, pp. 1–15, 2005.

[40] J. Ma and M. Y. Hussaini, "Three dimensional curvelets for coherent vortex analysis of turbulence," *Applied Physics Letters 184101*, vol. 91, 2007.

[41] H. Miura, "Analysis of vortex structures in compressible isotropic turbulence," *Computer Physics Communications*, vol. 147, pp. 552–555, 2002.

[42] P. K. Yeung and Y. Zhou, "Universality of the Kolmogorov constant in numerical simulations of turbulence," *Physical Review E*, vol. 56, pp. 1746–1752, 1997.

[43] J. Schumacher, "Sub-Kolmogorov scale fluctuations in fluid turbulence," *EPL*, vol. 80, p. 6, 2007.

[44] R. Samtaney, D. I. Pullin, and B. Kosovic, "Direct numerical simulation of decaying compressible turbulence and shocklet statistics," *Physics of Fluids*, vol. 13, pp. 1415–1430, 2001.

[45] S. M. de Bruyn Kops and J. J. Riley, "Direct numerical simulation of laboratory experiments in isotropic turbulence," *Physics of Fluids*, vol. 10, pp. 2125–2127, 1998.

[46] T. Ishihara, Y. Kaneda, M. Yokokawa, K. Itakura, and A. Uno, "Small-scale statistics in high-resolution direct numerical simulation of turbulence," *Journal of Fluid Mechanics*, vol. 592, pp. 335–366, 2007.

[47] M. Yokokawa, K. Itakura, A. Uno, T. Ishihara, and Y. Kaneda, "16.4-Tflops direct numerical simulation of turbulence by a Fourier spectral method on the Earth simulator," *Proceedings of the 2002 ACM/IEEE conference on Supercomputing*, pp. 1–17, 2002.

[48] F. Ladeinde, X. Cai, M. R. Visbal, and D. V. Gaitonde, "Turbulence spectra characteristics of high order schemes for direct and large eddy simulation," *Applied Numerical Mathematics*, vol. 36, pp. 447–474, 2001.

[49] M. Wu and M. P. Martin, "Assessment of numerical methods for DNS of shock-wave/turbulent boundary layer interactions," *AIAA-717*, pp. 1–16, 2006.

[50] E. M. Taylor and M. P. Martin, "Stencil adaptation properties of a WENO scheme in direct numerical simulations of compressible turbulence," *Journal of Scientific Computing*, vol. 30, pp. 533–554, 2007.

[51] E. M. Taylor, M. Wu, and M. P. Martin, "Optimisation of nonlinear error for Weighted Essentially Non-Oscillatory methods in direct numerical simulations

of compressible turbulence," *Journal of Computational Physics*, vol. 223, pp. 384–397, 2007.

[52] A. E. Honein and P. Moin, "Higher entropy conservation and numerical stability of compressible turbulence simulations," *Journal of Computational Physics*, vol. 201, pp. 531–545, 2004.

[53] R. S. Klessen and D. N. C. Lin, "Diffusion in supersonic turbulent compressible flows," *Physical Review E*, vol. 67, pp. 1–10, 2003.

[54] D. H. Porter, A. Pouquet, and P. R. Woodward, "Kolmogorov-like spectra in decaying three-dimensional supersonic flows," *Physics of Fluids*, vol. 6, pp. 2133–2142, 1994.

[55] ——, "Three-dimensional supersonic homogeneous turbulence," *Physical Review Letters*, vol. 68, pp. 3156–3159, 1992.

[56] S. Sukoriansky, A. Chekhlov, S. A. Orszag, B. Galperin, and I. Staroselsky, "Large eddy simulation of two dimensional isotropic turbulence," *Journal of Scientific Computing*, vol. 11, pp. 13–45, 1996.

[57] G. H. Cottet, D. Jiroveanu, and B. Michaux, "Vorticity dynamics and turbulence models for large eddy simulations," *Mathematical Modeling and Numerical Analysis*, vol. 37, pp. 187–207, 2003.

[58] A. W. Vreman, B. J. Geurts, J. G. M. Kuerten, and P. J. Zandbergen, "A finite volume approach to large eddy simulation of compressible homogeneous isotropic decaying turbulence," *International Journal for Numerical Methods in Fluids*, vol. 15, pp. 799–816, 1992.

[59] G. Lodato, P. Domingo, and L. Vervisch, "Three dimensional boundary conditions for direct and large eddy simulation of compressible viscous flows," *Journal of Computational Physics*, vol. 227, pp. 5105–5143, 2008.

[60] M. P. Martin, U. Piomelli, and G. V. Candler, "Subgrid scale models for compressible large eddy simulations," *Theoretical and Computational Fluid Dynamics*, vol. 13, pp. 361–376, 2000.

[61] B. Thornber, A. Mosedale, and D. Drikakis, "On the implicit large eddy simulations of homogeneous decaying turbulence," *Journal of Computational Physics*, vol. 226, pp. 1902–1929, 2007.

[62] W. J. Rider, "Effective subgrid modeling from the ILES simulation of compressible turbulence," *Journal of Fluids Engineering*, vol. 129, pp. 1493–1496, 2007.

[63] Y. Hou and K. Mahesh, "A robust, colocated, implicit algorithm for direct numerical simulation of compressible, turbulent flows," *Journal of Computational Physics*, vol. 205, pp. 205–221, 2005.

[64] A. Hansen, N. Sorensen, J. Johansen, and J. A. Michelsen, "Detached-eddy simulation of decaying homogeneous isotropic turbulence," *AIAA-885*, p. 15, 2005.

[65] G. A. Blaisdell, G. N. Coleman, and N. N. Mansour, "Rapid distortion theory for compressible homogeneous turbulence under isotropic mean strain," *Physics of Fluids*, vol. 8, pp. 2692–2705, 1996.

[66] A. Simone, G. N. Coleman, and C. Cambon, "The effect of compressibility on turbulent shear flow a rapid distortion theory and direct numerical simulation study," *Journal of Fluid Mechanics*, vol. 330, pp. 307–338, 1997.

[67] P. R. V. Slooten and S. B. Pope, "PDF modeling for inhomogeneous turbulence with exact representation of rapid distortions," *Physics of Fluids*, vol. 9, pp. 1085–1105, 1997.

[68] K. Mohseni, B. Kosovi, S. Shkoller, and E. J. Marsden, "Numerical simulations of the Lagrangian averaged Navier–Stokes equations for homogeneous isotropic turbulence," *Physics of Fluids*, vol. 15, pp. 524–544, 2003.

[69] H. Yu, S. S. Girimaji, and L.-S. Luo, "DNS and LES of decaying isotropic turbulence with and without frame rotation using Lattice Boltzmann method," *Journal of Computational Physics*, vol. 209, pp. 599–616, 2005.

[70] M. Farge, N. K. R. Kevlahan, V. Perrier, and K. schneider, "Turbulence analysis, modelling and computing using wavelets revised version," *Proceedings of IEEE*, vol. 84, pp. 1–77, 1996.

[71] F. Nicolleau and J. C. Vassilicos, "Wavelets for the study of intermittency and its topology," *The Royal Society*, vol. 357, pp. 2439–2457, 1999.

[72] A. G. Lamorgese, D. A. Caughey, and S. B. Pope, "Direct numerical simualtion of homogeneous turbulence with hyperviscosity," *Physics of Fluids*, vol. 17, p. 10, 2005.

[73] W. Schmidt, W. Hillebrandt, and J. C. Niemeyer, "Numerical dissipation and the bottleneck effect in simulations of compressible isotropic turbulence," *Computers and Fluids*, vol. 35, pp. 353–371, 2006.

[74] P. Martin and G. V. Candler, "Effect of chemical reactions on decaying isotropic turbulence," *American Institute of Physics*, vol. 10, pp. 1715–1724, 1998.

[75] F. A. Jaberi, D. Livescu, and C. K. Madnia, "Characteristics of chemically reacting compressible homogeneous turbulence," *Physics of Fluids*, vol. 12, pp. 1189–1209, 2000.

[76] J. Doom, Y. Hou, and K. Mahesh, "A numerical method for DNS/LES of turbulent reacting flows," *Journal of Computational Physics*, vol. 226, pp. 1136–1151, 2007.

[77] F. A. Jaberi and C. K. Madnia, "Effects of heat of reaction on homogeneous compressible turbulence," *Journal of Scientific Computing*, vol. 13, pp. 201–228, 1998.

[78] Y. Andreopoulos, J. H. Agui, and G. Briassulis, "Shock wave turbulence interactions," *Annual Review Fluid Mechanics*, vol. 32, pp. 309–345, 2000.

[79] J. C. Anyiwo and D. Bushnell, "Turbulence amplification in shock-wave boundary layer interaction," *AIAA*, vol. 20, pp. 893–899, 1982.

[80] T. A. Zang, M. Y. Hussaini, and D. M. Bushnell, "Numerical computations of turbulence amplification in shock-wave interactions," *AIAA*, vol. 22, pp. 13–21, 1984.

[81] L. Jacquin, C. Cambon, and E. Blin, "Turbulence amplification by a shockwave and rapid distortion theory," *Physics of Fluids A*, vol. 5, pp. 2539–2550, 1993.

[82] R. Hannappel and R. Friedrich, "Direct numerical simulation of a Mach 2 shock interacting with isotropic turbulence," *Applied Scientific Research*, vol. 54, pp. 205–221, 1995.

[83] S. Jamme, J. B. Cazalbou, F. Torres, and P. Chassaing, "Direct numerical simulation of the interaction between a shock wave and various types of isotropic turbulence," *Flow Turbulence and Combustion*, vol. 68, pp. 227–268, 2002.

[84] R. H. Cohen, W. P. Dannevik, A. Dimits, D. Eliason, A. A. Mirin, D. H. Porter, O. Schilling, and P. W. Woodward, "Three dimensional high resolution simulations of Richtmyer Meshkov mixing and shock turbulence interaction," *6th International Workshop on the Physics of Compressible Turbulent Mixing UCRL JC 125309*, p. 6, 1997.

[85] S. Lee, "Interaction of isotropic turbulence with a shockwave," Ph.D. dissertation, Stanford University, 1992.

[86] E. Garnier, P. Sagaut, and M. Deville, "Large eddy simulation of shock homogeneous turbulence interaction," *Computers and Fluids*, vol. 31, pp. 245–268, 2002.

[87] F. Ducros, V. Ferrand, F. Nicoud, C. Weber, D. Darracq, C. Gacherieu, and T. Poinsot, "Large eddy simulation of the shock turbulence interaction," *Journal of Computational Physics*, vol. 152, pp. 517–549, 1999.

[88] S. Pirozzoli, "Conservative hybrid compact WENO schemes for shock-turbulence interaction," *Journal of Computational Physics*, vol. 178, pp. 81–117, 2002.

[89] E. Garnier, M. Mossi, P. Sagaut, P. Comte, and M. Deville, "On the use of shock-capturing schemes for LES," *Journal of Computational Physics*, vol. 153, pp. 273–311, 1999.

[90] S. Xanthos, G. Briassulis, and Y. Andreopoulos, "Interaction of decaying free stream turbulence with a moving shock wave pressure field," *Journal of Propulsion and Power*, vol. 18, pp. 1289–1297, 2002.

[91] J. Keller and W. Merzkirch, "Interaction of a normal shock with a compressible turbulent flow," *Experiments in Fluids*, vol. 8, pp. 241–247, 1990.

[92] L. Hesselink, "An experimental investigation of propagation of weak shockwaves in a random medium," Ph.D. dissertation, California Institute of Technology, 1977.

[93] D. R. White, "Structure of gaseous detonation III density in the induction region of hydrogen detonation," *Physics of Fluids*, vol. 6, pp. 1011–1015, 1963.

[94] K. Kailasanath, "Review of propulsion applications of detonation waves," *AIAA*, vol. 38, pp. 1698–1708, 2000.

[95] M. Hanana, M. H. Lefebvre, and P. J. V. Tiggelen, "Preliminary experimental investigation of the pressure evolution in detonation cells," *Experimental Thermal and Fluid Science*, vol. 21, pp. 64–70, 2000.

[96] J. Hoke, R. Bradley, and F. Schauer, "Heat transfer and thermal management in a pulsed detonation engine," *AIAA 6486*, 2003.

[97] Z. J. X.Y. Hu, D.L. Zhang, "Analytical study of idealized two-dimensional cellular detonations," *Shock Waves*, vol. 11, pp. 475–480, 2002.

[98] J. Li, W. H. Lai, K. Chung, and F. K. Lu, "Experimental study on transmission of an overdriven detonation wave from propane oxygen to propane air," *Combustion and Flame*, vol. 1.91, pp. 1–15, 2008.

[99] P. K. Panicker, F. K. Lu, and D. R. Wilson, "Practical issues in ground testing of pulsed detonation engines," *IMECE paper 44068*, 2007.

[100] T. V. Bazhenova and V. V. Golub, "Use of gas detonation in a controlled frequency mode review," *Combustion, Explosion and Shock Waves*, vol. 39, pp. 365–381, 2003.

[101] X. Y. Hu, J. Czerwinska, N. Adams, and B. C. Khoo, "The cellular structure and its tracks of a H_2 O_2 ar detonation waves," *ICATM*, vol. 21, pp. 15–21, 2004.

[102] E. S. Oran and J. P. Boris, "Numerical approaches to combustion modeling," *AIAA Progress in Astronautics and Aeronautics*, vol. 135, 1991.

[103] ——, *Numerical Simulation of Reactive Flow*. New York, USA: Elsevier Science Publishing Company, 1991.

[104] V. N. Gamezo, A. M. Khokhlov, and E. S. Oran, "Deflagrations and detonations in thermonuclear supernovae," *Physics Review Letters*, vol. 92, pp. 1–4, 2004.

[105] V. N. Gamezo, D. Desbordes, and E. S. Oran, "Two-dimensional reactive flow dynamics in cellular detonation waves," *Shock Waves*, vol. 9, pp. 11–17, 1999.

[106] N. Tsuboi, Y. Daimon, and A. K. Hayashi, "Three-dimensional numerical simulation of detonations in coaxial tubes," *Shockwaves*, vol. 18, pp. 379–392, 2008.

[107] K. Eto, N. Tsuboi, and A. K. Hayashi, "Numerical study on three-dimensional C-J detonation waves detailed propagating mechanism and existence of OH radical," *Proceedings of the Combustion Institute*, vol. 30, pp. 1907–1913, 2005.

[108] C. Helzel, "Numerical approximation of conservation laws with stiff source term for the modeling of detonation waves," Ph.D. dissertation, der Otto-von-Guericke-Universitat Magdeburg, 2000.

[109] V. Deledicque, "Modeling and simulation of multidimensional compressible flows of gaseous and heterogeneous reactive mixtures," Ph.D. dissertation, Universite Catholique de Louvain, 2007.

[110] R. J. LeVeque, "Some traffic flow models illustrating interesting hyperbolic behaviour," *SIAM Annual Meeting and Minisymposium*, p. 11, 2001.

[111] V. Akkerman, V. Bychkov, A. Petchenko, and L.-E. Eriksson, "Accelerating flames in cylindrical tubes with nonslip at the walls," *Combustion and Flame*, vol. 145, pp. 206–219, 2006.

[112] H. He, "Numerical simulations of unsteady flows in a pulse detonation engine by the space time conservation element and solution element method," Ph.D. dissertation, The Ohio State University, 2006.

[113] K. Vaagsaether, V. Knudsen, and D. Bjerketvedt, "Simulation of flame acceleration and DDT in H2-air mixture with a flux limiter centered method," *International Journal of Hydrogen Energy*, vol. 32, pp. 2186–2191, 2007.

[114] T. H. Yi, D. R. Wilson, and F. K. Lu, "Numerical study of unsteady detonation wave propagation in a supersonic combustion chamber," *25th International Symposium on Shock Waves*, p. 6, 2004.

[115] T. H. Yi, D. A. Anderson, D. R. Wilson, and F. K. Lu, "Numerical study of two-dimensional viscous, chemically reacting flow," *AIAA-4868*, p. 11, 2005.

[116] S. Singh, J. M. Powers, and S. Paolucci, "Multidimensional detonation solutions from reactive navier-stokes equations," *17th International Colloquium on the Dynamics of Explosions and Reactive Systems*, p. 4, 1999.

[117] A. K. Kapila and D. W. Schwendeman, "A study of detonation diffraction in the ignition and growth model," p. 41, 2006.

[118] B. Wang, H. He, and S. T. J. Yu, "Direct calculation of wave implosion by the space time conservation element and solution element method," *AIAA 4354*, pp. 524–544, 2005.

[119] L. Tosatto and L. Vigevano, "Numerical solution of under-resolved detonations," *Journal of Computational Physics*, vol. 227, pp. 2317–2343, 2008.

[120] T. L. Jackson, M. Y. Hussaini, and H. S. Ribner, "Shock-turbulence interactions in a reacting flow," *NASA CR-189647*, p. 18, 1992.

[121] ——, "Interaction of turbulence with a detonation wave," *Physics of Fluids*, vol. 5, pp. 745–749, 1993.

[122] T. L. Jackson, A. K. Kapila, and M. Y. Hussaini, "Convection of a pattern of vorticity through a reacting shock wave," *Physics of Fluids A*, vol. 2, pp. 1260–1268, 1990.

[123] M. Y. Hussaini, F. collier, and D. M. Bushnell, "Turbulence alteration due to shock motion," *Turbulent Shear Layer/Shock Wave Interactions*, pp. 371–381, 1986.

[124] D. G. Lasseigne, T. L. Jackson, and M. Y. Hussaini, "Nonlinear interaction of detonation/vorticity wave," *Physics of Fluids A*, vol. 3, pp. 1972–1979, 1991.

[125] M. Short and D. S. Stewart, "The multi-dimensional stability of weak-heat-release detonations," *Journal of Fluid Mechanics*, vol. 382, pp. 109–135, 1999.

[126] R. J. LeVeque, *Finite volume methods for hyperbolic problems.* New York, USA: Cambridge University Press, 2002.

[127] C. W. Shu, "Essentially Non Oscillatory and Weighted Essentially Non Oscillatory schemes for hyperbolic conservation laws," *NASA-CR-206253*, 1997.

[128] X. dong Liu, S. Osher, and T. Chan, "Weighted Essentially Non-Oscillatory scheme," *Journal of Computational Physics*, vol. 115, pp. 200–212, 1994.

[129] A. K. Henrick, T. D. Aslam, and J. M. Powers, "Mapped Weighted Essentially Non-Oscillatory schemes achieving optimal order near critical points," *Physics of Fluids*, vol. 207, pp. 542–567, 2005.

[130] J. Shi, C. Hu, and C. W. Shu, "A technique of treating negative weights in WENO schemes," *Journal of Computational Physics*, vol. 175, pp. 108–127, 2002.

[131] D. Levy, G. Puppo, and G. Russo, "Central WENO schemes for hyperbolic systems of conservation laws," *Mathematical Modelling and Numerical Analysis*, vol. 33, pp. 547–571, 1999.

[132] D. S. Balsara and C. W. Shu, "Monotonicity preserving Weighted Essentially Non Oscillatory schemes with increasingly high order accuracy," *Journal of Computational Physics*, vol. 160, pp. 405–452, 2000.

[133] C. Hu and C. W. Shu, "Weighted Essentially Non Oscillatory schemes on triangular meshes," *Journal of Computational Physics*, vol. 150, pp. 97–127, 1999.

[134] S. Serna and A. Marquina, "Power ENO methods a fifth order accurate Weighted Power ENO method," *Journal of Computational Physics*, vol. 194, pp. 632–658, 2003.

[135] J. Qiu and C. W. Shu, "On the construction comparison and local characteristic decomposition for higher order central WENO schemes," *Journal of Computational Physics*, vol. 183, pp. 187–209, 2002.

[136] V. A. Titarev and E. F. Toro, "Finite volume WENO schemes for three-dimensional conservation laws," *Journal of Computational Physics*, vol. 201, pp. 238–260, 2004.

[137] P. Jenny and B. Muller, "Rankine–Hugoniot Riemann solver considering source terms and multidimenstional effects," *Journal of Computational Physics*, vol. 145, pp. 575–610, 1998.

[138] M. Abramowitz and I. A. Stegun, *Handbook of Mathematical Functions.* New York, USA: Dover, 1965.

[139] G. Jiang and C. Shu, "Efficient implementation of weighted ENO schemes," *Journal of Computational Physics*, vol. 126, pp. 202–228, 1996.

[140] R. LeVeque. Wenoclaw. [Online]. Available: www.amath.washington.edu/claw

[141] K. K. Kuo, *Principles of combustion.* New Jersey, USA: John Wiley and Sons, 2005.

[142] W. Fickett and W. C. Davis, *Detonation Theory and Experiment.* Mineola, NY-11501: Dover Publications, 1969.

[143] U. Austin. Tacc. [Online]. Available: http://www.tacc.utexas.edu/

[144] C.-B. G and C. S, "Simple Eulerian time correlations of full- and narrow-band velocity signals in grid generated isotropic turbulence," *Journal of Fluid Mechanics*, vol. 48, pp. 273–337, 1971.

[145] S. Lee, S. K. Lele, and P. Moin, "Direct numerical simulation of isotropic turbulence interacting with a weak shock wave," *Journal of Fluid Mechanics*, vol. 251, pp. 533–562, 1993.

[146] ——, "Direct numerical simulation and analysis of shock turbulence interaction," *AIAA 0523*, p. 11, 1991.

[147] Y. Couder and C. Basdevant, "Experimental and numerical studies of vortex couples in two-dimensional flows," *Journal of Fluid Mechanics*, vol. 16, pp. 405–424, 1986.

[148] A. Arakawa, "Computational design for long-term numerical integration of the equations of fluid motion," *Journal of Computational Physics*, vol. 1, pp. 119–143, 1966.

BIOGRAPHICAL STATEMENT

Hari Narayanan Nagarajan was born in Sathyamangalam, Erode DT, Tamil Nadu, India on 25th May 1980. He always looked up at the sky amazingly whenever he heard the sound of aeroplanes and helicopters in his native place. Some of the aircrafts were passenger planes/helicopters and the others were used to visit his native to seed the mountains and dense forests in the proximity every season. He was also perplexed whenever he watched eagles flying in the sky without flapping their wings. It is the quest to fly and desire of awareness of how they are flying that spurned the passion to become an aeronautical engineer eventually. He joined the Bachelor of Engineering in Aeronautics in 1997 at Park College of Engineering & Technology affiliated to Bharathiar University and fulfilled his wish of learning an advanced technology. He received his B.E. degree from Bharathiar University, Coimbatore, India, in 2001 and his M.S. degree from the University of Texas at Arlington in 2009 in Aerospace Engineering.

His exposure to industry began while participating in inplant training (unpaid internships) in manufacturing and maintenance units of both the mechanical and aeronautical industry during every semester holidays of undergraduate studies.

Hari started his professional career in September 2001 as a senior contract engineer in Select Software Pvt Ltd and worked to develop a generic software using Visual Basic 6.0 and C for gas turbine performance analysis until June 2002. Then, he joined the Gas Turbine Research Establishement, India in June 2002 as a research engineer (scientist) and worked until July 2007. His experience covered experimen-

tal and CFD analysis of gas turbine engine and its components which encompassed design, development and research activities.

His current research interest is in the area of CFD and aerospace technologies. He is a student member of AIAA, associate member of AeSI and a member of International Honour Society.

This paper documents the independent research that he has done in attaining the master's degree.